PORE-SCALE CONSIDERATIONS OF THE AIR-WATER INTERFACE OR ROUGH SURFACE ON FLOW IN POROUS MEDIA

by

Wenjuan Zheng

A dissertation submitted to the Faculty of the University of Delaware in partial fulfillment of the requirements for the degree of Doctor of Philosophy in Plant and Soil Sciences

Fall 2014

PORE-SCALE CONSIDERATIONS OF THE AIR-WATER INTERFACE OR ROUGH SURFACE ON FLOW IN POROUS MEDIA

by

Wenjuan Zheng

Approved: ______________________________

Blake C. Meyers, Ph.D.
Chair of the Department of Plant and Soil Sciences

Approved: ______________________________

Mark Rieger, Ph.D.
Dean of the College of Agriculture and Natural Resources

Approved: ______________________________

James G. Richards, Ph.D.
Vice Provost for Graduate and Professional Education

I certify that I have read this dissertation and that in my opinion it meets the academic and professional standard required by the University as a dissertation for the degree of Doctor of Philosophy.

Signed: ______________________________

Yan Jin, Ph.D.
Professor in charge of dissertation

I certify that I have read this dissertation and that in my opinion it meets the academic and professional standard required by the University as a dissertation for the degree of Doctor of Philosophy.

Signed: ______________________________

Lian-Ping Wang, Ph.D.
Member of dissertation committee

I certify that I have read this dissertation and that in my opinion it meets the academic and professional standard required by the University as a dissertation for the degree of Doctor of Philosophy.

Signed: ______________________________

Deb Jaisi, Ph.D.
Member of dissertation committee

I certify that I have read this dissertation and that in my opinion it meets the academic and professional standard required by the University as a dissertation for the degree of Doctor of Philosophy.

Signed: ______________________________

Liyun Wang, Ph.D
Member of dissertation committee

I certify that I have read this dissertation and that in my opinion it meets the academic and professional standard required by the University as a dissertation for the degree of Doctor of Philosophy.

Signed: ______________________________

Chandran R. Sabanayagam, Ph.D
Member of dissertation committee

ACKNOWLEDGEMENTS

First and foremost, I would like to express my sincere gratitude to my advisor Dr. Yan Jin for her support, patient, and encouragement throughout my graduate studies. It is a great opportunity to do my doctoral program under her systematic guidance. Her technical and editorial advice was essential to the completion of this dissertation.

I thank members of the dissertation committee, Dr. Lian-Ping Wang, Dr. Chandran Sabanayagam, Dr. Deb Jaisi, and Dr. Liyun Wang for their most valuable advices and insightful comments on this work. Especially I thank our research partner Dr. Lian-Ping Wang for fruitful discussion and his contribution to Chapter 2. I am grateful to Dr. Dani Or, our research collaborator from ETH Zürich, for productive discussion and assistance in nice graphics in Chapter 2. I thank Dr. Kirk Czymmek, Dr. Jeffrey Caplan and Dr. Chandran Sabanayagam of the Delaware Biotechnology Institutes Bioimaging Center for training and assisting with confocal scanning microscopy and atomic force microscopy imaging and analysis. I thank Dr. Eric Furst and his research group, Alexandra Bayles and Hyejin Han, for their assistance in fabricating the PDMS microchannels.

I also would like to thank my lab colleagues for their simulating discussion, assistant, feedback, and friendship. I would like express my special thanks to Dr. Volha Lazouskaya for being a great example in front of me. Special thanks also go to Dr. Gang Wang and Michael Doody for valuable comments on this thesis.

I wish to gratefully thank my parents for their unconditional support throughout my life. I wish to thank my husband, Xuan Yu and my daughter, Annabelle Yu, together with whom we now have the most lovely family. Finally, I would like to extend

my deepest gratitude and love to my grandmother for her intellectual life, strong will, and modest personality, for whom I dedicate this work.

TABLE OF CONTENTS

LIST OF TABLES

LIST OF FIGURES

ABSTRACT

Understanding flow in porous media is a challenging problem in many fields of fundamental science and engineering. This dissertation focuses on flow behavior at the pore scale, including observation and simulation of flow in microchannels and development of pore-space-based models for unsaturated hydraulic conductivity. Pore-scale flow is strongly influenced by relatively large interfacial areas (per unit volume) where surface tension, viscosity, and diffusion processes dominate gravity and inertia. Consequently, flow regimes may differ markedly from conventional large-scale flows.

In Chapter 2, I presented water flow patterns visualized in open capillary channels with various sizes using the $\mu-$PIV technique. I found that a partial-slip, rather than the commonly used stress-free condition, provided a more accurate description of the boundary condition at the air-water interface (AWI). The mechanism for a partial slip boundary condition at the AWI is due to the confinement of adjoining solid walls. In Chapter 3, I demonstrated that assuming a partial-slip AWI for corner flow could improve the prediction of unsaturated hydraulic conductivity at low water saturation conditions compared to that with a stress-free AWI. A roughness triangular pore space model (R-TPSM) for water retention and unsaturated hydraulic conductivity was developed in Chapter 4. The R-TPSM took into account surface roughness effects where film flow largely increased at low water content. The model was able to significantly improve the prediction of unsaturated hydraulic conductivity for heavier-textured soils (e.g., loam). In Chapter 5, the slip boundary condition at rough surfaces was resolved numerically at the pore scale. Roughness scale, together with interfacial shape and local slip length at the liquid-gas interfaces, and particularly the coupled effect of the last two, affected the effective slip length on the rough surfaces.

Improved physical understanding of surface/interface effects on multiphase flow behavior at both the pore scale and the core scale has been achieved in this study. Findings in this study are essential for an accurate quantification of a wide variety of multiphase problems in porous media as well as for design and manipulation of flow in microfluidics.

Chapter 1

GENERAL INTRODUCTION

Multiphase flow in porous media is encountered in a variety of fields of fundamental and applied sciences, e.g., soil physics, fluid mechanics, rheology, surface and colloid physical chemistry, hydrology, petroleum engineering, chemical engineering, material science, and biological engineering. As much of the subsurface environment (e.g., the soil) is porous, the flow of water and air in the vadose zone, and the flow of nonaqueous phase liquids in aquifers are important examples. Contaminants (e.g., pathogens, nanoparticles, pesticides, fertilizer, and heavy metals in dissolved or particulate phase) transporting along with water through percolation into groundwater pose potential risks to human health. Predicting the spread of such contaminants that infiltrate the ground requires understanding how liquids transport in subsurfaces. The economical concerns of multiphase flow systems include oil reservoir and natural gas reservoir. Additionally, microfluidics offers a large number of technologies involving multiphase flow, such as separation of biochemical sample, mixing, drug delivery, inkjet printers, dairy analysis, and so on.

1.1 Various Length Scales

A physical observation or theoretical treatment of flow in porous media usually fall into one of the three length scales: pore- (or microscopic), core- (or Darcy's or lab- or macroscopic) and field scales. Figure 1.1 illustrates a conceptual model of the relationship between different scales. Flow and transport at the field scale or watershed/regional scale is of more practical interest, for example, for refining agricultural management practices and for assessing the effects of agriculture on environmental quality. Because of the spacial heterogeneity of soil properties, continuum modeling

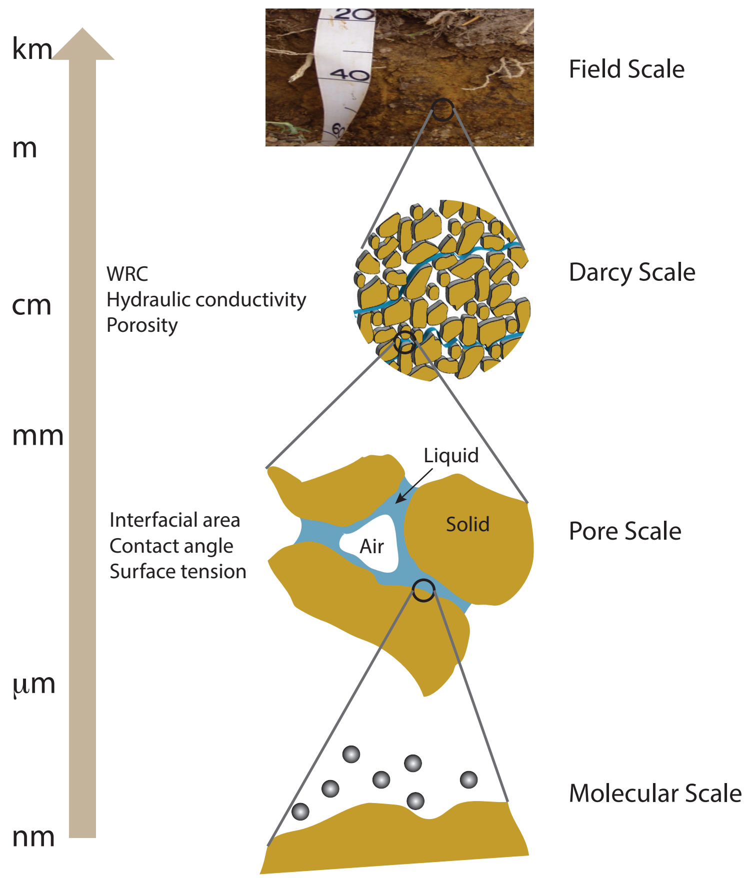

Figure 1.1: Illustration of the various spatial scales associated with flow in porous media

the processes at the field scale heavily depends on variables defined at the macroscopic (Darcy's) scale, which is also known as the representative element volume (REV). The REV is defined as the minimum volume of a porous media that allows the measurement of its property to be representative of the field under investigation. The pore scale studies deal with processes within a single pore or several pores, such that a porous medium is composed of a solid phase and pore space where flow and reaction occurred. This study will particularly focus on two scales: the pore scale and the Darcy's scale.

The typical length magnitude varies at each length scale. Soil pores can be as small as several nanometers (e.g., clay soils) [1], or macropores may exist with a size larger than 75 μm [2]. The size of a REV depends on the heterogeneity of the porous media, however, REV is much larger compared to the dimension at the pore scale. Experiments of flow and transport in laboratories conducted in columns with the length scale of centimeter, which usually fall in the REV scale [3]. Additionally, variables of interest at each scale are defined differently. For example, at the Darcy's scale, the porosity is used to describe the ratio of the void space to total volume. The porosity should not be affected by the addition or subtraction of several pores. If the total volume under consideration is small enough to fit entirely into a void space or solid particles, it is meaningless to define the porosity at the pore scale. The pore scale quantities such as contact angle or surface area which can be observed at the pore scale but are not variables for a macroscopic theory.

1.2 Flow at Darcy's Scale and the Pore Scale

The study of flow in porous media can be tracked back to 1856 when Darcy conducted the experiments of water flowing through beds of sand. Darcy's approach depicts that the flow rate is linearly proportional to the head loss, and the proportion, named as hydraulic conductivity (K), is used to characterize the permeability of the porous media. This approach has been used extensively to construct modeling frameworks for both single-phase and multiphase flow systems [4, 5, 6, 7]. While Darcy's law applies for single-phase flow system in homogeneous media very well, difficulties is generally encountered when it is extended to multiphase flow problems [8], where K is assumed to be functions of the saturation degree of each phase. The failure is due to the complex relationship between K and the saturations [9, 10, 11, 12, 13, 14], thus Darcy's approach for multiphase flow systems is impossible for accurate prediction of hydraulic conductivity.

An alternative to Darcy's approach is the pore-scale methods, where the derivation of mass, momentum, and energy conservation principles for flow in porous media is dealt exclusively with their phases, interfaces and contact lines [15, 16, 12]. The conservation laws provide insightfully physical meaning of transport process, therefore, pore-scale approaches inherently are able to simulate the flow behavior more accurately. Because pore-scale information cannot be informed from large-scale data, it is necessary to account properly for pore-scale processes not explicitly modeled at the continuum scale. A rigorous strategy to compare the pore-scale information with data collected at a large scale is to apply the microscopic conservation laws and to use techniques such as homogenization or representative element volume averaging [17, 18]. Because a point/area quantity such as contact angle or interfacial area that can be defined at the microscopic theory cannot be stated as macroscopic variables, the pore-scale observation is necessary to understand the fundamental fluid mechanics.

1.3 Interface/surface Effects on Flow at Pore-scale

As the length scale changes, the dominant processes and governing forces may vary from one scale to other scale. At the pore scale, as systems are reduced in size, surface area relative to volume increases often by several orders of magnitudes [19, 20]. The relatively large interfaces that are available for mass transfer have a profound impact on flow in the microscopic systems. One striking characteristic for such systems is that surface forces and viscous forces are dominant over the gravity and inertia so that flow behavior can markedly differ from that occurs at the macroscopic scale. For instance, capillarity, which describes the rise or depression of liquid in small channels, is the most common microscopic phenomenon. Capillary force also influences the shape of interfaces between different phases so that the interfaces remain curved rather than flat. In addition, recent publications [21, 22, 23, 24] indicate that the hydrodynamic boundary condition describing liquid-liquid interfaces at the pore scale may be different from the normally used shear-free boundary condition at the macroscale.

Another scale-dependent problem is to apply the no-slip boundary condition at solid surfaces for microscopic flow. The application of no-slip boundary condition to the Navier-Stokes equation has been well established in the field of fluid mechanics [25]. However, the validity of no-slip boundary was extensively debated for microscopic flow. The slippage at the solid surface can be affected by surface roughness [26, 27, 28, 29], surface wettability [30, 31, 32, 33], flow velocity [34, 35], as well as impurities and dissolved gas [36]. Therefore, no-slip boundary condition acts as no more than a convenient approximation that holds under macroscopic flow conditions [37, 38]. Roughness effects on the slip boundary condition have been reviewed [38, 39]. Because the surface/interfacial forces become more important in controlling the flow in porous media particularly at microscale, the knowledge of effects from rough solid surface is necessary for accurate flow prediction.

1.4 Modeling Hydrualic Conductivity

Continuum modeling of flow in subsurfaces based on the concept of representative elementary volume (REV) requires accurate description of water retention curve and hydraulic conductivity function. Significant attention has been given to the development of advanced hydraulic conductivity models because the experimental determination of unsaturated hydraulic conductivity (K_r) is considerably complicated. A common approach is to deduce the unsaturated hydraulic conductivity from water retention curve (i.e., pore-size distribution), supplemented by direct measurements of the saturated hydraulic conductivity (K_s) [40, 41, 42]. Because models developed based on this approach link the macroscopic Darcy's law to microscale flow behavior, these physically based models have shown improvements of predictions of hydraulic conductivity as compared with purely empirical models [43].

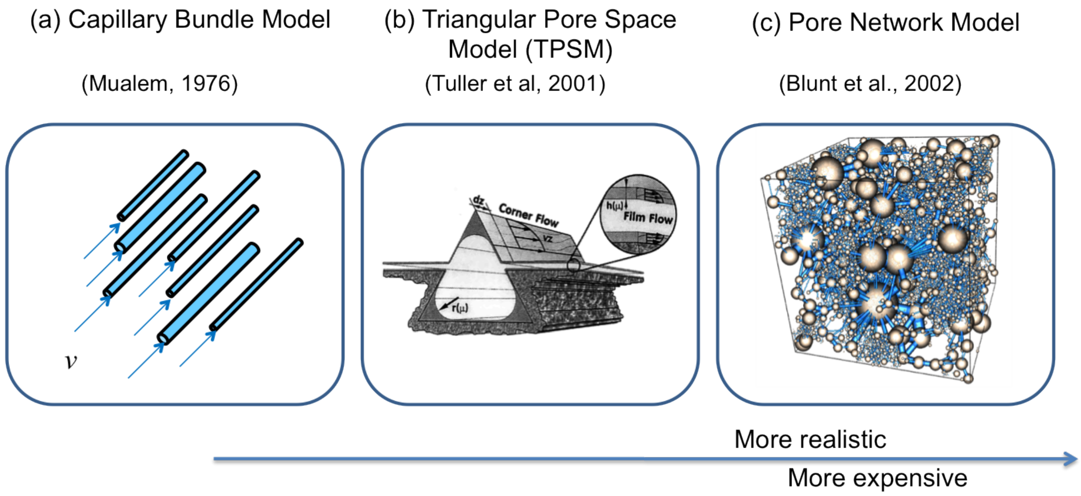

Figure 1.2: Different types of simplified pore space models. Soil pore space can be simplified by a bundle of cylindrical capillaries (a, the capillary bundle model) or a bundle of capillaries with triangular cross sections (b, the tiangular pore space model) or a bundle of cells that are compose of pore bodies connected to each other through pore throats (c, the pore network model).

Among the physically based models, the earliest ones conceptualized the porous medium (i.e., soil) as a bundle of cylindrical capillaries (BCC) [44, 4, 40, 42]. The BCC-based water retention and hydraulic conductivity models, e.g., van Genucthen-Mualem model (VGM), are most widely used, due to their simple mathematical formulas. However, the BCC-based models could not be rigorously verified against experimental data at low water contents [45]. The BCC-based model was improved by an alternative triangular pore space model (TPSM) [41], in which the pore space is represented by an angular central pore attached to slit-shaped spaces. The TPSM enables dual occupancy of air and water as water remains in corners after the center pore is drained, or accumulates in corners before central pore is completely filled during imbibition. Another advantage of the model is that the slit-shaped area is controlled by adsorptive force so that both adsorption and capillary processes are accentuated. Recently, there has been increasing research interest in using the pore network models for pore-scale flow modeling. In the pore network models, soils are represented by pore bodies connected to each other through pore throats. The pore network models provide an elegant approach to simulate multiphase flow problem, and they are potentially powerful and no longer limited to computing the conductance of the porous media [46, 47]. They are used as a platform to investigate a large number of pore-scale phenomena, including mass transfer between phases, wettability, and hysteresis. However, small representative sample volume (usually from 1 mm^3 to few mm^3) limits the applicability of these models to larger-scale problems [48].

The key elements in physically based hydraulic conductivity models are representation of pore geometries and accurate characterization of microscopic flow processes. Inaccurate and inadequate consideration of microscopic flow phenomena in such models could hinder the predictive capability considerably [49]. Review of hydraulic conductivity models disclose that the prevailing models (e.g., the VGM, the TPSM) generally do not adequately consider the microscopic flow behavior [43]. For instance, the air-water interface was treated as shear-free, and all solid surfaces of soil matrix were assumed to be smooth. Therefore, research gap exists in modeling of multiphase flow in porous media.

1.5 Framework of This Study

The goal of this work is to develop a better understanding of multiphase flow in porous media at the pore scale. In this study, I investigated the mechanisms of flow in porous media at the pore scale, as well as incorporated the pore-scale results into the macroscopic modeling framework. Two focuses are the role of curved air-water interfaces and the effect of surface roughness on pore-scale flow and ultimately on the macroscopic hydraulic conductivity. The specific objectives for this research include: 1) observation and investigation of the flow in open capillary channels; 2) characterization of the boundary conditions at air-water interfaces and at rough/patterned surfaces; 3) development of hydraulic conductivity models involving accurate descriptions of the boundary condition at air-water interfaces or considering surface roughness effects.

In the dissertation, Chapter 2 presents an experimental study that investigated the flow pattern and velocity distribution in open capillary channels with a rectangular cross section using μ-particle imaging velocimetry (PIV). The capillary channel represents a single pore of porous media. The boundary condition at the air-water interface was estimated from the measured velocity profiles in capillary channels with different sizes. Numerical calculation was also conducted to investigate the effect of boundary condition at AWI on pressure-driven flow patterns in microchannels.

Chapter 3 mainly demonstrates that prediction of unsaturated hydraulic conductivity can be improved by using a partial-slip boundary condition rather than a shear-free boundary condition at AWI in a triangular pore space model. The original triangular pore space model for hydraulic conductivity treats the boundary condition for corner flow as shear-free. The derivation of the expression for corner flow with a partial-slip boundary condition based on the experimental results from Chapter 2 and additional numerical simulations is provided.

Chapter 4 presents a new roughness-TPSM (R-TPSM) for water retention and unsaturated hydraulic conductivity considering the effects of surface roughness of soil matrix. The roughness features on solid surfaces that define the pore space largely increase water film length and thus the model can improve the prediction of unsaturated hydraulic conductivity at low water saturation condition.

Chapter 5 discusses the slip flow boundary condition at rough/patterned surfaces by numerical simulations, and its dependence on interfacial shape and interfacial shear, with an emphasis on the superhydrophobic surfaces.

The summary and conclusion from this research are presented in Chapter 6.

Chapter 2

THE ROLE OF MIXED BOUNDARIES ON VELOCITY PROFILES IN OPEN CAPILLARY CHANNELS FOR FLOW WITH CURVED LIQUID-GAS INTERFACES

2.1 Introduction

Multiphase flow in porous media is relevant to many natural and industrial processes encountered in soil physics, surface and colloidal sciences, environmental sciences, petroleum and chemical engineering. Such flow takes place in highly interconnected and tortuous regions bounded by solid-water and air-water interfaces [49]. Although these fluid interfaces are massless, they exert significant influence on dynamics of multiphase flow by shaping flow pathways and their ability to sustain stress. Simple Darcy-like flux extended from single-phase flow does not always sufficiently capture the physics of flow in processes such as water flow in partially saturated soil or oil extraction from a reservoir [8]. Alternatives based on mass, momentum, and energy conservation laws have been proposed to provide more accurate descriptions of multiphase flow by coupling conservation equations associated with phases and interfaces [17]. These descriptions require adequate understanding of pore-scale flow and the interfacial processes and conditions that control the flow.

Pore-scale flow is strongly influenced by the relatively large interfacial areas (per unit volume) where surface tension, viscosity and diffusion processes dominate gravity and inertia [19, 20]. In multiphase flow systems, the air-water interface is bounded ubiquitously by adjoining solid surfaces. This study focuses on the boundary condition for water at the air-water interface. It is argued that description of the boundary condition at the air-water interface is of relatively little consequence because of the strong constraint from no-slip walls [50]. However, other studies that considered flow on surfaces with similar mixed boundaries indicated that the air-water interface affected the overall mobility of water bounded by mixed interfaces [51, 52, 53]. Therefore, as a key component of the mixed boundaries, the boundary condition at the air-water interface requires an accurate characterization and description.

In general, a clean air-water interface at the macroscopic or continuum scales is often treated as a full-slip or stress-free boundary [50, 54, 55, 51]. While some experimental results seem to provide supportive evidence of this assumption [56, 57], others indicate different types of boundary conditions, such as partial-slip or even no-slip [56, 58, 22, 24, 21]. In addition to the inconsistencies in the types of boundary conditions at the air-water interface, there are also uncertainties as to the physical mechanisms responsible for preventing the air-water interface from being stress-free. The presence of minor impurities in the experimental systems was suspected as the cause of the observed partial-slip boundary condition in several studies [22, 23] . However, the partial-slip boundary was also observed in very clean systems [58, 21]. Manor et al. [22, 23] reported, on the basis of their atomic force microscopy study using a 50-μm-radius bubble in a clean system (i.e., in electrolyte without surfactant), that the air-water interface did not obey the stress-free boundary condition. Lazouskaya et al. [21] demonstrated that the air-water interface in an open rectangular capillary channel had limited mobility (i.e., not stress free) and could be described by a partial-slip boundary condition. Therefore, the physical origin of interfacial shear stress and the resulting partial-slip boundary condition in clean systems remains poorly understood.

Another factor that influences the microscopic behavior of multiphase flow is the shape of the air-water interface. When water is confined within small pores, the air-water interface is curved rather than flat because of the increasing capillary pressure at decreasing scales. The impact of meniscus shape on fluid flow has been discussed in the literature [59, 55, 60, 61, 62]. Ransohoff and Radke [59] reported that an increasing contact angle diminished the available area for flow, and thereby caused a greater resistance to the flow. Such a curved air-water interface can also induce supplementary energy dissipation as compared to that of a flat interface, resulting in a lower effective slip length[51, 52, 63].

The growing interest in microfluidic technology and advances in computational and observational methods now enable resolution of micrometric flow processes. Boundary conditions can be indirectly deduced by measuring forces between surfaces/interfaces using, for example, a surface force apparatus (SFA) [64] or atomic force microscopy (AFM) [22, 65] or determined directly using micro-particle image velocimetry (μ-PIV) [66, 21]. Since its introduction by Santiago et al. [67], the μ-PIV method has become a standard tool for measuring fluid velocity in microfluidic devices for near-wall flow, single-phase and multiphase flow, steady and turbulent flow, as well as pressure-driven, surface-tension-driven and electrokinetic flows.

This work extends our previous research on air-water interfacial behavior in capillary channels [21] by examining the physical origin of the observed limited mobility of the small-scale air-water interface. Particle tracking by means of confocal microscopy enabled experimental determination of air-water interfacial shapes and flow velocity profiles in open rectangular microchannels with a range of opening sizes (0.6 - 5.0 mm). The results were compared with theoretical analyses that examined the influence of the air-water interfacial shape and boundary conditions on the flow pattern in open square channels.

2.2 Theoretical Considerations

2.2.1 Meniscus shape between two vertical walls

We employed two approaches to calculate meniscus shape of an air-water interface confined between two vertical walls with spacing ranging from 0.1 to 5.0 mm. The first approach involved calculation of the exact meniscus shape under static conditions by balancing gravitational and capillary pressures (see Appendix A.2):

$$\rho g(h-h_0) = \frac{\sigma\frac{d^2h}{dx^2}}{[1+(\frac{dh}{dx})^2]^{\frac{3}{2}}} - \frac{2\sigma\cos\theta}{w} = \frac{\sigma}{R} - \frac{\sigma}{R_0} \tag{2.1}$$

where x is the distance measured horizontally from one wall of the channel (m),

h is the local height of water (m), ρ is the density of the bulk phase (kg m^{-3}), and σ is the surface tension (N m^-1), and R is the local radius of curvature (m). The reference radius of curvature is defined as $R_0 = w/(2\cos\theta)$, which is the radius of a circle passing through the two contact points on the vertical walls with the prescribed contact angle θ between the liquid and the vertical walls. w is the width of the channel (m). The reference height h_0 represents the average height (m) (measured from the bottom of the channel) of the meniscus or, equivalently the height of the air-water interface if the interface is flat. The boundary conditions on the vertical walls (i.e., $x = 0$) satisfy:

$$\left.\frac{dh}{dx}\right|_{x=0} = -\frac{1}{tan\theta} \tag{2.2}$$

Because we assume that the two vertical bounding walls are identical, the meniscus shape is symmetric about $x = w/2$, therefore,

$$\left.\frac{dh}{dx}\right|_{x=w/2} = 0 \tag{2.3}$$

And only half of the meniscus (from $x = 0$ to $x = w/2$) needs to be computed.

The second approach calculates the meniscus shape neglecting the gravity effect and assuming a constant mean curvature for the whole interface (i.e., a circular meniscus). The mean curvature depends on the contact angle between the liquid and the wall. The meniscus shape based on this approach is:

$$h = h_0 - \sqrt{(\frac{w}{2\cos\theta})^2 - (x - \frac{w}{2})^2} + \frac{w}{2\cos\theta}[\frac{\sin^{-1}(\cos\theta)}{2\cos\theta} + \frac{1}{2}\sin\theta] \tag{2.4}$$

In fact, equation 2.4 can be derived from equation 2.1 by simply setting the left hand side of equation 2.1 to zero (see Appendix A.2). Namely, equation 2.4 represents a limiting-case solution of equation 2.1 when w approaches zero and as such the capillary force completely dominates over the whole air-water interface.

In general equations 2.1 - 2.3 were solved numerically, and the solution was compared with that of equation 2.4. When the spacing between two vertical walls

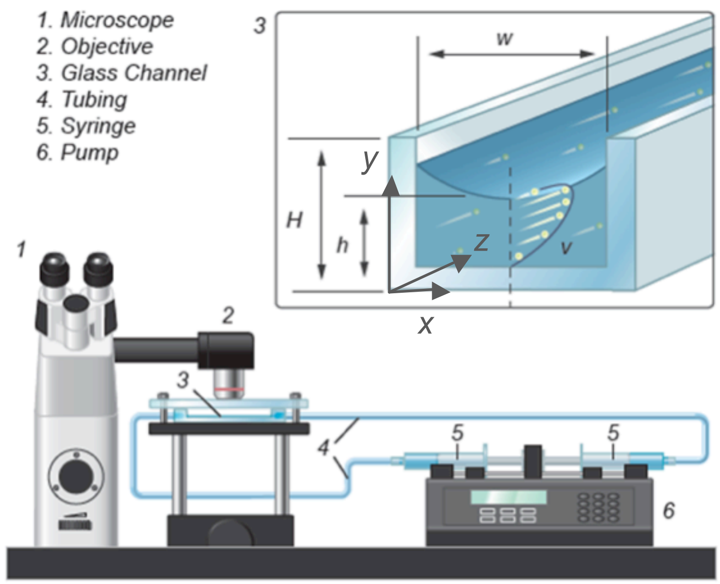

Figure 2.1: Schematic diagram of the experimental setup. The confocal laser scanning microscope μ-PIV system consists of an inverted microscope, a confocal scanning unit, a laser with an excitation wavelength of 488 nm, and a high-speed camera. Flow through microchannel with fluorecent colloidal particles are controlled by the syringe pump.The inlet and outlet of the microchannel are connected to a precision syringe pump using plastic tubing. A typical velocity profile along z-direction in the middle of the channel is shown in the channel.

increases, interfacial curvature at the center position decreases when other parameters are kept constant. This indicates increasing influence of body force such as gravity relative to the capillary force on the meniscus shape. Therefore, by comparing the exact meniscus shape calculated from equation 2.1 with the approximation assuming the meniscus to be a circular arc (equation 2.4), we can infer the importance of the capillary effect in the system.

2.2.2 Flow in open capillary channels

We considered the steady-state motion of an incompressible viscous fluid through a straight microchannel. For 1D flow in the z-direction (figure 2.1), the inertial term is identically zero. The flow is governed by the balance of pressure gradient and the viscous term, namely, the Stokes equation [68]:

$$\nabla^2 \mathbf{v} = \frac{1}{\mu}\frac{dp}{dz} \tag{2.5}$$

where $\mathbf{v}$ is velocity component in the z direction (m s^{-1}), μ is the viscosity (N s m^{-2}) of bulk phase, $\frac{dp}{dz}$ is the pressure drop along the channel (Pa m^{-1}).

The no-slip boundary condition is commonly applied at the solid-liquid interface as [68]:

$$\mathbf{v} = 0 \tag{2.6}$$

At the air-water interface, the boundary condition is described in the following form [61]:

$$\mu \nabla \mathbf{v} \cdot \hat{n} = \tau_0 \tag{2.7}$$

where $\hat{n}$ is the unit outward normal to the interface and τ_0 is the interfacial shear stress (N m^{-2}) that acts in the direction opposite to the direction of the bulk liquid flow. Mathematically, $\tau_0 = 0$ represents a shear-free surface and $\tau_0 < 0$ corresponds to a partial-slip boundary.

The Stokes equation (equation 2.5) was applied to model measured flow velocity profiles in the experimental microchannels, where the air-water interfaces were not pinned at the edges, did not reached the channel bottoms (figure 2.1). The cross-sectional liquid-filled area was assumed to be rectangular by neglecting the flow in the contact line region. As a result, the partial differential equation over a rectangular domain can be solved analytically by the separation of variables. The following dimensionless variables were introduced: $u = -v\mu/w^2(dp/dz)$, $X = x/w$, and $Y = y/h$. Under this scaling, the governing equation (equation 2.5) and boundary conditions (equations 2.6 and 2.7) have the form:

$$\frac{\partial^2 u}{\partial X^2} + s^2 \frac{\partial^2 u}{\partial Y^2} = -1 \tag{2.8}$$

$$u|_{X=0} = 0; \tag{2.9}$$

$$u|_{X=1} = 0; \tag{2.10}$$

$$u|_{Y=0} = 0; \tag{2.11}$$

$$\mu \frac{du}{dY}|_{Y=1} = \tau \tag{2.12}$$

where $s = w/h$ is the aspect ratio, and $\tau = (\tau_0 h)/(w^2(-dp/dz))$ is the dimensionless form of the interfacial shear stress.

The analytical solution of the above partial differential equation is

$$\begin{aligned} u(x,y) = &-\frac{x^2}{2} + \frac{x}{2} + \sum_{i=1}^{n} \sin(\pi n x)\{\frac{2((-1)^n - 1)}{(\pi n)^3}\cosh(\frac{\pi n}{s}y) \\ &+ \frac{-\frac{2((-1)^n-1)}{(\pi n)^3}[\sinh(\frac{\pi n}{s}) + \tau s(n\pi)]}{\cosh(\frac{\pi n}{s})}\sinh(\frac{\pi n}{s}y)\} \end{aligned} \tag{2.13}$$

By fitting equation 2.13 to experimentally measured velocity profiles at the channel center, $x = w/2$, two parameters that characterize the interfacial and flow properties (i.e., the interfacial shear stress and pressure gradient) were obtained. The computation was performed using a least-squares fitting procedure.

We also examined the effects of different types of boundary conditions at the air-water interface on the cross-sectional flow pattern. When unidirectional flow through an open-square microchannel was considered, the velocity distribution was calculated by solving equations 2.5 - 2.7 by assuming a flat air-water interface. The governing equation was set as $\nabla \mathbf{u} = 1$, and the boundary conditions at the open surface were $u = 0$, $\tau = 0.2$, and $\tau = 0$ representing no-slip, partial-slip, and stress-free conditions, respectively. In addition, we considered flow pattern with a curved airwater interface subjected to the above boundary conditions. The curvature κ, the reciprocal of the interfacial arc radius, was arbitrarily set to 1.6. The unit square domain in transformed variables X and Y was chosen because the Stokes equation solved over a rectangular area can be reduced to a dimensionless form over a unit square domain. The partial differential equation (equation 2.8), together with the boundary conditions (equations 2.9 - 2.12), was solved numerically using the pdetool toolbox in Matlab.

2.3 Experimental Materials and Methods

2.3.1 Experimental setup

A schematic representation of the experimental setup is given in figure 2.1. The confocal laser scanning microscope μ-PIV system (Zeiss 5 LIVE DUO, Carl Zeiss, Oberkochen, Germany) consisted of an inverted microscope, a confocal scanning unit, a laser with an excitation wavelength of 488 nm, and a high-speed camera. This system has the capability of acquiring a series of in-focus images by means of depth-wise optical slicing, allowing 3D image reconstruction [69]. Two air immersion objective lenses with magnification of 10x and 5x and corresponding numerical aperture of 0.3 and 0.25, respectively, were used. More detailed description and working principle of the μ-PIV system can be found in other reference [70].

2.3.2 Rectangular glass microchannels

The open microchannels were made from rectangular glass tubings (Friedrich & Dimmock Inc., Millville, NJ), which were cut length-wise and embedded into waxy base. Five microchannels with different inside sizes with the dimensions (w (mm) $\times$ H (mm)) of 0.6×0.4, 1.0×0.7, 2.0×1.6, 3.0×2.6, and 5.0×4.4 were used. The opening length of the microchannels was 40 mm in the axial direction for all the channels except the 5.0 mm one, which was 100-mm long. The lengths were selected to allow flow to fully develop in the channels. The inlet and outlet of the microchannel were connected directly to a precision syringe pump (PHD, Harvard Apparatus, Holliston, MA) using plastic tubing. The microchannels were reused for repeated experiments after a thorough cleaning, following the procedure described by Lazouskaya et al. [21].

2.3.3 Working fluid and tracers

The working fluid was deionized water seeded with 1.0-μm-diameter fluorescent particles (Molecular Probes Inc., Eugene, OR) as flow tracers. The particles were carboxylate-modified, hydrophilic, yellow-green, surfactant-free latex microspheres with a mass density of 1.055 g cm^{-3}, which is close to the density of water such that gravitational force is balanced by the buoyant force. We used a dilute particle suspension of 1 ppm concentration (i.e., 1.4×10^6 particles ml^{-1}) in all experiments. To ensure a monodispersed state, both concentrated and diluted colloidal suspensions were sonicated in an ultrasonic bath (Ultramet, Buehler, Lake Bluff, IL) for 1 min before use.

To examine whether the addition of tracers would change solution surface tension, we measured the surface tension of suspensions (0.16 mM $NaHCO_3$) at different colloid concentrations of 0, 2, 4, 6, 8, 10 ppm using the do Noüy ring method with a KSV sigma 700 tensiometer (KSV Instruments Ltd., Helsinki, Finland). All measurements were performed at room temperature (20°C). The measurements gave an average surface tension of 7.19×10^{-2} N m^{-1} with a small standard deviation of 9.33 $\times10^{-5}$ N m^{-1}, which indicates that the addition of colloids did not alter the solution surface tension.

2.3.4 μ-PIV experimental protocol

We conducted a series of flow experiments at a mean velocity of $\sim$0.50 mm s^{-1}. Optically sectioned images were captured along the y-axis (figure 2.1) at a step size of 50 μm or 100 μm at a resolution of 512×512 pixels and 12-bit gray scale and a scanrate of 20 frames s^{-1}. The objective lens focused on the middle between the inlet and outlet of the channels. Particle tracking software Volocity 5 (PerkinElmer Inc., Waltham, MA) was used to analyze the images to calculate the particle velocities and construct the velocity profiles. The location of the channel center $x = w/2$ (figure 2.1) was estimated by applying a quadratic equation to the measured velocity profiles along x axis at each layer to overcome the difficulties in directly determining the positions of microchannel walls from the images. Location $x = w/2$ acquired using this method was extended to the top layer (liquid-gas interface: $y = h$). Velocity on the bottom layer (liquid-solid interface: $y = 0$) was assumed to be 0 (i.e., no-slip).

To ensure steady-state flow, images were captured approximately 30 min after the initiation of each experiment when the configuration and position of the liquid-gas interface remained unchanged over the observation time spans. Evaporation, which has been identified as a source of potential error (e.g., inducing Marangoni effect, changing mass balance, etc.) [71], was minimized by placing the microchannel inside of a closed chamber packed with moist sponges during each experiment.

2.3.5 Visualization of air-water interfacial shape

We also conducted experiments to characterize the static liquid-gas meniscus shape using the same experimental setup shown in figure 2.1. Rhodamine B isothiocyanate (Sigma-Aldrich, St. Louis, MO) was added to the working fluid to improve imaging quality of the interface. Three-dimensional configurations of liquid-gas interfaces were built from stacks of 2D images with a section depth of 8.17 μm for 0.6 mm and 2.0 mm channels and 40.3 μm for 5.0 mm channel, respectively.

2.4 Results

We present results from a large number of captured confocal images that were analyzed for particle velocities to provide quantitative flow-field descriptions in the microchannels. Figure 2.2 is a representative transverse 2D velocity map, constructed for the 0.6 mm channel with a mean velocity of 0.514 mm s^{-1}, showing that the air-water interface was mobile and the maximum velocity was located in the middle of the channel. This finding indicates that the air-water interface was not stress free. It should be noted that although the liquid was flowing with a curved interface (figure 2.3), the velocity distribution was measured for a rectangular area by neglecting the contact line

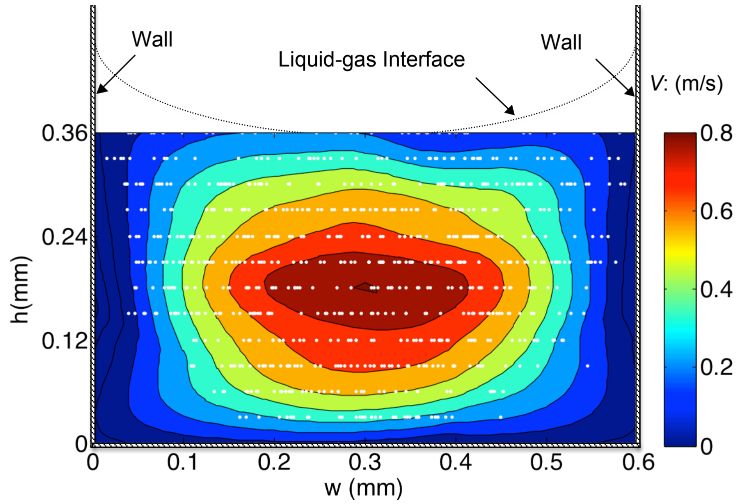

Figure 2.2: Representative 2D velocity distribution profile measured in the 0.6 mm channel at the mean velocity of 0.514 mm s^{-1}.

regions where we observed flow reversal. (Movie 1 is given in supplementary material showing colloid tracers in contact line region moving in the direction opposite to the bulk flow)

The flow pattern and interface characteristics were further examined through 1D velocity profiles (figure 2.4) constructed on the basis of velocities measured at the center of each of the five microchannels, ranging in size from 0.6 mm to 5.0 mm. These profiles all have similar shapes and, to some extent, resemble Poiseuille flow, a typical flow pattern found in fully developed incompressible flow in a closed capillary conduit. However, unlike Poiseuille flow, the profiles are not completely symmetrical from the solid-water interface (at the channel bottom) to the air-water interface, because the velocities did not vanish at the air-water interface. For a given mean flow rate, although velocities at the air-water interface in different channels were not significantly different, the maximum velocity in the profile decreased with increasing channel size from 0.88 mm s^{-1} (0.6 mm channel) to 0.65 mm s^{-1} (5.0 mm channel). In addition, the position of the maximum velocity shifted closer to the interface with increasing channel size.

We calculated velocity profiles for the same channel dimensions by solving the Stokes equation (equation 2.5) assuming a partial-slip boundary condition (equation

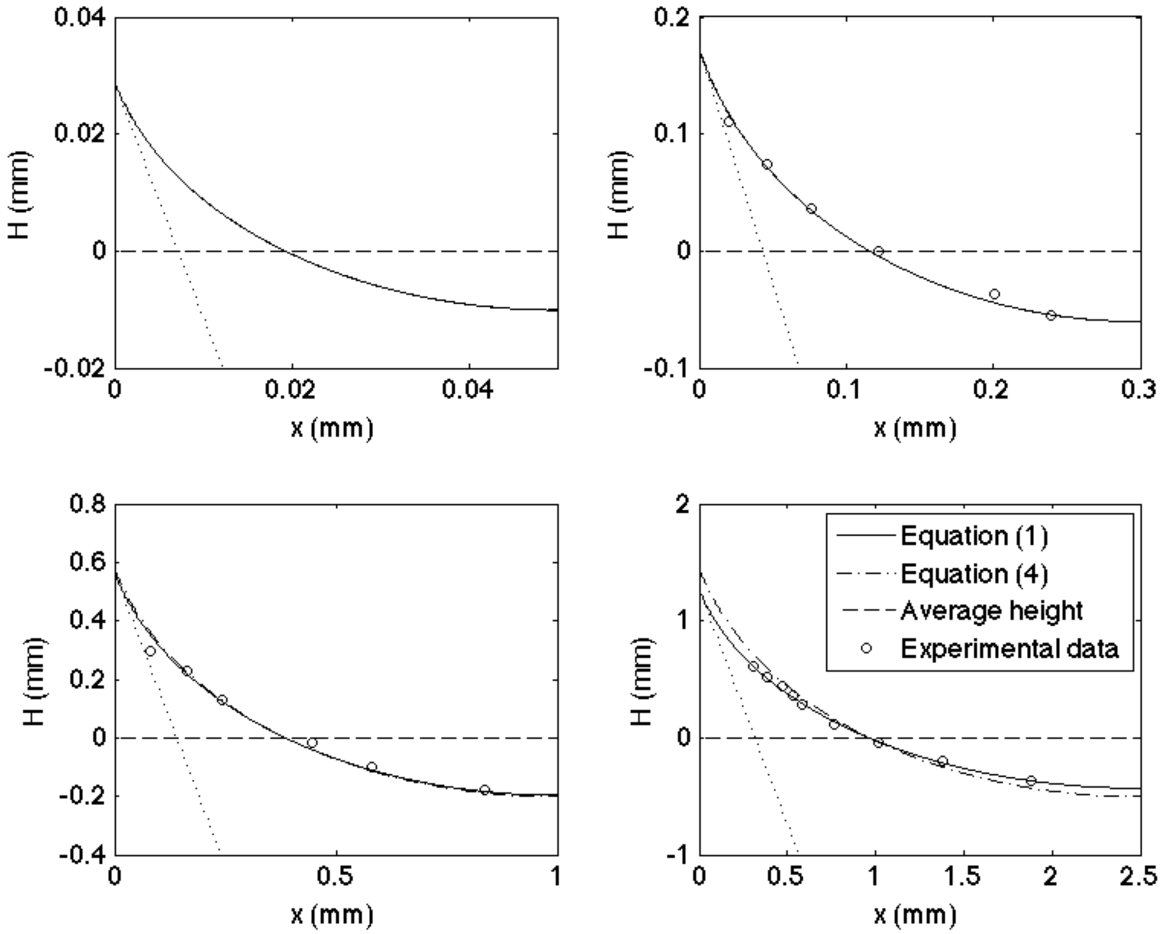

Figure 2.3: Calculated meniscus shapes for water confined between two vertical glass plates with spacing of 0.1, 0.6, 2.0 and 5.0 mm and measured air-water interface shapes in 0.6, 2.0 and 5.0 mm channels ($0 \leq x \leq w/2$). Note that $H(x) = h(x) - h_0$, where $h(x)$ is the meniscus shape function.

Table 2.1: Experimental conditions and fitted parameters

w(mm)	H(mm)	h(mm)	$\frac{h}{w}$	τ	$\frac{dp}{dz}$(pa m^{-1})
0.6	0.42	0.36	0.600	-0.136	-59.847
1.0	0.70	0.45	0.450	-0.083	-31.755
2.0	1.60	0.75	0.375	-0.059	-9.264
3.0	2.60	1.10	0.367	-0.054	-3.750
5.0	4.40	2.30	0.460	-0.075	-0.828

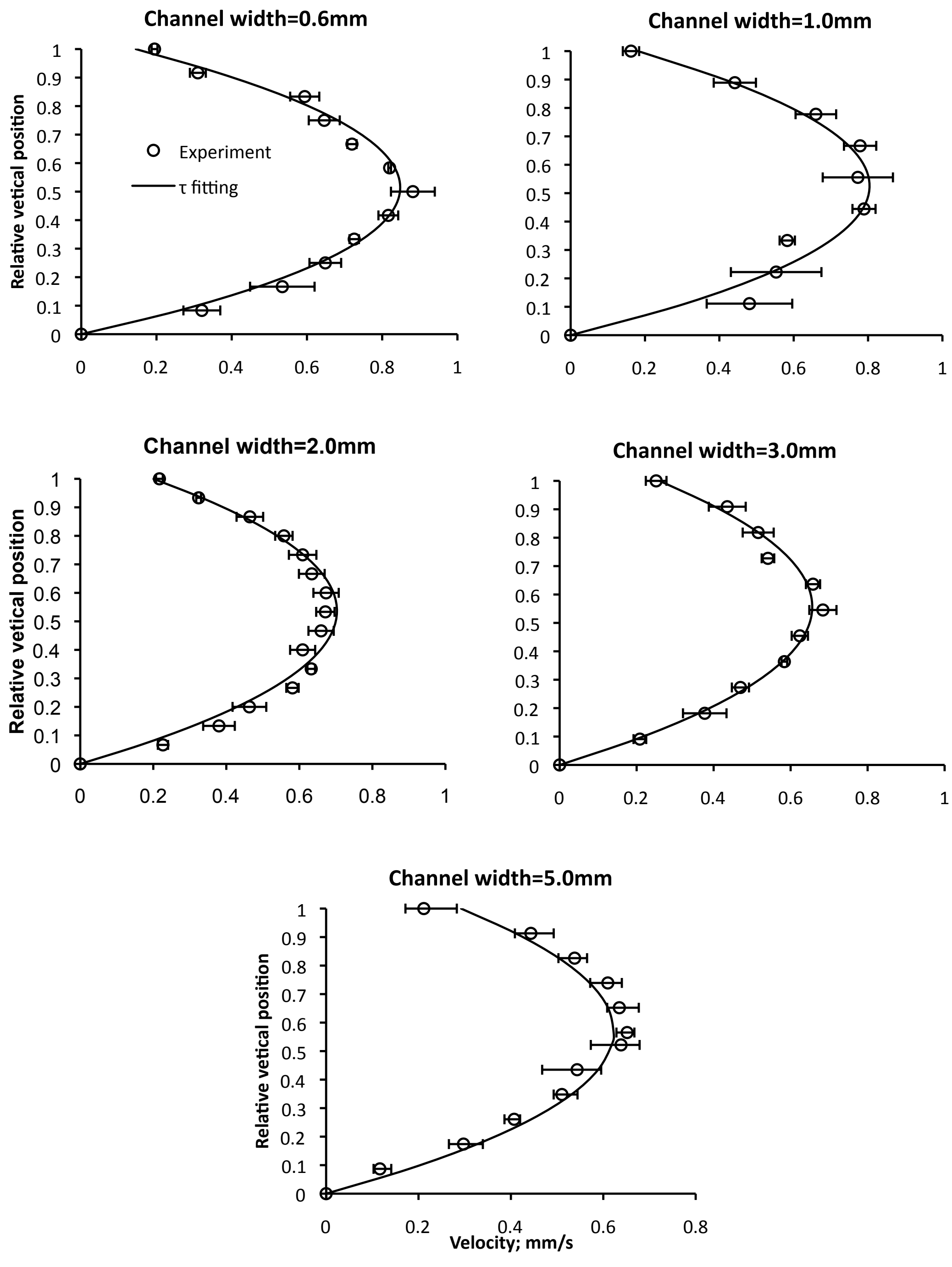

Figure 2.4: Experimental and theoretically fitted velocity profiles in the middle of the 0.6, 1.0, 2.0, 3.0, and 5.0 mm channels (mean velocity: $\sim$0.5 mm s^{-1}). The y-axis shows the relative vertical position, which is the measurement location normalized by water height. The error bars are based on three repeated runs.

2.7, $-\infty < \tau < 0$) at the air-water interface, fitted the solutions (equation 2.13) to experimentally measured profiles, and estimated surface shear stress values and the pressure drop for each channel (table 2.1). The theoretical and experimental velocity profiles matched very well (figure 2.4). In addition, for the same mean flow rate, the value of the dimensionless interfacial shear stress increased (i.e., became more negative from -0.059 to -0.136) as channel size decreased from 2.0 mm to 0.6 mm whereas it remained relatively constant for 2.0, 3.0 and 5.0 mm channels (table 2.1). Furthermore, the fitted pressure drop across each channel increased (i.e., became more negative from -0.8 to -59.8) as channel size decreased (table 2.1). These results indicate that the interfacial shear stress and thus the air-water interface mobility are functions of the channel size.

Our measurements show that the air-water interface confined in small channels was curved rather than flat (figure 2.3). Experimentally determined interfacial shapes for channel sizes of 0.1, 0.6, 2.0 and 5.0 mm were in reasonable agreement with calculated values using equation 2.1 with σ=72.2 m J m^{-2}, $\rho = 1000$ kg m^{-3}, $g = 9.8$ m s^{-2}, and $\theta = 14^o$. Moreover, for smaller channels with sizes 2.0 mm ($Bo \leq 0.144$), the interface shapes are similar to those approximated on the basis of circular arcs of equal sizes (equation 2.4). However, for larger channels with sizes ¿ 2.0 mm, the interfacial curvature decreased along the interface receding from the wall.

To evaluate the effect of boundary condition and interfacial shape on the flow characteristics in open microchannels, we performed theoretical calculations of 2D velocity distributions over a unit square domain for a flat (figure 2.5a - c) and a curved air-water interface (figure 2.5d - f) with an arbitrary curvature of $\kappa = 1.6$ for three boundary conditions at the air-water interface: no-slip, partial-slip and stress-free, respectively. Our analysis shows that the maximum normalized velocities were higher in channels with a flat air-water interface at 0.073, 0.082 and 0.114 for the three boundary conditions, respectively, than the corresponding values with a curved interface at 0.038, 0.043, 0.060. The increased shear stress associated with a curved interface decreased

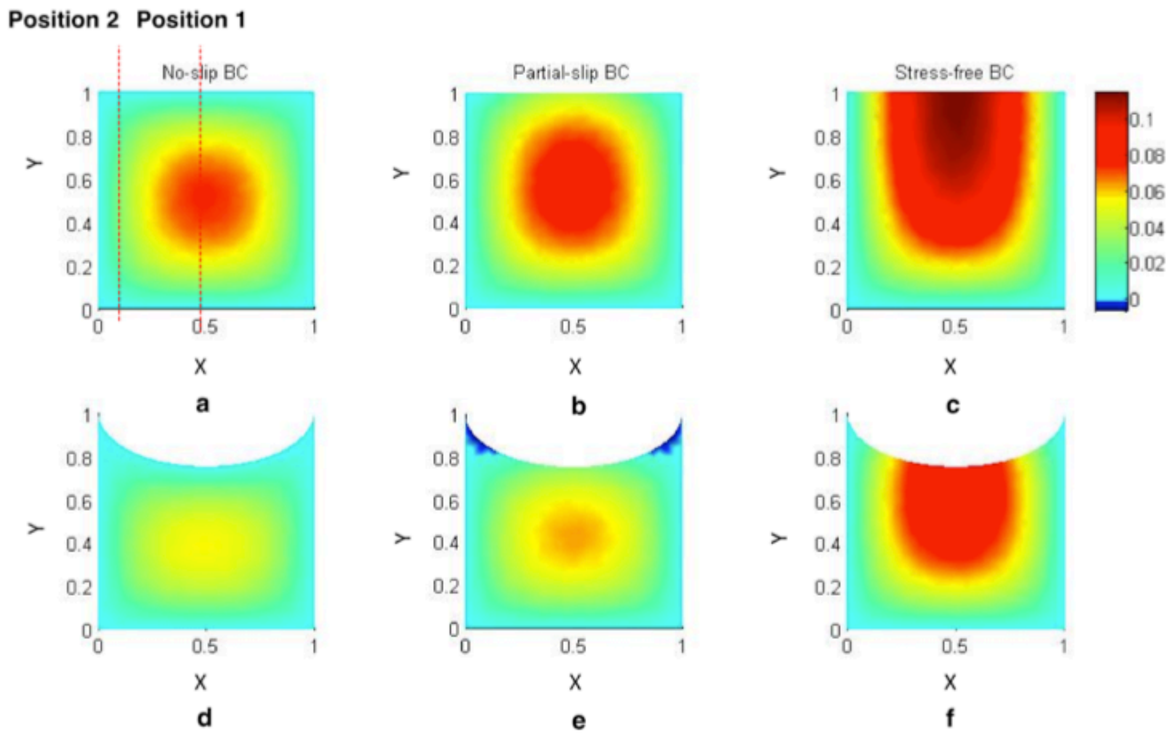

Figure 2.5: Two-dimension velocity distribution obtained by solving the equation of $\Delta^2 v = 1$ over a unit square domain for a flat (a - c) and a curved surface with a curvature of 1.6 (d - f). Boundary conditions applied at the interface were $u = 0$, $\tau = -0.2$, and $\tau = 0$ for no-slip, partial-slip and stress-free cases, respectively.

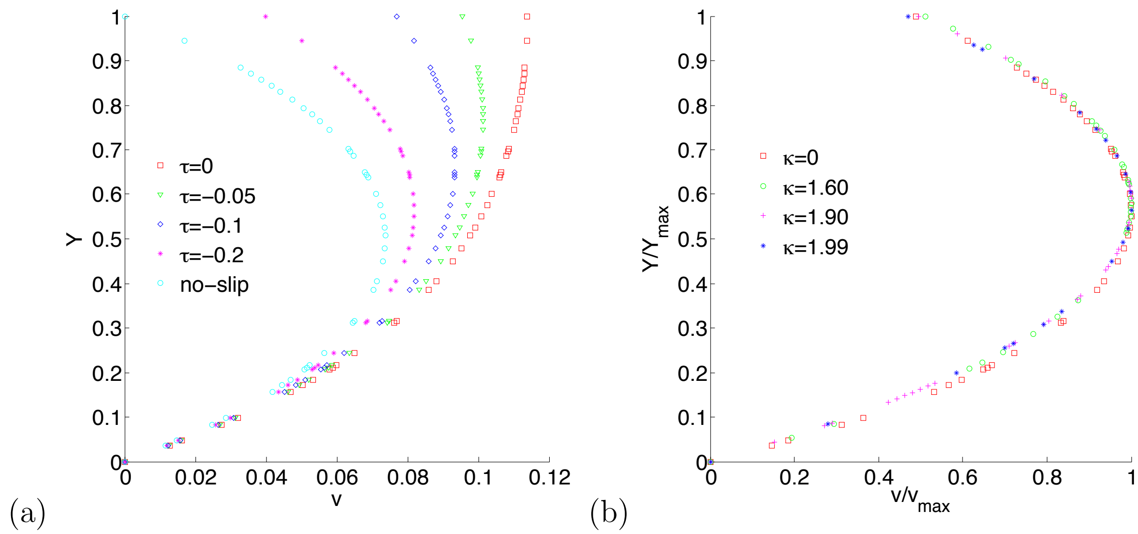

Figure 2.6: Theoretical velocity profiles at the center of the channels by solving the equation of $\Delta^2 v = 1$ over a unit square domain under different shear stresses (τ = 0, -0.05, -0.1, -0.2 and $u = 0$; $\kappa = 0$) and interfacial curvatures (κ = 0, 1.6, 1.9, 1.97; τ = -0.2).

the maximum flow velocity as well as lowered the location (i.e., was closer to the channel bottom) where the maximum velocity was measured. Figure 2.5e, calculated for flow with a curved air-water interface and a partial slip boundary condition, resembled most closely the experimentally measured 2D velocity map (figure 2.2).

Additional calculations compared the effect of interfacial shear stress (τ) and curvature (κ), respectively, on velocity profile in the center of the channel(figure 2.6). The results clearly show that, by changing the boundary condition from stress-free to partial-slip and to no-slip (i.e., τ = 0, - 0.05, -0.1, -0.2 and $u = 0$) the velocity profile changes its pattern from half parabolic to partially parabolic (the case similar to our experimental observation) and to parabolic (figure 2.6a; $\kappa = 0$), demonstrating how interfacial shear stress causes significant change in the flow field in an open capillary channel. However, at a given shear stress value (τ = -0.2), a change in interfacial curvature had no significant impact on velocity profiles and they essentially overlapped with each other (figure. 2.6b, κ = 0, 1.6, 1.9 and 1.97).

2.5 Discussion

2.5.1 Partial-slip air-water interface and origin of interfacial shear stress

The air-water interface has, in general, been treated as a stress-free boundary when modeling two-phase flow, as the density and viscosity of air are much lower than those of water. Our directly measured velocity profiles in open capillary channels suggest that the interface is not stress-free and is better represented by a partial slip boundary condition. Similar results in various experimental settings (e.g., open capillary channels, air bubbles, and moving meniscus) have been reported by others [22, 23, 24, 21].

Rigidity or limited mobility of air-water interfaces can result from surface tension gradients or the spatial variation of surface energy due to one or more mechanisms [72]. The presence of minor impurity in experimental systems could lead to a partial-slip or even a no-slip boundary condition at air-water interfaces [22]. The addition of colloid tracers to the fluid could be a potential source of interfacial contamination causing alternations in the interfacial rigidity in our study. However, surface tension measurements of colloidal suspensions at various concentrations (0 to 10 ppm) did not show surface tension changes in these samples. Additionally, our results and the derived interpretation of the effects of channel size on interfacial mobility would not be affected even if the added colloidal tracers slightly varied the fluid properties because the same tracer fluids were used in all experiments.

Our finding that interfacial shear stress increases with decreasing channel size suggests that airwater interfaces in small confined regions cannot be treated as entirely isolated from their surrounding no-slip solidwater interfaces and three-phase contact lines. In the capillary channels used in our study, the air-water interface near a channel wall tends to be stationary whereas it attains a larger velocity away from the wall. This lateral velocity gradient across from the channel wall to its center has to be balanced by a tangential hydrodynamic stress, which gives rise to finite shear stress at the interface [72]. As the spacing between confining walls decreases, the gradient increases and thus leads to larger interfacial shear stress. The dependence of the interfacial behavior of an airwater interface on its proximity to a solid surface has been speculated on or demonstrated in earlier studies [58, 21]. In particular, Chan et al.[58] reported that a bubbles air-water interface was stress-free when the bubble was far away from a TiO_2 substrate and became more rigid as it approached the substrate.

In addition to channel size, the fitted shear stress also depends on the interfacial curvature, which affects both the cross-sectional area and proportion of the air-water interface in the total length of mixed boundaries. As the channel size decreases, interfacial curvature and shear stress increase simultaneously, making it very difficult to differentiate their individual contributions to the increased interfacial shear stress. However, the variation of fitted interfacial shear stress for different sized channels was not expected to be due to the difference in interfacial curvature for two reasons. First, for channels with sizes <3.0 mm, the interfacial curvatures were all similar to circular arcs (figure 2.3). Second, the cross section used for fitting interfacial shear stress was assumed to be rectangular where the air-water interface was flat. The overlapping velocity profiles with different interfacial curvature values ranging from flat to $\kappa = 1.6$ (figure 2.6b) further indicate that neglecting the interfacial curvature was not the cause of the size effect on the interfacial shear stress.

Although the increased interfacial shear stress with decreasing size for channels with < 3.0 mm width was likely caused by the confinement of the no-slip walls, it remained relatively constant for the larger channels (table 2.1). This suggests that the physical origin of interfacial shear stress in small and large channels is likely different [25]. To compare the competing physical phenomena, we calculated dimensionless numbers (Ca, Bo, Re, and Pe) for all experiments (table 2.2). Especially insightful is the Bond number (Bo), which compares the relative contribution of gravitational and capillary force in affecting flow behavior in differently sized channels. The calculated Bo values increased as the channel size increased, indicating that capillarity dominates only on small scales and that on large scales, gravity makes a considerable contribution and therefore cannot be ignored. The calculation of meniscus shapes show that for channel sizes of < 2.0 mm the capillary force dominated and for larger channels with

Table 2.2: Dimensionless numbers

w[1]	a[2]	v_m[3]	Ca[4]	Bo[5]	Re[6]	Pe[7]
0.6	0.16	0.514	7.35×10^{-6}	0.050	0.084	1458
1.0	0.24	0.494	7.06×10^{-6}	0.139	0.116	1400
2.0	0.43	0.463	6.62×10^{-6}	0.557	0.197	1312
3.0	0.63	0.505	7.22×10^{-6}	1.254	0.319	1432
5.0	1.20	0.483	6.90×10^{-6}	3.484	0.576	1369

[1] the width of the channel (mm);
[2] the characteristic length of the channel (mm);
[3] the mean velocity of flow (mm s^{-1});
[4] the Bond number $Bo = \frac{\rho g a^2}{\sigma}$, a is the characteristic length of the channel (mm), and $a = \frac{wh}{2h+w}$, h is the height of liquid-filled area (mm). ρ is the density (kg m^{-3}) of bulk phase;
[5] the capillary number $Ca = \frac{v_m \mu}{\sigma}$, ρ is the viscosity (N s m^{-2}) of bulk phase;
[6] the Reynolds number $Re = \frac{a v_m \rho}{\mu}$;
[7] the Peclet number $Pe = \frac{2 r v_m}{D_0}$, D_0 is the diffusion coefficient of particles with radius of r (m);

sizes > 2.0 mm, interfacial curvature was affected by both capillarity and gravity. The commonly used criterion for distinguishing between small and conventional size channels in engineering applications is 3 mm [73]. This coincides with the results from the calculation of meniscus shapes, as well as the interfacial shear stress fitted by experimental data, where the interfacial shear stress increased as the channel size decreased when channel size was less than 3mm. The shape of the cross section, the roughness of the channel walls, and the presence of bends or a small disturbance at the entrance were proposed as possible causes of unequalized shear stresses on both sides of the channel and of the maximum velocity below the surface [74]. This has also been observed in open water systems such as rivers and streams where the maximum flow velocity often occurs at 1/3 depth below the water surface [25, 75], with a typical flow profile similar to that in figure 2.5b.

2.5.2 Flow pattern affected by interfacial shear stress

The importance of whether fluid-fluid interfaces during flow in porous media are rigid or mobile has been discussed in the context of flow in porous media [50, 76, 77]. It has been suggested that finite velocities exist at fluid-fluid interfaces and they affect the macroscopic permeability of the media [76]. Our study provides experimental evidence that, for flow with mixed boundaries where the air-water interface is bounded by no-slip solid surfaces, the boundary condition at the air-water interface would likely change with the pore size to become more rigid as pore size decreases. Our results suggest that treating the interface as stress-free would lead to an overestimation of macroscopic permeability.

We show in this study that both the boundary condition (interfacial shear stress) and interfacial curvature affect two-phase flow and transport. Flow resistance β (or friction factor), defined as [55, 59]:

$$\beta = \frac{w^2}{\mu v_m}(-\frac{dp}{dz}) \tag{2.14}$$

where v_m is the mean flow velocity (m s^{-1}), is frequently used to characterize flow efficiency in systems such as capillary or microfluidic channels. This relationship indicates that the flow resistance increases with decreasing mean flow velocity, which is in turn controlled by the interfacial shear stress. In microchannels where the surface area to volume area ratio is large, interfacial shear stress contributes to increased flow resistance and leads to a decreased effective slip length [61]. Interfacial shear stress is therefore considered an important parameter in the design of micro- and nano-fludic channels. For example, by making channel surfaces rough, i.e., making them superhydrophobic by trapping air and creating air-water interfaces, flow resistance can be reduced and effective slip length can be increased. Numerical simulations of the effective slip length have been found to overestimate the total effective slip length [55, 25, 73]. The overestimation has been attributed to treating the liquid-air interface as flat, thus neglecting interfacial curvature. Our analysis suggests that treating the interface as stress-free thus ignoring interfacial shear stress may be another source of overestimation in previous studies.

The observed reverse flow (i.e., the direction of flow is opposite to that of the bulk flow, see Appendix C) in the contact line region also likely resulted from the interfacial shear stress that originated from adjoining channel walls. This conclusion is consistent with our theoretical analysis where reverse flow along the contact lines was generated by solving the Stokes equation with a partial-slip boundary and a curved interface (figure 2.5e), indicating that the generation of reverse flow can be a direct result of the altered interfacial shear stress at a curved interface. By imposing different values of the interfacial shear stress on flow in a wedge, Su et al. [60] showed the occurrence of reverse flow near the interface when the shear stress was opposing the flow direction. The phenomenon of reversed flow in the contact line region has been reported in the literature, which was attributed to asymmetric flow around the gas phase or Marangoni effect [21] due to local variations in the interfacial tension or temperature. Although the possibility of thermal Marangoni flow due to heat emanating from the microscope could not be completely ruled out, this effect was likely very small due to the short duration of the experiments. Our results indicate that the combination of interfacial shear stress and curvature, both characteristics of microscale flow, are the two essential factors that can give rise to the reverse flow phenomenon.

2.6 Summary

We examined the boundary condition at the air-water interface and flow pattern on the microscopic scale in capillary channels that are representative of small isolated flow regions found in natural porous media. Experimentally measured velocity profiles showed that the air-water interface possesses some degree of rigidity that increases with increasing flow confinement (i.e., decreasing channel size). The observations can be described by the Stokes equation by invoking a partial-slip boundary condition at the air-water interface. The dominant effect of capillary forces in confined flow regions leads to the observed interfacial curvature and shear stress, which in turn lead to the non-stress-free air-water interface. These results suggest that conservation-based pore-scale models of multiphase flow that treat the air-water interface as wholly isolated from the surrounding solid-water interfaces (i.e., stress-free) would overestimate the flow rate in porous media. Therefore, a partial-slip boundary condition should be considered in describing the free air-water interface taking into account the effects from adjoining solid-water interfaces and the complex flow pattern in the contact line regions in microscale flow where the capillary force dominates. In addition, our study provides a new explanation for the reported overestimation of the slip length in microfluidic channels with superhydrophobic surfaces as well as new insight into how interfacial shear stress may generate reverse flow in the contact line regions. The improved physical understanding of surface/interface effects on flow behavior on the nano- and microscale is essential for an accurate quantification of a wide variety of multiphase problems in porous media as well as for the design and manipulation of flow in microfluidics.

Chapter 3

PARTIAL-SLIP BOUNDARY CONDITION AT AIR-WATER INTERFACE IMPROVES PREDICTION OF UNSATURATED HYDRAULIC CONDUCTIVITY

3.1 Introduction

Accurate determination of the unsaturated hydraulic conductivity (K_r) of a porous medium has been an active research topic in disciplines such as soil science, environmental engineering and petroleum engineering for decades [43, 8, 49]. Significant attention has been given to developing advanced hydraulic conductivity models because experimental determination of K_r is complicated and time-consuming. A common approach is to deduce K_r from water retention curve (i.e., pore-size distribution), supplemented by direct measurements of the saturated hydraulic conductivity (K_s) [40, 41, 42]. The models developed based on this approach link the macroscopic Darcy's law to microscale flow behavior, and have been shown to provide better predictions of K_r as compared with purely empirical models, such as the model in Gardner [78]. For example, the van Genuchten-Mualem model (VGM), which applies the Poiseuille's law to a series of parallel capillary tubes, has been widely used [42].

The VGM developed based on cylindrical tube pore space geometry give satisfactory estimation of water retention curves or hydraulic conductivity values only at high water saturations whereas large discrepancies exist when water saturation is low [45]. The models unsatisfactory performance was attributed to the oversimplified pore geometry, which does not allow for adequate account of the water retention and transport mechanisms. Tuller and Or [41] developed the triangular pore space model (TPSM), assuming a triangular pore geometry that better represents the real pore space than cylindrical tubes. The TPSM considers flow in the corners of angular pores as well as thin-film flow in slit-shaped area, and takes into account of the existence of residual liquid in the corners and slits after the pores are drained; therefore as an advantage, it enables quantifications of distinct flow characteristics during drainage or imbibition processes.

Accurate representation of pore geometries and the associated microscopic flow processes is the keys to the success of any physically based hydraulic conductivity models. Inaccurate and inadequate consideration of microscopic flow phenomena in the model could hinder the predictive capability considerably [49]. Flow at the microscale can be markedly different from the traditional descriptions of fluid dynamics at the conventional scale because surface effects play a dominant role at the microscale [20]. For example, recent studies revealed that a clean AWI was able to sustain stress due to the constraint of adjacent no-slip walls in open capillaries [21]. This observation is in conflict with the conventional assumption of a shear-free or perfect-slip boundary at a clean AWI [25]. As flow in unsaturated porous media takes place in highly interconnected and tortuous pore spaces surrounded by soil grains [50], it is reasonable to expect that the AWI is not stress-free in such restricted regions. Therefore, the common practice of treating the AWI as a shear-free boundary in existing hydraulic conductivity models (e.g., TPSM) may be a source of the observed discrepancies between model predictions and experimental measurements.

The main goal of this study is to demonstrate that representing a confined AWI as a partial-slip boundary improves the prediction of unsaturated hydraulic conductivity. We built the modeling framework on the basis of the TPSM by Tuller and Or [41], and verified the modified-TPSM based on a microscale experimental observation and numerical calculations of micro-flow along a corner. Three sandy soils were used to test the proposed model and the results were analyzed. In addition, comparison of modified-TPSM with the VGM was also discussed.

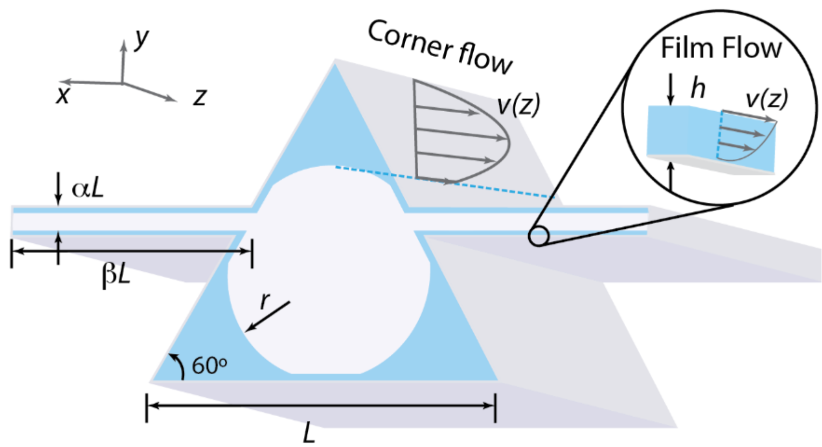

Figure 3.1: Pore space representation of the unit cell in the TPSM with a triangular central pore and slits connecting pores. The blue-colored area depicts the water-saturated region under the unsaturated condition. Representative velocity profiles $v(z)$ of corner flow and film flow are sketched.

3.2 Model Description

In this study, modeling of hydraulic conductivity was based on the framework of the TPSM developed by Tuller and Or [41]. In the TPSM, the pore space was represented by a bundle of unit cells, each consisting of a triangular large central pore and slit-shaped spaces representing the internal surface area between the central pores (figure 3.1). Based on the liquid configuration in both the angular and slit-shaped spaces, the water retention function and hydraulic conductivity functions accounting for duct, corner and film flow were derived. A detailed description of the TPSM is provided in the Appendix B. The AWI for corner flow was treated as a shear-free (perfect-slip) boundary in the TPSM. In the modified-TPSM developed in this study, the shear-free boundary condition was replaced by a partial-slip boundary condition. Specifically, the hydraulic conductance for corner flow was expressed with a dimensionless flow resistance ε (see equation B.7), and the value of ε was set as 31.07 in the TPSM [41]. In the modified-TPSM, the flow resistance ε was assumed to be a function of the saturation S of the porous medium: $\varepsilon = f(S)$.

The derivation of the analytical function $\varepsilon = f(S)$ based on the unit cell geometry defined in the TPSM involved three steps. First, the flow resistance ε for air and water two-phase flow with a partial-slip boundary condition at the AWI along a corner was computed to determine the relationship between ε and a normalized slip length ξ. Second, the dependence of ξ at the AWI on the length l of the microchannel was investigated in an open microchannel experiment. We defined l as the distance between the contact lines formed on each of the channel walls. Third, within a single cell, the degree of saturation (S) was approximately written as a function of the length l. The three steps are derived in more detail below.

3.2.1 Relationship between ε and ξ

In this section, flow of water along a predominantly air-occupied corner was solved numerically. Figure 3.2a depicts the geometry for a corner with a spanning angle of $\gamma = 60°$, as well as the AWI configuration with a contact angle of 0°. We denoted the length of each of the wetting walls as L', and radius of the AWI as r, which defined the flow domain. Because relatively large viscous forces are required to break up or significantly deform the interface, a fixed boundary was assumed to form at the AWI.

The Stokes equation was employed to describe the unidirectional flow, assuming that flow was dominated by the viscous forces and the inertial effects were negligible:

$$\mu \nabla^2 v = -\frac{dp}{dz} \tag{3.1}$$

where μ is the liquid viscosity (kg m^{-1} s^{-1}), and $\frac{dp}{dz}$ is the pressure gradient (kg m^{-2} s^{-2}).

We normalized the variables by the characteristic length L', $X = x/L'$, $Y = y/L'$, and $u = -v\frac{1}{\mu}\frac{dp}{dz}$, so the governing equation can be written accordingly:

$$\nabla^2 u = 1 \tag{3.2}$$

The solution of equation 3.2 depends on the boundary conditions considered at the corner walls and the AWI. The velocity at the wall was assumed to be zero according to the no-slip boundary condition:

$$u = 0 \text{ at } Y = 0 \text{ for } x \leq X \leq 1 \tag{3.3}$$

$$u = 0 \text{ at } Y = \sqrt{3}X \text{ for } 0 \leq X \leq 1/2 \tag{3.4}$$

The boundary condition at the AWI is the key input for solving the flow field and flow resistance. An AWI with limited mobility can be modeled by the Navier slip-boundary characterized by a normalized slip length ξ,

$$u = \xi \frac{du}{dn} \text{ at } (X-1)^2 + (Y - \frac{1}{\sqrt{3}})^2 = \frac{1}{3} \text{ for } 0 \leq X \leq 1 \tag{3.5}$$

The value of ξ indicates the amount of slippage at the boundary, and varies from 0 for a no-slip boundary to -∞ for a perfect-slip boundary condition, respectively.

The velocity distribution across the corner domain was solved using the PDE toolbox in Matlab for the defined boundary conditions, and the flow resistance was calculated by [59]:

$$\varepsilon = \frac{r^2}{\mu \langle u \rangle}(-\frac{dp}{dz}) \tag{3.6}$$

where $\langle u \rangle$ is the average flow velocity.

The mobility of the AWI changes with varying slip length ξ. Figure 3.2b depicts the calculated flow resistance for the intermediate range of the normalized slip length from 10^{-2} to 50, showing a linear relationship between the flow resistance ε and the logarithm of the reduced slip length ξs:

$$\varepsilon - 30.09 = 6.35\log(\xi) \sim log(\xi) \tag{3.7}$$

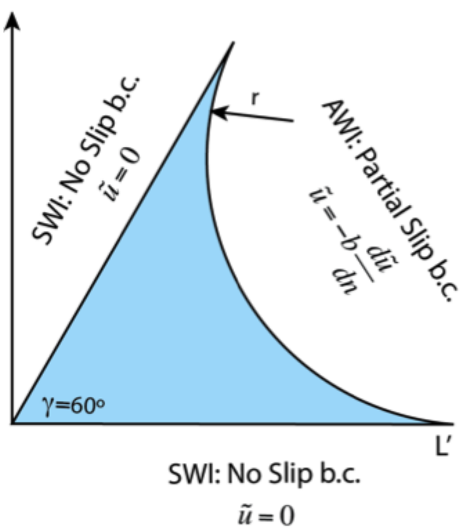

(a)

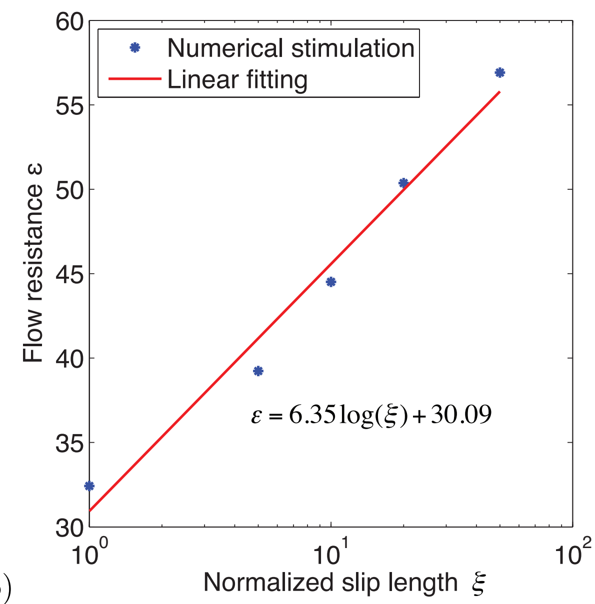

(b)

Figure 3.2: (a) Boundary conditions in corner flow calculation; (b) Calculated flow resistances with different normalized slip lengths at the AWI for corner flow.

3.2.2 Relationship between ξ and l

The slip length at AWI was quantitatively studied in a microchannel experiment. Using the method of μ-particle image velocimetry (μ-PIV), velocity profiles of flow along open rectangular microchannels with different sizes were constructed [79]. Assuming the incompressible viscous flow remained steady-state and only followed the longitudinal direction of the channel, the Stokes equation along with a no-slip boundary condition at channel walls and a partial-slip boundary condition at the AWI was used to model the flow system. The partial boundary condition at the AWI can be expressed with a tangential shear stress [79] or a limited slip length [22], both can be estimated by analyzing the measured velocity profiles. Zheng et al. [79] showed that the apparent tangential shear stress at an AWI increased with decreasing channel sizes (opening width). For generality, the opening width was characterized by a length l, which is defined as the distance between the contact lines formed at each of the channel walls. For rectangular channels, the value of l equals to their opening width of the channel. Here the slip length was solved and plotted versus the opening width (figure 3.3) showing that the slip length ξ increased with increasing l. Linear relationship between ξ and l was observed (figure 3.3):

$$\xi = 0.04l \sim l \tag{3.8}$$

3.2.3 Relationship between S and l

The degree of saturation (S) of a single cell at a certain matric potential (μ) can be expressed by the geometric parameters that define the unit cell (see equation B.3). In order to express S as a function of the radius of the AWI (r), we simplified the equation by neglecting the slit-shape area of the unit cell and water films. As a result, a linear function between S and r^2 was deduced as:

$$S \approx \frac{4r^2(3\sqrt{3} - \pi)}{L^2} \sim r^2 \tag{3.9}$$

(a)

(b)

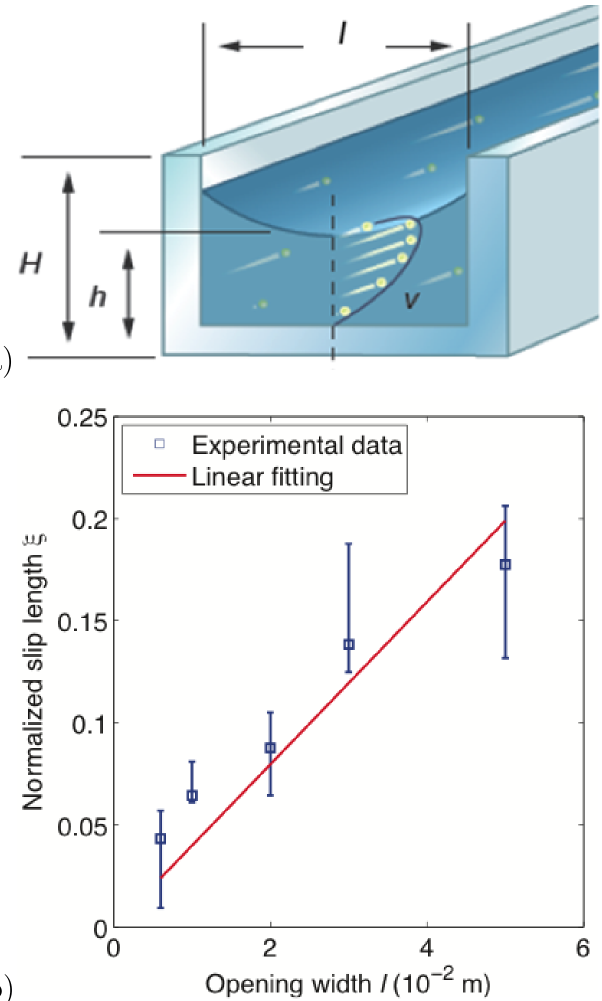

Figure 3.3: (a)Schematic drawing of flow through the microchannel used in the experiment; (b) Normalized slip length at AWI versus the opening width of the channel in the microchannel experiment.

In the unit cell, the radius of the AWI determined the value of l assuming the contact angle was 0°, and thereof, l was linearly related to the saturation of the unit cell:

$$l = \frac{\sqrt{3}}{2} r \sim \sqrt{S} \tag{3.10}$$

Substituting equations 3.8 and 3.10 into equation 3.7, the flow resistance could be related to the saturation as $\varepsilon - 30.09 \sim \log(\sqrt{S})$. In the modified-TPSM, this equation was applied to take into account the effects of the limited slip at the AWI. The slope of 10 (therefore, $\varepsilon = 30.09 + 10\log(\sqrt{(}S)))$ was chosen based on a prior test for the experimental data.

3.3 Model Testing

3.3.1 Testing data sets

The modified-TPSM was tested against experimental data obtained from the Unsaturated Soil Hydraulic Database (UNSODA) [80]. The key physical properties of the selected soils are summarized in table 3.1. These soils were selected because they have fairly complete data sets of both soil water retention curve (drainage process) and hydraulic conductivity measurements.

3.3.2 Illustrative examples

A flowchart for prediction of hydraulic conductivity using the modified-TPSM is shown in figure 3.4. The input data for hydraulic conductivity include three geometric parameters (L, α, β) defining the single pore space. Because no direct measurement was availabel for L, α, and β, these parameters were estimated using the measured water retention curve. The curve fitting was conducted with an evolutionary algorithm CMA-ES (Covariance Matrix Adaptation Evolution Strategy) [81]. We used the same set of geometric parameters in the TPSM and the modified-TPSM because the differ only in the hydrodynamic consideration. In addition, the measured water retention curve was also fitted to the VGM for each soil for comparision.

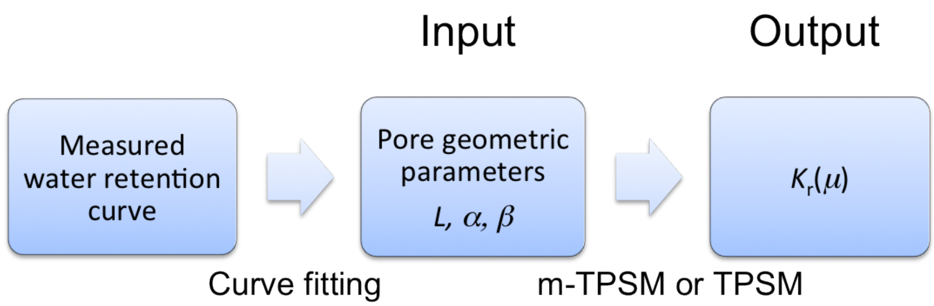

Figure 3.4: Flowchart for the prediction of hydraulic conductivity using the TPSM or the modified-TPSM (m-TPSM).

The goodness of model performance was quantified by the root mean square error ($RMSE$), which is the overall magnitude of the differences between the observed and predicted data. It was noted that the relative hydraulic conductivity was log-transformed to ensure that the complete range of hydraulic conductivity was well represented. The values of RMSE for water retention curve and hydraulic conductivity were computed as:

$$RMSE_\theta = \frac{1}{N}\sum_{i=1}^{N}[\theta_w - \hat{\theta}_w]^2 \tag{3.11}$$

$$RMSE_K = \frac{1}{N}\sum_{i=1}^{N}[\log(K_w) - \log(\hat{K}_w)]^2 \tag{3.12}$$

where N is the number of the observations in the data set, θ_w and K_r are the predicted water content and relative hydraulic conductivity, and $\hat{\theta}_w$ and $\hat{K}_w$ are the observed water content and relative hydraulic conductivity, respectively.

3.4 Results and Discussion

3.4.1 Soil pore size

The estimated values of the model parameters in the modified-TPSM, the TPSM and the VGM from the water retention curves were given in table 3.1. Water retention curves, which were used as indirect input information for prediction of hydraulic conductivity, reveal estimated pore space sizes. The average central pore sizes were all smaller than 1 μm for the three targeted soils (table 3.1). The values of slit-spacing ratio (α) were at the order of 10^{-2} or 10^{-3}, indicating that the slit spacing was less than 10 nm. The estimated single pore size indicates that soil pores remained at the microscale, thus liquid retention and flow were dominantly controlled by surface forces and viscosity [20].

3.4.2 Model comparisions

As shown in figure 3.5, the TPSM fitted the water retention curve remarkably well for Berlin sand. Both the TPSM and modified-TPSM were in good agreement with the measured hydraulic conductivity. As for Lille sand, because of uniform pore-size distribution assumed in TPSM, it was difficult to fit the initial end of the water retention curve with the TPSM (figure 3.6). Nevertheless, the model parameters values obtained from the water retention curve lead to a reasonable agreement of hydraulic conductivity with the measured data set. The VGM showed a perfect fit for the water retention curve; however, the prediction of hydraulic conductivity considerably deviated from the measurements at the low saturation range. Figure 3.7 depicts the results for Poppel sand, showing that albeit the VGM was in excellent agreement with the water retention data, large deviation was found for hydraulic conductivity at the dry end. Reasonable agreement with water retention and hydraulic conductivity data was found using the TPSM. Importantly, the modified-TPSM captured the trend of the drying end for hydraulic conductivity and provided the best fit among the three models. The goodness of model performance was also evaluated by the calculated $RMSE_K$ (table 3.2). The smallest $RMSE_K$ was achieved using the modified-TPSM among the three models, indicating that the modified-TPSM could improve the prediction of unsaturated hydraulic conductivity.

The improved prediction of hydraulic conductivity using the modified-TPSM as compared with that of the TPSM was attributed to the detailed microscopic flow processes considered in the modified-TPSM. Specifically, the modified-TPSM considered a

Table 3.1: Soil properties and estimated parameters from water retention curve using the TPSM and VGM

Soil code	Name	θ_s (cm^3 cm^{-3})[1]	K_s (cm d^{-1})[1]	TPSM			VGM[2]		
				L	α	β	a	n	θ_r (cm^3 cm^{-3})
1460	Berlin sand	0.261	251	11.46	2.44	7.65	3.280	2.267	0.014
4000	Lille sand	0.387	95.8	4.59	0.17	18.02	2.342	2.244	0.045
4132	Poppel sand	0.332	79.8	4.59	4.50	3.82	1.016	4.105	0.036

[1] Source: Data from UNSODA [80].

[2] The VGM for water retention curve is written as $\frac{\theta(\mu)-\theta_r}{\theta_s-\theta_r} = \frac{1}{1+[a(-\mu)^n]^{1-1/n}}$, where θ_s is the saturated water content (cm^3 cm^{-3}); θ_r is the residual water content (cm^3 cm^{-3}); a is a parameter related to the inverse of the air entry suction; n is a measure of the pore-size distribution.

Table 3.2: Calculated root mean square errors ($RMSE$) for water retention curve and hydraulic conductivity using the modified-TPSM (m-TPSM), TPSM and VGM

Soil code	$RMSE_\theta$		$RMSE_K$		
	TPSM	VGM	m-TPSM	TPSM	VGM
1460	0.005	0.005	0.532	0.707	1.278
4000	0.028	0.003	1.411	1.449	3.339
4132	0.014	0.003	2.117	2.566	6.181

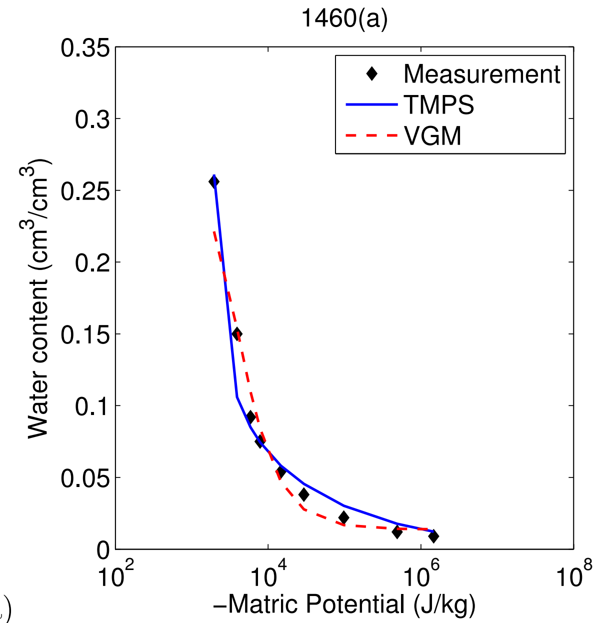

(a)

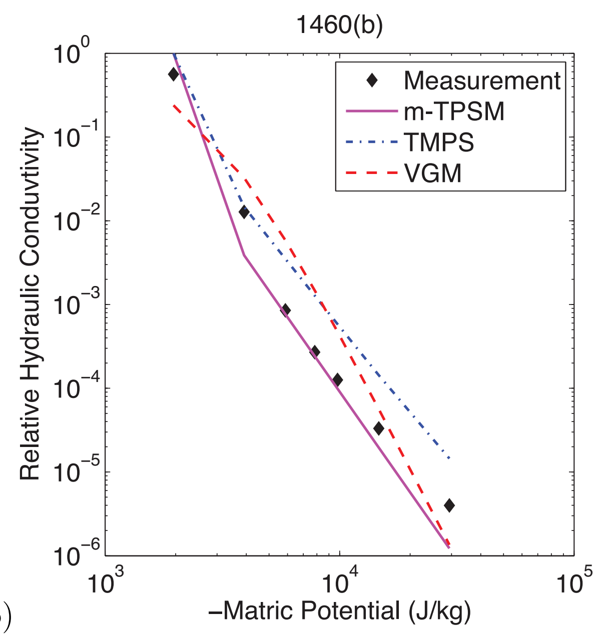

(b)

Figure 3.5: Measured and calculated water retention curves (a) and relative hydraulic conductivity (b) for Berlin sand.

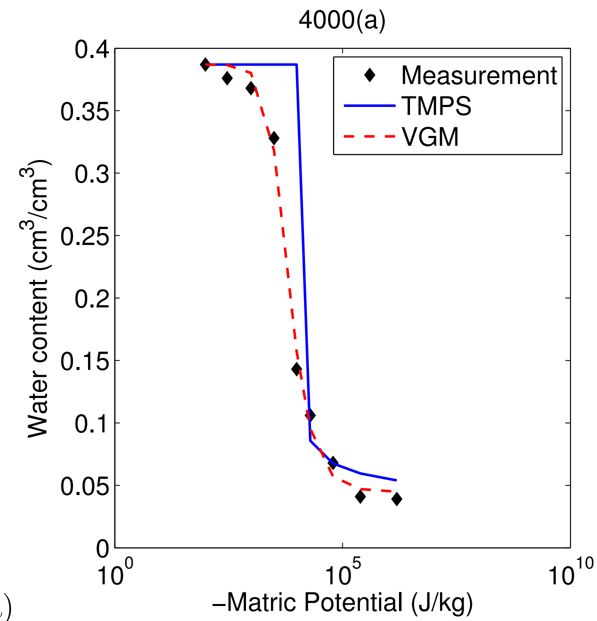

(a)

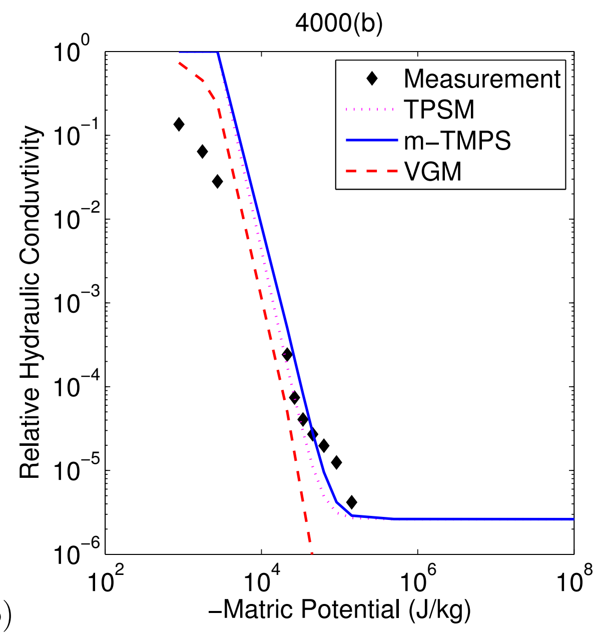

(b)

Figure 3.6: Measured and calculated water retention curves (a) and relative hydraulic conductivity (b) for Lille sand.

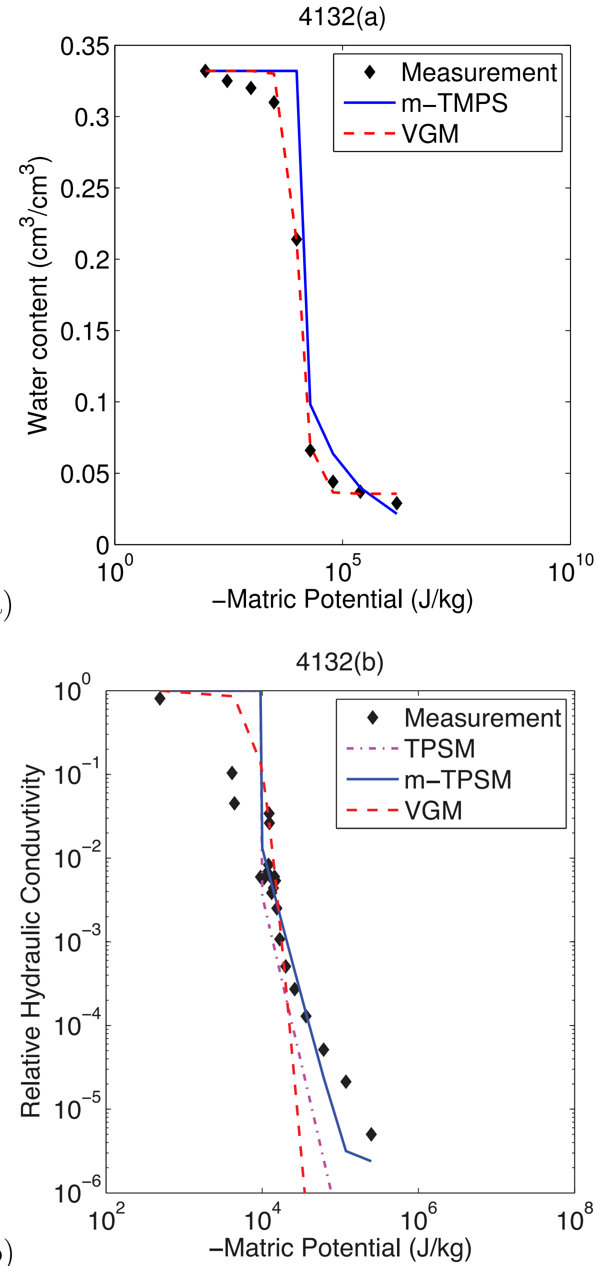

(a)

(b)

Figure 3.7: Measured and calculated water retention curves (a) and relative hydraulic conductivity (b) for Poppel sand.

partial-slip boundary condition at the AWI for corner flow while a perfect-slip boundary condition at the AWI was used in TPSM [41]. The results suggested that the AWI was more accurately represented by a partial-slip boundary condition. The partial-slip boundary condition at the AWI describes the transfer of momentum between AWIs in multiphase flow. Conventionally, the interaction between air and water phase was neglected assuming a perfect-slip boundary condition at the AWI [41]. Nevertheless, the driving force at the interface, which is known as viscous coupling, could lead to a considerable effect on the permeability of each phase of multiphase flow in porous media at both the microscopic and macroscopic scales [82]. The slip boundary condition was also applied in other two-phase flow system. [83] used a model assuming ow in capillary tubes with a slip boundary condition to predict the permeability of oil-water two-phase flow, and concluded that slip was the explanation for the observed “lubricating effect”. We demonstrated in this paper that the partial-slip boundary condition described the pore-scale AWI more accurately than the perfect-slip boundary condition.

Water retention curve and hydraulic conductivity were also calculated according to VGM for comparison. The VGM fitted the water retention curve considerably well, however, prediction of hydraulic conductivity by the VGM had relatively large deviations at low water saturations (table 3.2). The deviations could relate to some of the drawbacks of the cylindrical capillary-based parametric model. First, the VGM considers the residual water content as a fitted parameter, and assumes that flow process is negligible at water content smaller than the residual value [42]. However, the residual water content was not consistently recognized physically, and water flow was observed under the condition near the residual water content [45]. Second, the cylindrical-capillary based model assumes that water is either completely filled or completely emptied in capillary tubes, which neglects the effects of the adsorptive forces in retention of water films [41]. However, the adsorption is regarded as the dominant force that holds water at very dry conditions [84]. Third, the VGM is based on Poiseuille flow where a linear relationship between the driving pressure and flow rate is derived. The existence of adsorptive films or the momentum transfers though interfaces may violate the linearity as simplified by Poiseuille flow assumption [8]. We compared the VGM to the current modified-TPSM model, and results suggested that realistic pore representation and accurate flow characterization should be considered maximally possible in hydraulic conductivity models.

3.4.3 Effects of local slip length at AWI

The local slip length at AWI was assumed to be a function of saturation in the modified-TPSM (equation 3.8). This assumption was based on the microscopic channel flow experiment [79], where the slip length at the AWI was resolved by measuring the flow field of water flowing through open channels with different opening widths. The experiment mimics the multiphase flow scenario in porous media where liquid-liquid interfaces are presented being bounded by the surrounding solid matrix surfaces. The decreasing slip length of the AWI as increasing opening width (figure 3.4) indicates that limited mobility of the AWI was likely due to being confined in restricted spaces. Consequently, continuous drainage of water from porous media lead to water retained in smaller corners, thus it is reasonable to assume the slip length of AWI decreases as water saturation decreases.

Studies have been conducted on characterizing the hydrodynamic boundary condition at the liquid-liquid interface, most of which attributed the limited mobility of AWI to the presence of contamination [72, 24]. Chan et al. [58] found that the AWI of a bubble was more rigid as it approached a TiO_2 substrate as compared to that if departing (from the substrate) scenario, indicating the effect of restricted space on the rigidity of the AWI. However, the relationship between the rigidity of AWI and the distance away from the substrate was not quantified. We used an empirical function in the modified-TPSM based on the experimental results from a relatively narrow range of length scales, because there was only very limited number of studies that quantified the rigidity of AWI due to the restricted space. It should be noted that the fitted parameters in equation 3.8 are likely to be case-dependent as they may be affected by fluid properties and surface characteristics of the channel wall. A general relationship between the slip length and pore size needs to be further tested.

Flow resistance for the corner flow with a partial-slip AWI was numerically calculated in this study (figure 3.3). The problem of wetting-phase flow along a corner is also important to oil trapping, foam drainage or capillary imbibition. The dependence of flow characteristics on the factors as flow geometry, corner angle, and interfacial shear stress have been previously investigated [59, 61]. Ransohoff et al. [59] studied the surface shear viscosity effect, and the dimensionless flow resistance was found to increase with increasing surface shear viscosity. Instead of using the surface shear, we used the slip length to characterize the mobility of AWI in this study, and our results showed a consistent trend that the flow resistance increased as the slip length at the AWI decreased (figure 3.3).

3.5 Conclusions

In this study, the modified-TPSM was developed to calculate the unsaturated hydraulic conductivity based on the framework of the TPSM. The modified-TPSM considered a partial-slip boundary condition at the AWI for corner flow while a perfect-slip boundary condition was used in the TPSM. Results of the predicted relative hydraulic conductivity for three sandy soils showed that the modified-TPSM could best fit the experimental data, compared with the TPSM and VGM. Our study clearly demonstrated that the AWI presented in porous media at unsaturated conditions should be described by a partial-slip boundary condition rather than a perfect-slip boundary condition. Consequently, unsaturated hydraulic conductivity models for multiphase flow developed based on pore-scale flow processes should consider the interfacial interaction between phases.

Combining the results from the microchannel experiment and numerical simulations for corner flow, an analytical expression for the dimensionless flow resistance was derived. The analytical expression from pore-scale results can be directed utilize for sample-scale hydraulic conductivity calculation. The microchannel experiment provided direct evidence for a partial-slip AWI, which contributes to characterization of the momentum transfer of interface between phases. The solution to the corner flow problem, which was solved in this paper, may be applied to a wide variety of capillary problems of interest. For example, the dimensionless flow resistance can be used for problem of snap-off of a gas bubble in a constraint pore [85] and in foam drainage [59, 86].

We restricted our modeling to sandy soils, because the TPSM with a uniform pore-size distribution was able to reasonably fit the water retention curve of a porous medium with a relatively narrow pore-size distribution, such as sandy soils [41]. Another reason is that even when the TPSM including a statistical pore-size distribution function is considered, it always fails to describe experimental data of water retention curve in the intermediate saturation range due to the limited flexibility of probability function used in the model [84]. To solve the problems with heavier-textured soils, a promising approach is to develop pore space models that can better represent natural porous media. There has been increasing interest in applying the pore-network model to study hydraulic properties, therefore, incorporating the partial-slip boundary conditions at liquid-liquid interfaces in such models may provide further improvement in predictions of hydraulic properties even for heavier-textured soils, but is out of the scope of the present study.

Chapter 4

CONSIDERING SURFACE ROUGHNESS EFFECTS IN A TRIANGULAR PORE SPACE MODEL FOR UNSATURATED HYDRAULIC CONDUCTIVITY

4.1 Introduction

A common approach of modeling water movement in porous media is to use Richards equation, where reliable prediction requires an accurate and effective description of water retention curve and hydraulic conductivity function. This approach is based on the continuum theory where water retention curve and hydraulic conductivity function are established based on the concept of representative elementary volume (REV). Many geological formations and soils contain micro-scale heterogeneities on surfaces of solid phase at a length scale below the REV scale. However, prevailing approaches for modeling the water retention curve and hydraulic conductivity function have limited representation of the microscale heterogeneities (e.g., surface roughness).

Several past studies have conceptualized soil as a bundle of cylindrical capillaries (BCC) [44, 4, 40, 42]. The BCC-based water retention and hydraulic conductivity models, e.g., van Genucthen-Mualem model (VGM), are most widely used in the practice of hydrology or environmental engineering, due to their simple mathematical formulation. However, the BCC-based models could not be rigorously verified against experimental data at low water contents [45]. The models' unsatisfactory performance is attributed, in part, to the oversimplified pore geometry, which does not allow for adequate account of water retention and transport mechanisms [41].

The BCC-based models can be improved by an alternative triangular pore space model (TPSM), in which the pore space is represented by a triangular central pore attached to slit-shaped spaces [41]. The TPSM enables dual occupancy of the pore space with water and air, as water remains in corners after the center pore is drained, or accumulate in corners before central pore is completely filled during imbibition. Another advantage of the TPSM is that film flow on planar surfaces is controlled by adsorptive force so that both adsorption and capillary processes are accentuated. However, the TPSM often had poor predictions in the intermediate range of saturation in the water retention curve, which was attributed to the limited flexibility of the applied pore size distribution function [84]. Other BCC-based models were developed accounting for water adsorption and film conductivity [87, 84, 88, 89, 90]. In general, the BCC-based models and the TPSM assume ideally smooth solid surfaces in the derivations of water retention curve and unsaturated hydraulic conductivity. Ignoring surface roughness may be associated with errors in water retention curve and hydraulic conductivity modeling.

Flow along rough fracture surfaces in unsaturated fractures has been found to be sensitive to surface roughness. Or and Tuller [91] developed a rough fracture surface model with a tractable geometry for calculations of surface liquid retention and hydraulic conductivity. In their model, surface roughness was represented by a statistical distribution of pits. Water storage on the surface and hydraulic conductivity were calculated, which were in excellent agreement with the experimental data. However, the surface fracture model does not consider flow between two surfaces, which is an essential element for flow in porous media. Recently, pore network models have been used as a platform to investigate surface heterogeneity effects [92, 93, 94]. In the pore network models, soils are represented by pore bodies connected to each other through pore throats. The pore network models provide an elegant way to simulate multiphase flow, and they are potentially powerful tools [46, 47]. Nevertheless, the small representative sample volume (usually from 1 mm^3 to few mm^3) limits the applicability of these models to large-scale problems [48].

In this study, we propose a new model for calculating water retention curve and unsaturated hydraulic conductivity considering surface roughness effects. Sensitivity analysis was conducted to test the model robustness. To further demonstrate its capability, the model was applied to fit water retention curves and to predict hydraulic conductivity of differently textured soils. We also explored the relationship between a key model parameter and soil physical properties from the available soil database.

4.2 Model Description

The proposed roughness-TPSM (R-TPSM) assumes that soil pores are composed of a bundle of capillaries with triangular cross sections and with a series of statistical pore size distribution. The description of the model includes three parts: (1) the single pore geometric representation as well as the water retention curve and hydrodynamic consideration for a single pore; (2) the pore size distribution function; (3) upscaling of the pore-scale water retention curve and hydraulic conductance to the core-scale.

4.2.1 Single pore representation and calculation

4.2.1.1 Single pore geometry

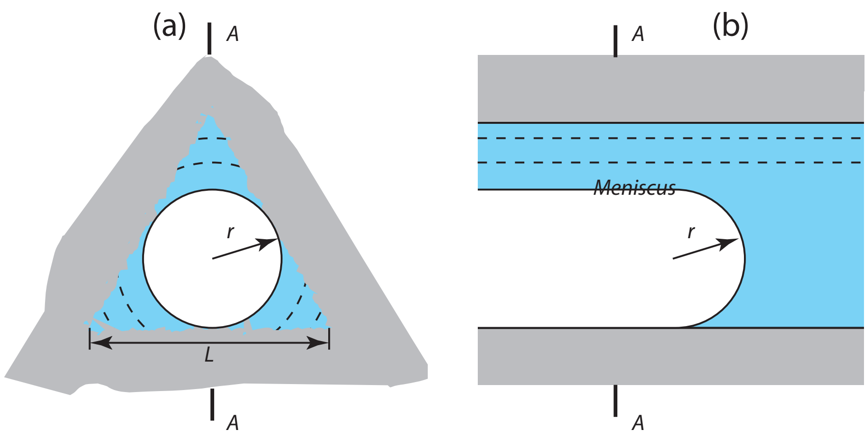

Figure 4.1: Schematic of the cross-section (a) and longitudinal section (b) of A-A in a single pore space representation. Increase in arc menisci curvature at corners during drainage is shown in (a). L is the equivalent side length. Roughness features are shown on the walls of the pore, X is the roughness factor defined as the ratio of the actual length of the wall L_a to the equivalent length L assuming the wall is smooth.

In the R-TPSM, a single pore space is represented by a capillary tube with a triangular cross section. We assume that the surface of the tube wall is rough, so that a single pore is characterized by an equivalent side length L and a roughness factor X (Fig. 4.1a). The roughness factor X is defined as the ratio of the actual length of side L_a considering surface roughness to the equivalent length L assuming the wall is smooth. The basis for defining X is that liquid film can expend over pits and bumps of the solid surface if the surface is not completely smooth. The roughness factor also accounts for liquid film adsorbed on the internal surface of porous media. Since all natural soil surfaces are rough, a roughness factor will be always greater than 1 for natural soils.

4.2.1.2 Liquid configuration at equilibrium during drainage and imbibition

Liquid saturation of a single pore involves different filling stages during drainage or imbibition. We consider a tube with a triangular cross section that is initially filled with a perfect-wetting liquid where the liquid drains from one end (Fig. 4.1b). The removal of a very small amount of liquid at the tube entrance causes a rise of capillary pressure, thus an invading meniscus is formed at the other end. When the suction increases (i.e., the matric potential becomes more negative) and reaches the threshold of μ_d, the liquid is displaced by the gas phase from the central region, leaving liquid wedges in the corners and liquid film on the solid wall. Away from the invading meniscus, the liquid-gas interface in the plane of the tube cross section can be approximated as a circular arc. The curvature of the arc increases and the thickness of liquid film decreases as the suction continues to increase. The gravitational effects are neglected because the tube size is small, thus the curvature remains constant at a given matric potential.

During the imbibition process, the tube is relatively dry at the beginning, where liquid films are adsorbed on the surface and liquid wedges are formed at the corners. As the suction increases to a critical value μ_i, the accumulation of liquid causes the circular arcs to begin to touch each other, followed by a spontaneous filling of the pore (i.e., the pore snap-off). The threshold suction/matric potential μ_i is different from the threshold μ_d during drainage, which is the main mechanism causing hysteresis between imbibition and drainage.

In the R-TPSM, both capillary and adsorptive forces contribute to liquid retention under unsaturated conditions. The thickness of a liquid film h and the curvature of liquid-gas interface of a liquid wedge $1/r$ are determined unitarily by the matric potential μ. Assuming the adsorption of liquid films is controlled only by the van der Waals interaction between the liquid and solid surface [41], film thickness h absorbed on a planar surface is calculated as a function of μ as:

$$h(\mu) = \sqrt[3]{\frac{A_{svl}}{6\pi\rho\mu}} \tag{4.1}$$

where A_{svl} is the Hamaker constant for the solid-gas interaction through the intervening liquid (J); ρ is the density of the liquid (kg m^{-3}).

The radius of the curved liquid-gas interface r is expressed as a function of μ based on the Young-Laplace relationship:

$$r(\mu) = -\frac{\sigma}{\rho\mu} \tag{4.2}$$

where σ is the surface tension of the liquid (N m^{-1}).

4.2.1.3 Water retention curve for a single pore

A pore is completely filled before (or after) the pore snap-off during drainage (or imbibition), so the saturation is $S_w = 1$. Under unsaturated conditions, S_w is reduced and equals to the ratio of the area occupied by the liquid (the sum of liquid films and wedges) to the total area on the cross-sectional face of the capillary tube. The expression for S_w is written as:

$$S_w(\mu) = \begin{cases} 1 & \mu \geq \mu_d \text{ or } \mu \geq \mu_i \\ \dfrac{3h(\mu)[L - 2\sqrt{3}r(\mu)]X + r(\mu)^2 F_3}{A_3 L^2} & \mu < \mu_d \text{ or } \mu < \mu_i \end{cases} \tag{4.3}$$

where A_3 and F_3 are the pore-shape-dependent parameters, and $A_3 = 2\sqrt{3}$, $F_3 = 3\sqrt{3} - \pi$ for an equivalent triangle [41].

In the R-TPSM, only liquid film is considered to be affected by surface roughness, where liquid film length increases because liquid expends over pits and bumps of the solid surface. Under the saturated condition or for the liquid in corners, the rough surface is substituted by a smooth imaginary boundary.

4.2.1.4 Hydrodynamic consideration for a single pore

Because local flow remains at a relatively slow rate in soil pores, we assumed stable and fully-developed laminar flow in modeled single pores. In the situation of complete pore saturation, liquid flows through capillary channels in the form of duct flow. At partial saturation conditions, flow occurs in thin adsorbed films on solid surfaces and in corners. For film flow and corner flow, we assumed fixed liquid-gas interfaces because breakup or significant deformation of liquid-gas interface requires relatively large viscous forces, which is unlikely under low matric potential conditions [41]. We derived the average flow velocity through duct flow with an equilateral triangular cross section, flow over a planar plate, and corner flow with fixed liquid-gas interfaces, respectively, as follows:

$$\text{Duct flow: } v_d = \frac{L^2}{80\eta_0}(-\frac{dp}{dz}) \tag{4.4}$$

$$\text{Film flow: } v_f = \frac{L^2}{3\eta_0}(-\frac{dp}{dz}) \tag{4.5}$$

$$\text{Corner flow: } v_c = \frac{r(\mu)^2}{\varepsilon\eta_0}(-\frac{dp}{dz}) \tag{4.6}$$

where η_0 is the viscosity of bulk phase (kg m^{-1} s^{-1}); $-dp/dz$ is the pressure head gradient in flow direction z (N m^{-3}); ε is the dimensionless flow resistance parameter [59, 41].

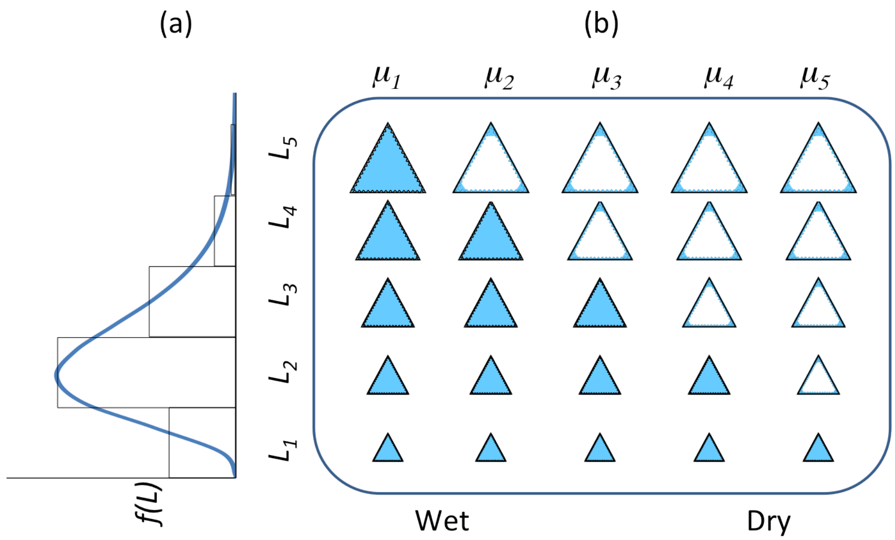

Figure 4.2: Schematic of the applied upscaling scheme in the model: (a) gamma distribution of pore length with 5 hypothetical bins; (b) pore drainage process for a single triangular pore (represented by L_1 to L_5) under the matric potential from μ_1 (wet) to μ_5 (dry).

4.2.2 Pore size distribution

To facilitate the derivation of closed-form functions of core-scale saturation and unsaturated hydraulic conductivity, we applied a gamma distribution function to describe the statistical property of a population of pores. The density gamma function is expressed as:

$$f(L) = \frac{L^{\xi}}{\xi!\omega^{\xi+1}}\exp(-\frac{L}{\omega}) \tag{4.7}$$

The two parameters used in the gamma distribution function are the shape factor ξ and the scale factor ω. The shape factor ξ is limited to integer values. L is the length of the equivalent triangle's sides (m). The mean value of pore length $m(L)$ are calculated as:

$$m(L) = \omega(\xi + 1) \tag{4.8}$$

4.2.3 Upscaling from pore scale to core scale

A conceptual schematic of the applied upscaling scheme is depicted in Fig. 4.2. For illustrative purpose, we used a population of pores with sizes from L_1 to L_5, which satisfy the gamma distribution function. During drainage, pores are gradually drained from large (L_5) to small pores (L_1). At a certain matric potential (e.g., μ_3), larger pores are partially filled (e.g., pores with the size of L_4 or L_5). The shape of a liquid-gas interface in unsaturated pores at each matric potential (μ_1 to μ_5) is determined by Eqs. 4.1 and 4.2. The total core-scale saturation and hydraulic conductivity are calculated as the respective weighted sum at different pore-filling stages as described below.

4.2.3.1 Core-scale saturation

We expressed the core-scale saturation (S_w) as the sum of the three terms that are related to duct flow, film flow and corner flow, respectively. The expressions for core-scale saturation were derived according to the upscaling scheme (Fig. 4.2),

$$\text{Duct flow: } S_{wd}(\mu) = \int_{L_{min}}^{L_1(\mu)} f(L)dL \tag{4.9}$$

$$\text{Film flow: } S_{wf}(\mu) = X \int_{L_1(\mu)}^{L_{max}} \frac{3h(\mu)[L - 2\sqrt{3}r(\mu)]}{A_3 L^2} f(L)dL \tag{4.10}$$

$$\text{Corner flow: } S_{wc}(\mu) = \int_{L_1(\mu)}^{L_{max}} \frac{r(\mu)^2 F_3}{A_3 L^2} f(L)dL \tag{4.11}$$

$$S_w(\mu) = S_{wd}(\mu) + S_{wf}(\mu) + S_{wc}(\mu) \tag{4.12}$$

where C_3 is a pore-shape-dependent parameter [41].

Equation 4.9 describes the portion of saturation contributed by the completely filled pores, which is expressed as the integration between the smallest pore size L_{min} and a certain pore size denoted by $L_1(\mu)$. The equation indicates that the pores with sizes greater than $L_1(\mu)$ remain partially saturated. The value of $L_1(\mu)$ is calculated from the radius of capillary interface curvature at the onset of pore snap-off:

$$L_1(\mu) = -\frac{\sigma}{\rho\mu}C_3 \tag{4.13}$$

Equations 4.10 and 4.11 account for the contribution of film flow and corner flow from the partially filled pores under a certain matric potential μ. The two limits of the integration are defined between $L_1(\mu)$ and L_{max}. The largest pore size L_{max} present in the porous medium can be related to the air entry value μ_d as:

$$L_{max} = L_1(\mu_d) + 2h(\mu_d) \tag{4.14}$$

Equation 4.14 indicates that during the drainage process, the largest pore achieves the onset of pore snap-off at the air entry value μ_d.

4.2.3.2 Core-scale hydraulic conductivity

Flow conductances by ducts, films and corners are derived by incorporating the average flow velocity in a single pore into the Darcy's law. Darcy's law is expressed as:

$$v = \frac{Q}{A} = \frac{K}{\rho g}(-\frac{dp}{dz}) \tag{4.15}$$

where Q is the volumetric flow rate (m^3 s^{-1}), A is the cross sectional area of water phase (m^2), K is the hydraulic conductance (m s^{-1}), and g is the acceleration of gravity (N kg^{-1}). We insert Eqs. 4.4 - 4.6 into Eq. 4.15, so that dp/dz was eliminated, and flow conductances for ducts, films, and corners can be written, respectively, as:

$$\text{Duct flow: } K_D = \frac{\rho g}{\eta_0}\frac{1}{80}L^2 \tag{4.16}$$

$$\text{Film flow: } K_F = \frac{\rho g}{\eta_0}\frac{h(\mu)^2}{3}dL \tag{4.17}$$

$$\text{Corner flow: } K_C = \frac{\rho g}{\eta_0}\frac{r(\mu)^2}{\epsilon} \tag{4.18}$$

Similar to the core-scale saturation, the core-scale hydraulic conductivity (K_w) is determined based on the upscaling scheme (Fig. 4.2) by adding each contribution from duct flow, film flow and corner flow.

$$\text{Duct flow: } K_{wd}(\mu) = \int_{L_{min}}^{L_1(\mu)} \phi K_D f(L) dL \tag{4.19}$$

$$\text{Film flow: } K_{wf}(\mu) = X \int_{L_1(\mu)}^{L_{max}} \phi K_F \frac{3h(\mu)[L - 2\sqrt{3}r(\mu)]}{A_3 L^2} f(L) dL \tag{4.20}$$

$$\text{Corner flow: } K_{wc}(\mu) = \int_{L_1(\mu)}^{L_{max}} \phi K_C \frac{r(\mu)^2 F_3}{A_3 L^2} f(L) dL \tag{4.21}$$

$$K_w(\mu) = \frac{K_{wd}(\mu) + K_{wf}(\mu) + K_{wc}(\mu)}{K_s(\mu)} \tag{4.22}$$

$$K_s(\mu) = \int_{L_{min}}^{L_{max}} \phi K_D f(L) dL \tag{4.23}$$

where ϕ is the porosity of the porous medium.

The term K_s is the saturated hydraulic conductivity, where all pores are completely filled thus only duct flow is considered. The term K_{wd}, K_{wf}, and K_{wc} are defined as the portion from duct flow, film flow and corner flow, respectively. The relative hydraulic conductivity is simply the quotient of K_w and K_s.

4.3 Sensitivity Analysis and Model Application

4.3.1 Sensitivity analysis

To better understand the relationship between the input and output variables in the developed R-TPSM, as well as to test the robustness of model predictions in the presence of uncertainty, we conducted sensitivity analysis before applying the model to measured soil data. The sensitivity of the model to the key parameters (ω, X or μ_d) was explored. For these simulations, values of ξ, ω, X and μ_d were set equal to 2, 10^{-8}, 2, and -1 J kg^{-1}, respectively. These values were selected to reflect the typical model fitting results for sandy and loamy soils. We referred to the modeling results based on these parameter settings as the "measurements". Each time we scaled one of the three key parameters to 0.5, 0.75 1.25, and 1.5 times of the initial setting while kept all other parameters at the preset values. We investigated the behaviors of water retention curve and unsaturated hydraulic conductivity according to each parameter change. It should be noted that the parameter ξ was not treated as a free parameter in the model, so sensitivity analysis was not conducted for ξ. However, the model was calculated with $\xi = 1$, $\xi = 2$ and $\xi = 6$ for each set of the testing data in order to test the flexibility of the proposed model.

4.3.2 Model application

4.3.2.1 Estimation of model parameters from water retention curve

The optimization of the estimated model parameters (i.e., ω, X or μ_d) was achieved by employing the CMA-ES (Covariance Matrix Adaptation Evolution Strategy) [81], which is an evolutionary algorithm for non-linear multi-parameter optimization problems in a continuous domain. The objective function employed is expressed as:

$$S_{w,RMSE} = \sqrt{\frac{\sum_{i=1}^{N}(S_{w,m} - S_{w,c})^2}{N}} \tag{4.24}$$

where $S_{w,m}$ and $S_{w,c}$ are measured and calculated saturation, respectively, and N is the number of the data points. A MATLAB version of the source code was used to conduct the inverse fitting.

4.3.2.2 Calculation of unsaturated hydraulic conductivity

The estimated model parameters from water retention curves were used to calculate the relative hydraulic conductivity using Eqs. 4.19 - 4.23. The goodness of the

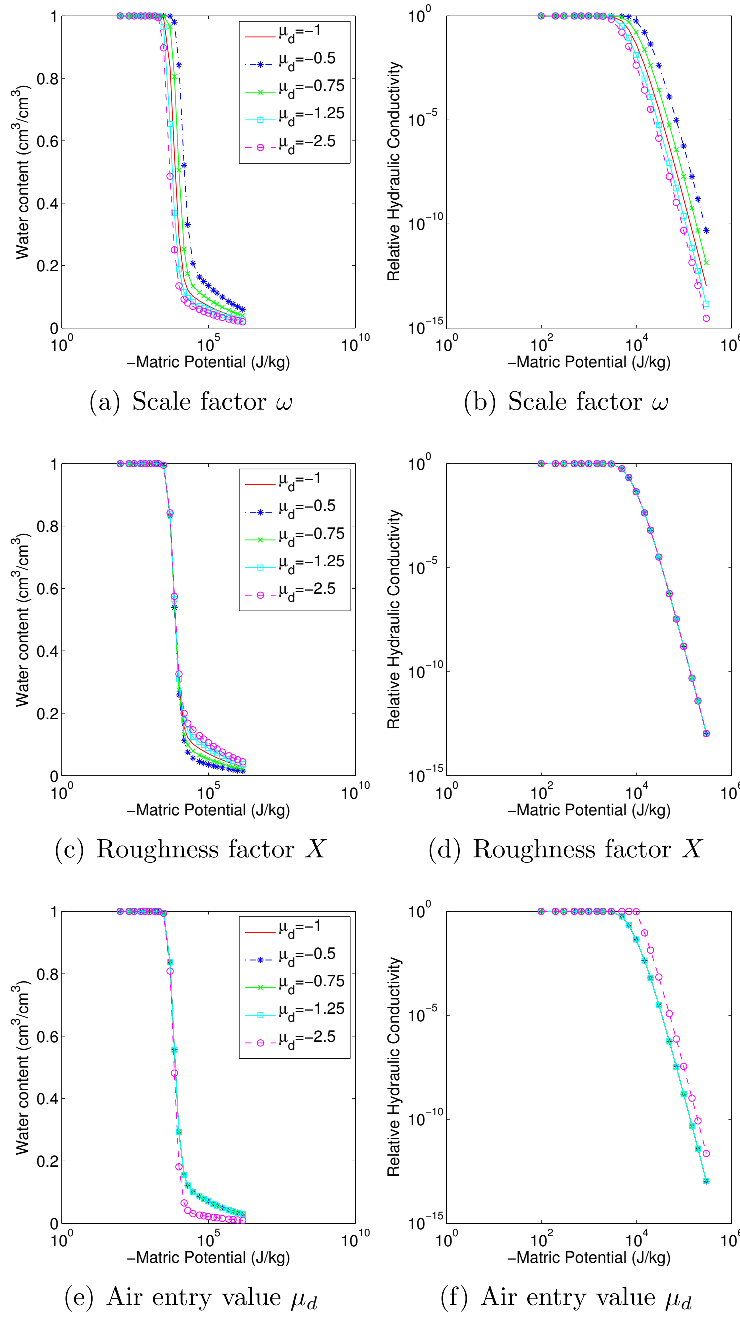

(a) Scale factor ω

(b) Scale factor ω

(c) Roughness factor X

(d) Roughness factor X

(e) Air entry value μ_d

(f) Air entry value μ_d

Figure 4.3: Sensitivity analysis of the R-TPSM for water retention curve and unsaturated hydraulic conductivity: the effects of the scale factor ω (a, b), the roughness factor X (c, d), and the air entry value μ_d (e, f). Other parameters are fixed at $\xi = 2$; $\omega = 10^{-8}$; $X = 2$; $\mu_d = -1$ J kg^{-1}.

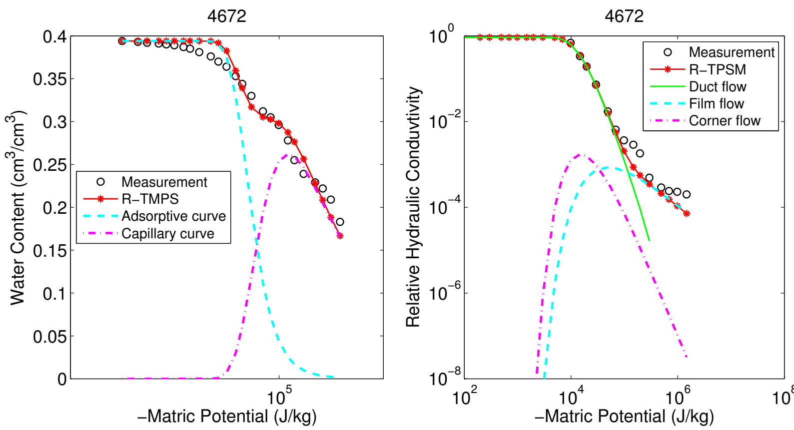

(a) Northen silt loam (θ) (b) Northen silt loam (K)

Figure 4.4: Measured and calculated water retention curves (left) and relative hydraulic conductivity (right) for Northen silt loam

model performance was evaluated by the root mean square error ($RMSE$):

$$K_{RMSE} = \sqrt{\frac{\sum_{i=1}^{N}(K_m - K_c)^2}{N}} \tag{4.25}$$

where K_m and K_c are measured and calculated relative hydraulic conductivity, respectively, and N is the number of data points.

4.3.2.3 Soil properties

The proposed model was tested against 14 sets of experimental data obtained from the Unsaturated Soil Hydraulic Database (UNSODA) [80]. The soil physical properties are summarized in Table 4.1. These soils were chosen because they have fairly complete data sets of both soil water retention curve (drainage process) and hydraulic conductivity. The majority of the soils ranged from coarse sand to silt loam. We only present results from 1 clay soil to show that the model did not fit the data from clay soils well.

Table 4.1: Soil properties

Soil texture	Code	Series Name	θ_S	K_S (cm d^{-1})	Clay(%)	Silt(%)	Sand(%)	OM (mass %)
Sand	1467	Berlin loamy sand	0.270	11.0	0.050	0.072	0.878	-*
	3154	Hecla loamy sand	0.337	6.0	0.045	0.064	0.891	0.39
	4142	Retie sand	0.352	175.0	0.018	0.024	0.958	0.18
	4661	Bordenan sand	0.428	1140.5	0.040	0.040	0.920	0.50
	4130	Poppel loamy sand	0.389	60.1	0.054	0.128	0.818	2.67
	4021	Poederlee sand	0.420	164.0	0.025	0.101	0.874	0.54
Loam	3392	Rosdorf loess silt loam	0.380	0.32	0.236	0.722	0.042	0.35
	3380	Rosdorf loess silt loam	0.390	2.19	0.123	0.822	0.055	0.91
	4672	Northen silt loam	0.394	2.42	0.180	0.760	0.060	0.17
	4673	Northen silt loam	0.415	4.33	0.140	0.810	0.050	0.17
	2321	Hasenholz loam	0.372	5.0	0.200	0.430	0.370	3.10
	4101	Boz polder loam	0.395	9.3	0.163	0.421	0.416	0.77
	2611	Schmidwald loam	0.507	39.8	0.245	0.480	0.275	4.00
Clay	2360	Seelow clay	0.492	5.0	0.450	0.380	0.170	4.86

Source: Data from UNSODA [80].
* No data reported.

4.4 Results

4.4.1 Sensitivity analysis

Fig. 4.3 present the results of sensitivity analysis of the three free model parameters for water retention curve and unsaturated hydraulic conductivity, respectively. The scale factor ω had a pronounced effect on both water retention curve and unsaturated hydraulic conductivity over the entire range of drainage process (Fig. 4.3a and 4.3b). The roughness factor X significantly influenced water retention curve at low water saturation as shown in Fig. 4.3c, however, it had little impact on the predicted hydraulic conductivity (Fig. 4.3d). The air entry value denoted by μ_d had negligible impact on water retention curve and hydraulic conductivity when μ_d was between -1.25 J kg and -0.5 J kg, whereas relatively large derivation was observed with μ_d=-2.5 J kg^{-1} (Figs. 4.3e and 4.3f). The parameter μ_d was moderately sensitive only when it exceeds a certain critical value (e.g., μ_d=-2.5 J kg^{-1} for the test case with the preset parameters).

4.4.2 Modeling water retention curve and unsaturated hydraulic conductivity

4.4.2.1 Primary features of the R-TPSM

The developed R-TPSM was employed to predict the unsaturated hydraulic conductivity from measured soil retention curves of the testing soils. The primary features of the model are demonstrated for the Northen silt loam. A set of model parameters ($\omega = 4.21 \times 10^{-8}$, $X = 16.63$ and μ_d=-0.02 J kg^{-1}) was estimated by fitting the model to the measured water retention curve. Individual contributions of adsorptive and capillary forces to water retention in soil pores are shown in Fig. 4.4a. Capillary force dominated at low suctions (less negative matric potential), and as the suction increased to where the capillary curve and the adsorptive curve crossed each other, adsorptive force became dominant over capillary force in retaining water. For the Northern silt loam depicted in Fig. 4.4a, the crossover point was found at $\sim -10^5$ J kg^{-1}.

The unsaturated hydraulic conductivity was readily predicted using the same set of model parameters estimated from the water retention curve. For the demonstrating example, individual contributions of duct flow, film flow and corner flow are depicted separately in Fig. 4.4b. Duct flow absolutely dominated at low suctions, but its contribution to hydraulic conductivity with increasing suction. At the point where film flow started to become dominant, a smaller slope of the $\log K_r - \log\mu$ curve than that at the duct-flow-dominant region was observed.

4.4.2.2 Comparison with the VGM

We compared the R-TPSM with the VGM for the testing soils (6 sandy soils in Fig. 4.5, 6 loamy soils in Fig. 4.6, 1 clay soil in Fig. 4.7). Model parameters for both models were estimated from the same measured soil retention curves, and were used to calculate unsaturated hydraulic conductivity. The goodness of model fitting results for the 14 testing soils are presented in Table 4.2. We also tested the R-TPSM with different ξ values: $\xi = 1$, $\xi = 2$ and $\xi = 6$. The calculated root mean square errors show that the best fit for sandy soils was mostly obtained with $\xi = 6$, and for loamy soils the root mean square error reached its smallest value with $\xi = 1$.

For sandy soils, both the VGM and R-TPSM achieved excellent fits to the measured retention data, as shown by the calculated values of $RMSE$ listed in Table 4.2. Out of the 6 sandy soils, the R-TPSM better fitted the measured hydraulic conductivity values for 4 soils than the VGM. Particularly, the smaller slope of $\log h$ - $\log K$ curve at low water contents was well characterized by film conductivity in the R-TPSM.

The R-TPSM and VGM were in reasonable agreement with the measured retention data for loamy soils. Predictions for unsaturated hydraulic conductivity of loamy soils show that the VGM routinely underestimated hydraulic conductivity, while the R-TPSM was able to match the measurements reasonably well. The R-TPSM agreed well with the experimental data of Rosdorf loess silt loam (3392) and Northen silt loam (4672) over the entire range of matric potentials, but overestimated the relative

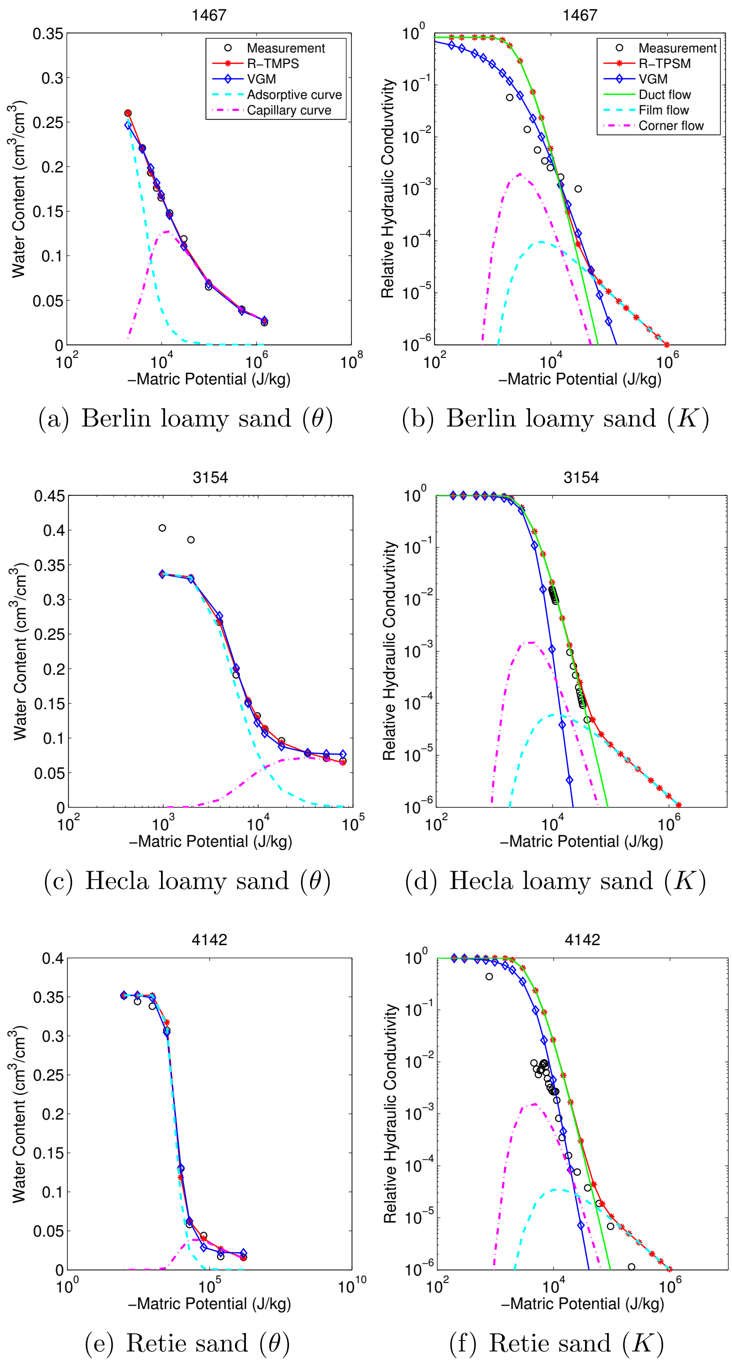

(a) Berlin loamy sand (θ) (b) Berlin loamy sand (K)

(c) Hecla loamy sand (θ) (d) Hecla loamy sand (K)

(e) Retie sand (θ) (f) Retie sand (K)

Figure 4.5: Measured and calculated water retention curves (left) and relative hydraulic conductivity (right) for six sandy soils

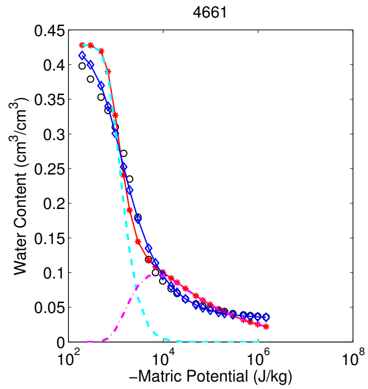

(g) Bordenan sand (θ)

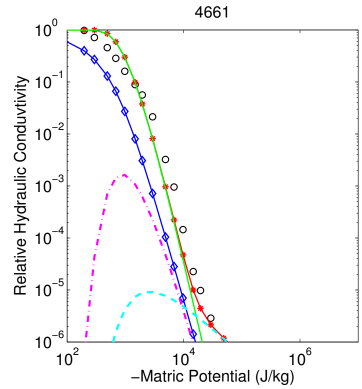

(h) Bordenan sand (K)

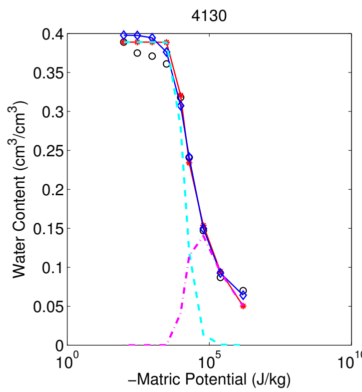

(i) Poppel loamy sand (θ)

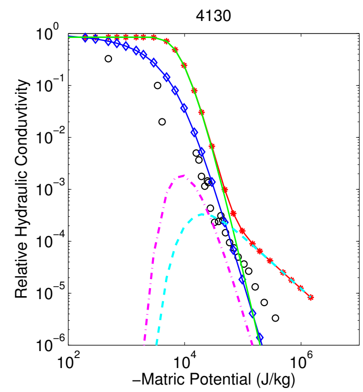

(j) Poppel loamy sand(K)

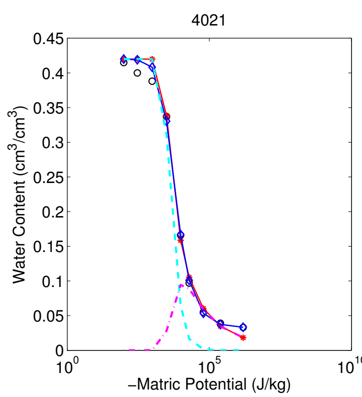

(k) Poederlee sand (θ)

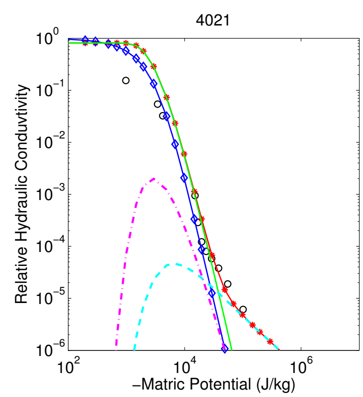

(l) Poederlee sand (K)

Figure 4.5: Measured and calculated water retention curves (left) and relative hydraulic conductivity (right) for six sandy soils (Con't)

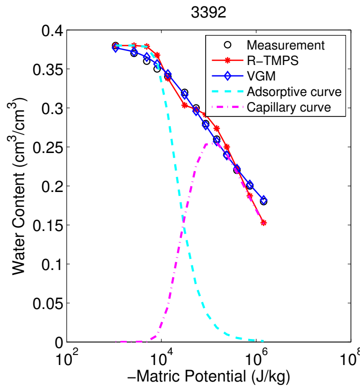

(a) Rosdorf loess silt loam (θ)

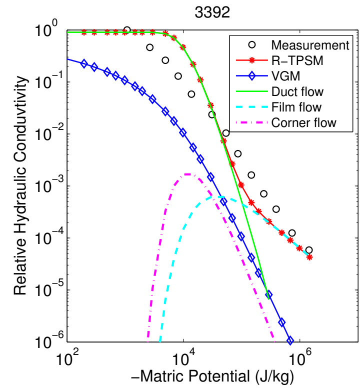

(b) Rosdorf loess silt loam (K)

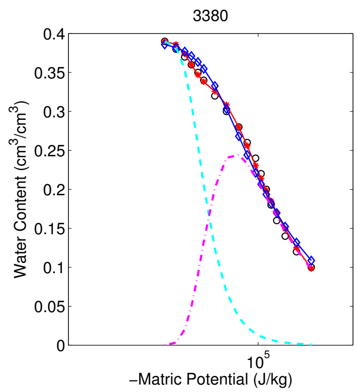

(c) Rosdorf loess silt loam (θ)

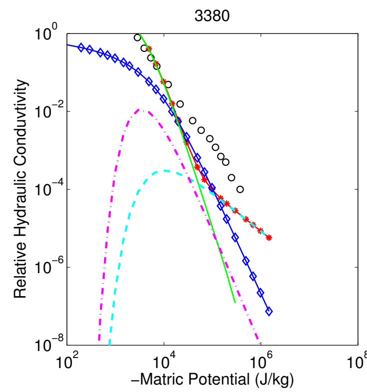

(d) Rosdorf loess silt loam (K)

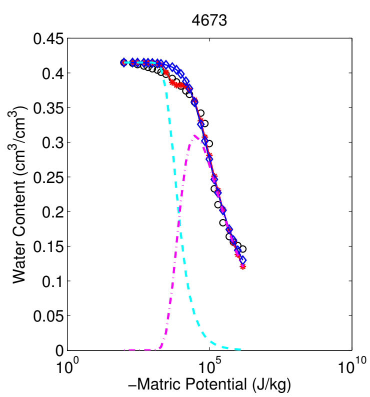

(e) Northen silt loam (θ)

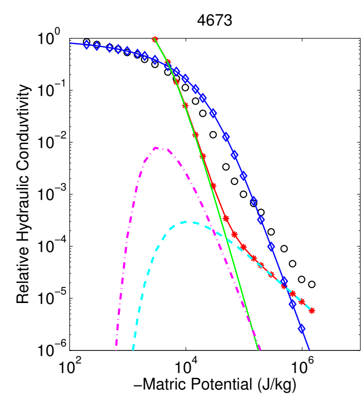

(f) Northen silt loam (K)

Figure 4.6: Measured and calculated water retention curves (left) and relative hydraulic conductivity (right) for six loamy soils

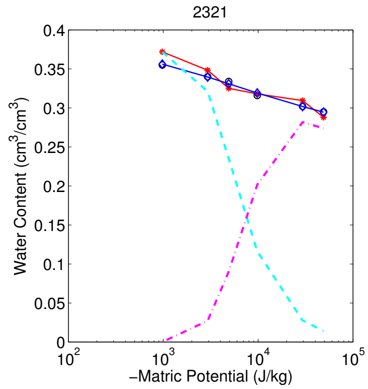

(g) Hasenholz loam (θ)

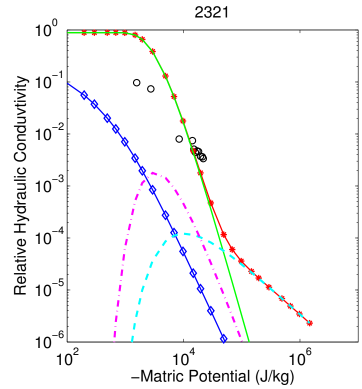

(h) Hasenholz loam (K)

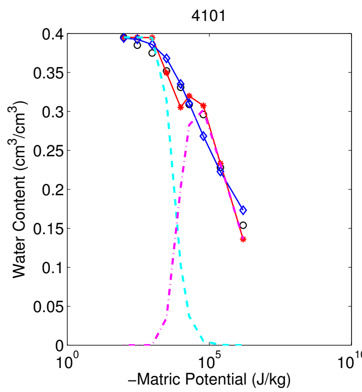

(i) Boz polder loam (θ)

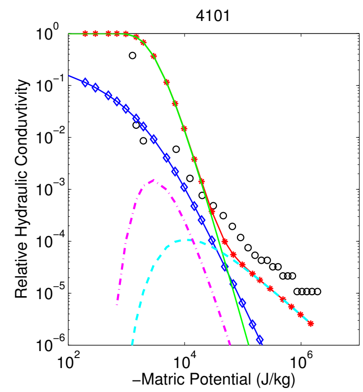

(j) Boz polder loam (K)

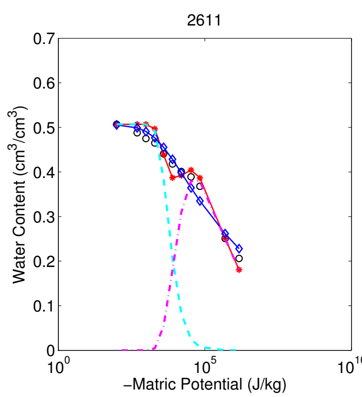

(k) Schmidwald loam (θ)

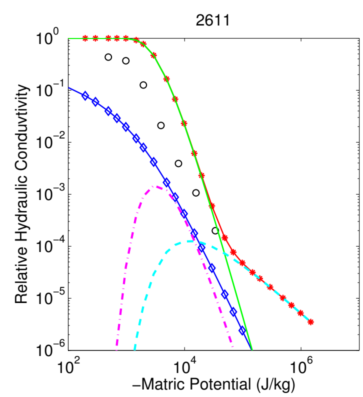

(l) Schmidwald loam (K)

Figure 4.6: Measured and calculated water retention curves (left) and relative hydraulic conductivity (right) for six loamy soils (Con't)

Table 4.2: Calculated root mean square errors ($RMSE$) for water retention curve and hydraulic conductivity using the R-TPSM and VGM (The italic numbers show the smallest values of $RMSE$. The comparison was conducted between different values of ξ for water retention curves and between the R-TPSM and VGM for hydraulic conductivity)

Soil texture	Soil code	R-TPSM (Retention)			VGM (Retention)	R-TPSM (K_r)	VGM (K_r)
		$\xi = 1$	$\xi = 2$	$\xi = 6$			
Sand	1467	0.0199	0.0158	*0.0029*	0.0059	0.6911	*0.3796*
	3154	0.0275	*0.0258*	0.0262	0.0272	*0.0858*	1.2426
	4142	0.0259	0.0084	*0.0075*	0.0163	*0.4487*	0.5550
	4661	0.0649	*0.0266*	0.0332	0.0098	*0.1949*	1.2470
	4130	-*	0.0143	*0.0131*	0.0262	0.4616	*0.2579*
	4021	-*	0.0209	*0.0142*	0.0098	*0.2532*	0.9354
Loam	3392	*0.0135*	0.0167	0.0188	0.0033	*0.9371*	3.5320
	3380	*0.0056*	0.0065	0.0106	0.0110	*1.3419*	1.6004
	4672	*0.0118*	0.0136	0.0175	0.0044	*0.4913*	3.3249
	4673	*0.0116*	0.0163	0.0137	0.0131	1.5556	*1.0350*
	2321	*0.0095*	0.0111	0.0154	0.0019	*1.0627*	5.4083
	4101	*0.0140*	0.0178	0.0216	0.0134	*1.6435*	4.2469
	2611	*0.0267*	0.0267	0.0362	0.0169	*1.7063*	2.3021

* Unreasonable parameters were obtained with the R-TPSM.

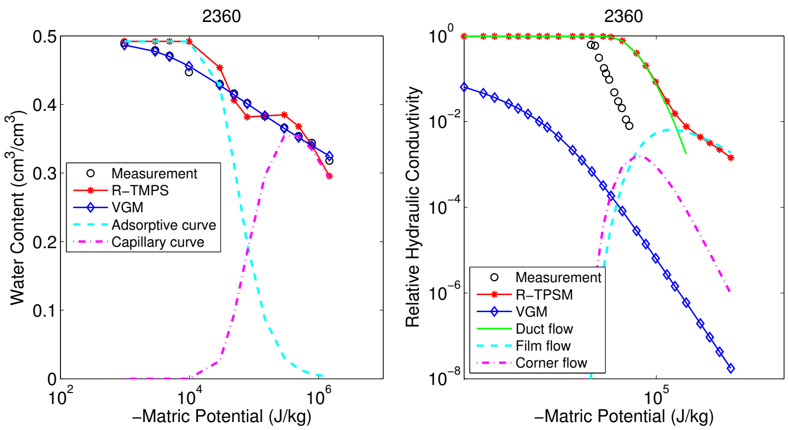

(a) Seelow clay (θ) (b) Seelow clay (K)

Figure 4.7: Measured and calculated water retention curves (left) and relative hydraulic conductivity (right) for Seelow clay

hydraulic conductivity of Hasenholz loam (2321), Boz polder loam (4101) and Schmidwald loam (2611) at high water saturation using the R-TPSM.

For the clay soil, the VGM fitted the water retention measurements well, while derivation was observed with the R-TPSM (Fig. 4.7). Both models were unable to fit the experimental hydraulic conductivity data.

4.5 Discussion

4.5.1 Significance of film flow

In the R-TPSM, the capillary force, which controls duct flow and corner flow, dominates at high water contents (low suctions or less negative matric potentials) whereas the adsorptive force mainly accounts for retaining water films at low water contents. As shown by the above demonstrating examples, considering adsorptive force and film flow in the R-TPSM is the main reason for the improvement of water retention curve and hydraulic conductivity modeling. The importance of film flow has also been recognized in other hydraulic conductivity models. [84] proposed a hydraulic conductivity model considering both capillary flow and thin film flow based on cylindrical pore space. In [90], the adsorptive saturation was incorporated in the water retention model by [95], so that hydraulic conductivity were coupled with appropriate retention models. Results from these models emphasized that film flow prevailed over capillary flow at the dry ends, which agrees well with the conclusion from this study.

Comparison with the VGM emphasizes that neglecting film retention and film conductivity can lead to considerable errors for hydraulic conductivity modeling. In addition, the VGM fitted the retention data of sandy soils only when the residual water content was set to a nonzero value, which indicates that flow is negligible at water contents smaller than the residual value [42]. However, the residual water content is not a consistently physically recognized concept, because water flow has been observed under the condition near the residual water content [45].

4.5.2 Surface roughness effects

Another key factor for the success of hydraulic conductivity modeling is accurate description of pore-scale flow phenomenon. Pore-scale flow behavior can be largely affected by surface roughness. [96] reported that the average roughness for a quartz sand grain was around 300 nm, with the maximum roughness larger than 2 μm. One of the roughness effects is that water films expend over pits and bumps of the solid surface so that the surface area of water film is largely increased. The roughness factor X defined in the proposed R-TPSM significantly influences the water retention curve at low water contents as shown by the sensitivity analysis (Fig. 4.3b). It also implicitly affects the pore size distribution when estimating the model parameters from the water retention curve, and consequently, indirectly affects hydraulic conductivity.

Surface roughness on soil particles can be affected by various factors, e.g., mineralization, organic matter (OM) coating on solid particles, biological factors and so on. Previous research reported that aggregates of soil organic matter increased soil particle's surface roughness at microscale [97]. In this study, smaller roughness factors were observed for sandy soils than that for loamy soils, as the average roughness factor was 7.87 for sandy soils, while it was 15.80 for loamy soils, which indicates that roughness factor could also be related to soil texture. This result is consistence with the original TPSM, which showed that fine-textured soils contained more internal surface area as compared with coarse-textured soils [41]. Thus, the proposed roughness factor also accounts for the internal surface area which leads to additional adsorptive water films.

Due to the highly heterogenous surface properties, direct measurement of soil surface roughness is not available. In order to estimate the roughness factor X from more easily measured soil properties, we developed a pedotransfer function by correlating the estimated roughness factor to soil composition: percentages of sand, slit and clay, and OM content, which are generally available in the UNSODA soil database. Pedotransfer functions are statistic regression equations that correlate hydraulic conductivity properties of soils with other physical properties. These functions have been proven to be good predictors for soil hydraulic conductivity data [98, 99, 100].

We derived a regression function between the percentage of each soil textural composition (e.g., sand, silt, clay), soil OM content and the roughness factor estimated from the proposed R-TPSM using a linear least square procedure. The resulted regression function is written as:

$$X = 2.78 \times \text{OM\%} + 12.29 \times \text{sand\%} + 4.08 \times \text{silt\%} + 0.00 \times \text{clay\%} \tag{4.26}$$

The predicted roughness factors based on Eq. 4.26 are plotted against the estimated ones from measured water retention curves using the R-TPSM model (Fig. 4.8). Results indicate that the regression function could predict the roughness factor reasonably well. The magnitude of regression coefficients offers insight of which parameters are more relevant for predicting the roughness factor. Eq. 4.26 indicates that the roughness factor is affected by the OM content. This result is supported by a previous microscopic observation where an image and force measurement of acid washed quartz sand showed that after immersing the particle in humic acid or lecithin solution, the hight of surface roughness increased significantly [101].

While the contents of sand and silt can significantly affect the roughness factor,

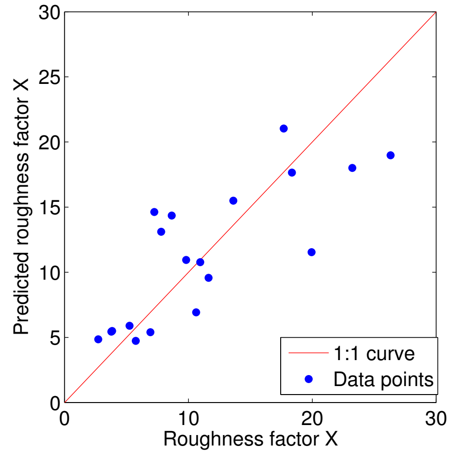

Figure 4.8: Plot of the roughness factor estimated from water retention curves versus the prediction using Eq. 4.26

the regression coefficient for the clay content is 0, indicating that clay content is not relevant to the roughness factor. This may be due to the scale on which surface roughness is examined. The pits and bumps at solid surface have to be large enough so that film flow could recognize a surface as rough, otherwise, the roughness features increase the film thickness rather than the film length. Clay particles are classified as the particles with a diameter less than 2 μm. At a matric head of -1 or -10 cm (below which unsaturated state is usually encountered), film thickness is calculated as $\sim 3{-}1.5$ nm by Eq. 4.1. Consequently, the pore space between clay particles may not be enough for valid pits or bumps for increasing film area, and thus clay content is not relevant to the roughness factor. In addition, we found that the proposed R-TPSM can rarely give a reasonable prediction for clay soils (Fig. 4.7). The Seelow clay contains 45% of clay particles, which is significantly more than other testing soils. Clay particles are planar rather than spherical, thus the pore geometry defined in R-TPSM is not representative of the real pore space [102] in clay soils, which may be the reason for the unsatisfied prediction results.

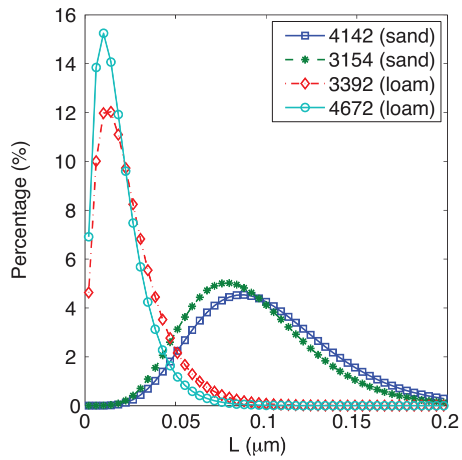

Figure 4.9: Pore size distribution plotted based on the fitted ω from water retention curves for two sandy soils ($\xi = 6$) and two loamy soils ($\xi = 1$)

4.5.3 Soil pore size distribution

The proposed R-TPSM applied a gamma distribution function to describe the statistical distribution of pore sizes. The gamma function contains two parameters, the shape factor ξ and the scale factor ω. We showed that the best fit for sandy soils was mostly obtained with $\xi = 6$, and for loamy soils the root mean square error reached its smallest value with $\xi = 1$. The value of ξ was fixed at 2 in the original TPSM [41] in order to derive closed-form expressions for core-scale unsaturated hydraulic conductivity, which could lead to a reduced flexibility of the model. Our results indicate that the value of ξ depends on soil texture. Fixing the ξ value without consideration of soil texture can lead to unreasonable pore size representation.

The scale factor ω was estimated from the measured soil retention curves. The ω value for each soil was obtained with the best fitted ξ ($\xi = 6$ for sandy soils and $\xi = 1$ for loamy soils). The pore size distribution curves for two sandy and two loamy soils (Fig. 4.9) are plotted using the corresponding gamma function, which show that the largest probability existed at the pore lengths of 20 nm to 30 nm for the two loamy soils (3392 and 4672), and two sandy soils had the pores mostly with the sizes around 80 nm and 100 nm (3154 and 4142). The magnitude of pore sizes estimated from water retention curves were comparable to the reported directly measured soil pore size data [103]. The relatively larger pore size of sandy soils can be related to larger particles sizes, as the pore size distribution is related to particle size distribution [104]. A relatively narrow size distribution was also found for sandy soils compared with loamy soils.

In addition, the sensitivity analysis indicates that the scale factor ω is extremely sensitive to both water retention curve and unsaturated hydraulic conductivity. By changing the value of ω from 0.5 to 1.5 times of the preset value, the saturation at the separating point for capillary-dominant region and adsorption-dominant region in the retention curve decreased from 0.2 to 0.1 cm^3 cm^{-3} (Fig. 4.3a). A greater separating point value represents a wider adsorption-dominant region. According to Eq. 4.8, a smaller ω value corresponds to a smaller mean pore size at a constant ξ value. Therefore, at the same matric potential, a medium with smaller mean pores (smaller ω) is able to retain more liquid and remains at a higher saturation level.

4.6 Conclusions

In this study, a R-TPSM for water retention curve and hydraulic conductivity was developed considering surface roughness effects. The model is physically based as all the parameters have clear physical meanings and are sensitive to model output. The pore geometric parameters are estimated by fitting the model to measured water retention curve, then unsaturated hydraulic conductivity is predicted without additional parameters. Compared with the original TPSM [41], the R-TPSM has less adjustable parameters, which reduces the uncertainties associated with inverse estimation of model parameters using water retention curves.

The developed R-TPSM is able to effectively predict unsaturated hydraulic conductivity of soils with various textures with a known water retention curve and saturated hydraulic conductivity. Consideration of adsorptive water films in the R-TPSM allows for a smaller slope of the $\log K_r - \log\mu$ curve at lower water contents, which is a typical pattern in most measured $\log K_r - \log \mu$ curves. Therefore, prediction of hydraulic conductivity is significantly improved compared with the VGM, especially for loamy soils. The R-TPSM does not fit well water retention data of clay soils, because clay particles are planar rather than spherical, thus the triangular tubes defined in R-TPSM are not representative of the real pore space in clay soils. Furthermore, the R-TPSM does not include swelling mechanisms, which could also have a considerable impact on flow in clay soils.

In the R-TPSM, one of the most important model parameters is the roughness factor. Regression analysis indicates that roughness factor is not likely relevant to clay content, but is strongly related to OM content, and contents of slit and sand. The regression function potentially enables the application of the developed model to REV-scale-based simulations at the field and even larger scales, as soil properties, such as soil texture and OM content are readily available in soil survey database. Another important variable e.g., the pore size distribution function, estimated using the R-TPSM, is comparable to direct pore size measurements.

One limitation of the model is that effects of surface roughness are reflected only in film flow, which is likely incomplete. Film thickness, contact angle, and flow conductivity could also be influenced by surface roughness. Further improvement may be achieved by considering additional mechanisms and effects due to surface roughness and/or by employing more realistic pore space representations, e.g., the pore network model.

Chapter 5

SLIP FLOW BOUNDARY CONDITION AT ROUGH SURFACES

5.1 Introduction

Since virtually nearly all natural and engineering surfaces are rough at a certain scale, accounting for effect of surface topography is critical for accurately modeling flow in porous media. Effective models for flow in porous media can lead to an improved understanding of subsurface geobiochemical transformations, because fluid flow can carry dissolved minerals and anthropogenic contaminants through a great distance in subsurface, and fluid flow also mediates transport of anthropogenic and inorganic colloidal particles. Classical hydrodynamic model, which is based on the application of no-slip boundary condition at fluid-solid surface to Navier-Stokes equation, has been well established in the field of fluid mechanics and widely used in pore-scale modeling of flow in porous media [97, 25]. However, the no-slip boundary condition, which describes that the layer of liquid next to a solid surface moves with the same velocity as the surface, is generally accepted as no more than a convenient approximation that holds under macroscopic flow conditions [37, 38]. A slip boundary condition is regarded as a more appropriate alternative for rough surfaces.

Roughness effects on the slip boundary condition at solid surface have been investigated at different scales(e.g., molecular scale, pore-scale). Molecular-scale roughness depends strongly on surface hydrophobicity, which is determined by the nature of intermolecular interactions [105, 38]. The magnitude of the corresponding slip length remains only a few tens of nanometres at most [52]. Therefore, the no-slip boundary condition at local surfaces is still a reliable approximation [39, 32]. A different picture is obtained when considering surfaces with natural or engineered structures at the microscale or the scale equivalent to the pore size. It may be impossible or meaningless to represent all the details at the walls of the pore. To describe such situation, an effective slip length of the equivalent boundary is usually calculated [51, 63, 53]. Particularly when surfaces are hydrophobic where fluid may not fully saturate the solid surfaces, a mixed boundaries of liquid-gas and liquid-solid interfaces exist in the flow system and can have a profound effect on the overall flow behavior [50, 51].

The mixed boundary flow problem was first studied by Philip [50] with the initial motivation to understand the hydrodynamic property of flow in unsaturated porous media. Such flow takes place in highly interconnected and tortuous regions bounded by solid-water and air-water interfaces. More recently, the mixed boundary problem has been extensively investigated in the field of superhydrophobic surfaces [106, 107]. Superhydrophobic surfaces are defined as surface with a combination of hydrophobicity and micro- or nano-scale surface roughness. These surfaces were designed mimicking the topography of the biologically inspired surfaces, such as lotus leaf, as an effort to drag and friction reduction in devices operating at the micro- and nano-scale [108, 109]. Slip lengths up to a few micrometers has been measured on fabricated patterned surfaces [110, 111, 112]. The hydrophobicity of the surface prevents liquid from occupying the cavities in between the micro- or nano- asperities, thus resulting in the formation of gas-pockets in the cavities. There seems to be unanimous agreement that the enhanced effective slip is attributed to the existence of gas cavities, where liquid-gas interfaces are presented [107, 31, 113].

Theoretically, the slip boundary condition at rough surfaces where mixed boundary applies have been investigated with a focus of its dependence on roughness length scales, interfacial curvature and interfacial shear at liquid-gas interfaces. Philip [50] derived analytical solution for the effective slip length on patterned with alternating no-slip and shear-free domains using the method of separation of variables. Lauga and Stone [51] and Cottin-Bizonne et al. [52] semi-analytically solved the effective slip length for pressure-driven Stokes flow in circular pipe with the surface patterned with longitudinal and transverse stripes of alternating no-slip and no shear regions. Ybert et al. ([53]) performed a scaling law analysis in various geometries (grooves, posts or holes). These solutions predict that the effective slip length is a function of both the gas fraction and the period of roughness features.

While superhydrophobic surface is designed to reduce flow resistance, recent studies reported that an increase in flow resistance was encountered with the use of superhydrophobic surface by experiments and numerical computations [114, 64, 115]. Steinberger et al. [64] observed a reduced effective slip length on a hydrophobic surface compared with a hydrophobic surface, both of which were patterned with a square lattice of circular holes. Using the micro-particle image velocimetry (μ-PIV), Tsai et al. [63] investigated the microflow in hydrophobic micro-structured channels, which showed that the slip length was smaller than that estimated by Philip [50]. The experimental results suggested that the curvature of the meniscus played an important role in controlling the flow characteristics with mixed boundaries. This conclusion agrees well with the observed protrusion of the liquid-gas interfaces [63, 112, 116].

Another explanation for the reported decreased effective slip length was attributed to the confinement of the channel wall, leading to trapped liquid-gas interfaces [106], where fluid must accelerate from rest at the solid surfaces. In other words, the liquid-gas interface may not be shear-free at the microscale. Zheng et al. [79] conducted open microchannels experiments and concluded that the partial-slip, rather than the commonly used stress-free condition, provided a more accurate description of the boundary condition at the confined air-water interface. Results from the liquid-gas coupled model, which accounts for the interaction between liquid and gas phase, indicated that very small gas/liquid viscosity ratio may have considerable effects on the effective slip length [114, 117, 118].

While considerable studies on mixed boundary problem have focus on the effects of perturbation into liquid-gas interfaces, the liquid-gas interfacial shear effect or the coupled effects from interfacial shape and interfacial shear on the effective slip length was not clear. The main objective of this study is to understand the slip boundary condition at stripe-structured surfaces with mixed no-slip and partial-slip boundary conditions. The effective slip length was numerically investigated by solving

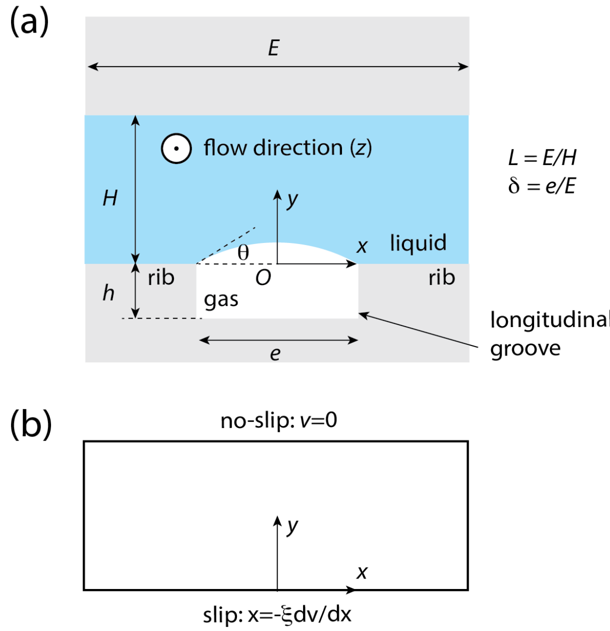

Figure 5.1: (a) Schematic flow configurations. Note that $\theta > 0$ represents convex interfaces and $\theta < 0$ for concave interfaces). (b) Flow boundary conditions for an analytical solution.

pressure-driven flow in microchannels with rough surfaces. I also changed other system parameters, such as roughness period to channel height ratio (L), gas fraction (δ), and liquid-gas curvature (θ).

5.2 Theoretical Considerations

5.2.1 Problem setup

I depicted the flow configuration analyzed in this study in figure 5.1a. The flow was assumed to be fully developed, and only in the streamwise z-direction. The structured surfaces, which consist of periodic grooves and ribs, were only patterned on the bottom wall of the microchannel. Grooves and ribs were designed parallel to the streamwise z-direction. The height of the microchannel was H. The length of the microchannel was assumed to be infinite, thus flow across one groove and rib was not subjected to the wall effect in the y-direction and could be treated as periodic flow. One repetition of equal cell consisting of the groove-rib combination is shown in figure

5.1a. Each groove and rib spans a distance of e and $(E - e)$, respectively, in the x-direction. Two dimensionless geometric parameters were used to characterize the shape of microchannel: (1) the liquid-gas fraction $\delta = e/E$, and (2) the dimensionless periodic extent of each groove-rib combination normalized by the channel height $L = E/H$.

The laminar flow in the microchannel was dominated by the viscous forces and the inertial effects were negligible, therefore, the Stokes equation was employed to calculate the velocity field in the flow domain:

$$\mu\nabla^2 v = -\frac{dp}{dz} \tag{5.1}$$

where μ is the liquid viscosity (kg m^{-1} s^{-1}), and $\frac{dp}{dz}$ is the pressure gradient (kg m^{-2} s^{-2}) along the z-direction.

I normalized the variables by the characteristic length H, $X = x/H$, $Y = y/H$, and $u = -v\frac{1}{\mu H^2}\frac{dp}{dz}$, so the governing equation can be written accordingly:

$$\nabla^2 u = 1 \tag{5.2}$$

No-slip boundary condition was applied at the liquid-solid surface (i.e., the top wall and ribs):

$$u(x, 1) = 0; \tag{5.3}$$

$$u(x, 0) = 0 \text{ on } \delta L/2 < |x| < L/2; \tag{5.4}$$

The periodic boundary condition in the y-direction was:

$$\frac{u(\pm L/2, y)}{dx} = 0; \tag{5.5}$$

The liquid-gas interface was assumed to be pinned at the sharp corner of the ribs. The interface deformed under a constant pressure difference between the gas and the liquid phase. The protrusion angle θ was positive when the meniscus bows toward the liquid phase (i.e., convex), and negative when the interface bows away from the liquid phase (i.e., concave). A boundary condition considering the local slip length ξ_g was used to describe the liquid-gas interface:

$$u = -\xi_g \frac{du}{dn} \text{ on a curved liquid-gas interface;} \tag{5.6}$$

where n is the tangential direction of the curved interface. The locally normalized slip length ξ_g was assumed to be proportional to the width of the groove (e) ([79]).

5.2.2 Effective slip length

The effective slip length ξ over the patterned surface was defined by equating the actual flow rate with the flow rate that would be found in a rectangular channel of height H and width L with a partial-slip condition applied at the patterned surface (figure 5.1b) [119]. The normalized effective length was defined as $\xi/\delta e$, which was calculated and compared with analytical solutions in the literature. The expression for $\xi/\delta e$ was written as [116, 119]:

$$\frac{\xi}{\delta e} = (\frac{1}{\delta^2 L})(4q - \frac{1}{3}) \tag{5.7}$$

where q is the normalized volumetric flow rate per unit width, and can be determined from [119]:

$$q = \frac{1}{L}\int_A v(x,y)dA \tag{5.8}$$

5.2.3 Numerical calculation

Computations for the velocity field at the flow domain (figure 5.1a) using the finite element method were achieved by employing the Partial Differential Equation (PDE) Toolbox in Matlab (The Mathworks, Natick, MA). The flow domain was discretized using triangular elements. The mesh was refined until doubling the number

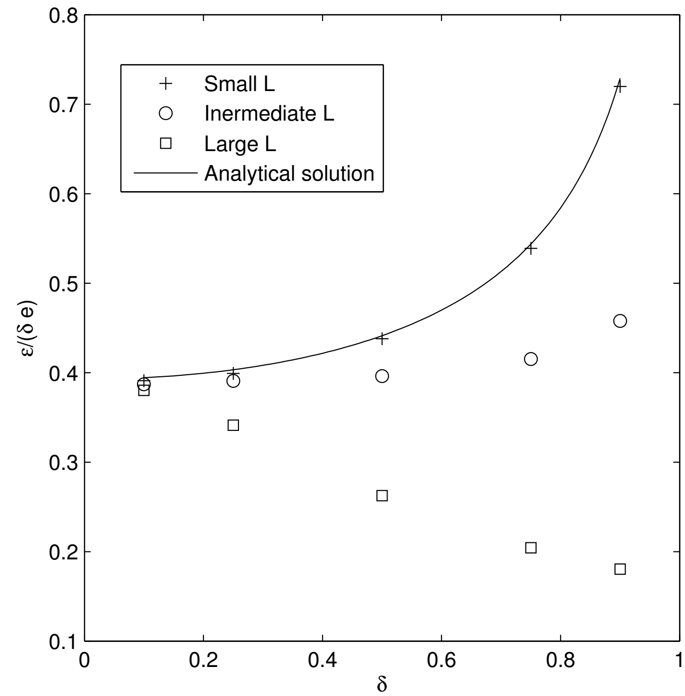

Figure 5.2: Numerically simulated $\xi/\delta e$ versus the approximated $\xi/\delta e$ by equation 5.9 A flat and shear-free liquid-gas interface was assumed in the calculations.

of element resulted in a difference of δe not more than 0.5% for the velocity, which is considered to be adequate [120].

5.3 Results and Discussion

5.3.1 Influence of gas fraction

I first validated the accuracy of the numerical results obtained using the finite element solver using an analytical solution. Philip ([50]) has previously reported an analytical solution of the effective slip length for longitudinal grooves with small value of roughness period to channel height ratio assuming the liquid-gas interface is flat (θ = 0) and shear-free:

$$\frac{\xi}{\delta e} = \frac{1}{\pi\delta^2}\ln[\sec(\frac{\delta\pi}{2})] \tag{5.9}$$

According to equation 5.9, the effective slip length is soly determined by the gas fraction. I calculated effective slip lengths at various gas fractions (δ=0.1, 0.25, 0.5, 0.75, and 0.9), and perfect agreement between the numerical results and Philip's solution was observed under the condition when the value of L was small ($L = 0.2$, figure 5.2), ensuring the accuracy of the numerical solver for solving mixed boundary flow problems.

The numerical results for intermediate roughness period to channel height ratio ($L = 1$) and large L (=5) for flat ($\theta = 0$) and shear-free liquid-gas interface is also plotted in figure 5.2. As clearly shown in the figure, there was a significant difference between the curves of the normalized effective slip length as a function of no-shear fraction under the conditions with different values of L. As the gas fraction increased, the normalized effective slip length increased for small L, while it decreased for large L. Results in Teo et al. [120] showed the same trend of the dependence of normalized effective slip length on the gas fraction. The greater value of L indicated a smaller spacing H for a fixed groove-rib period E. With a small spacing H, flow on the superhydrophobic surface on the bottom wall was affected by the distance away from the top wall. The result highlights the confinement effect from the top wall on the effective slip length on the rough surfaces [120].

5.3.2 Influence of liquid-gas interfacial shear

In this section, the liquid-gas interface was considered as flat but assumed to be a shear boundary with the local slip length at liquid-gas interface ξ_g. According to Ybert et al.[53], for $\xi_g \to 0$, the normalized effective length was expressed as $\xi/\delta e = \delta \xi_g$, and for $\xi_g \to \infty$, $\xi/\delta e = \xi_{ideal}$, where ξ_{ideal} is the effective slip length obtained in the idealized case where a no-shear boundary condition is assumed at the liquid-gas interface. An interpolation equation was thus proposed to formulate the dependence of effective slip length on the local slip length at liquid-gas interface ξ_g and geometric parameters. For ξ_g between the two limits 0 and ∞, the interpolation formula was

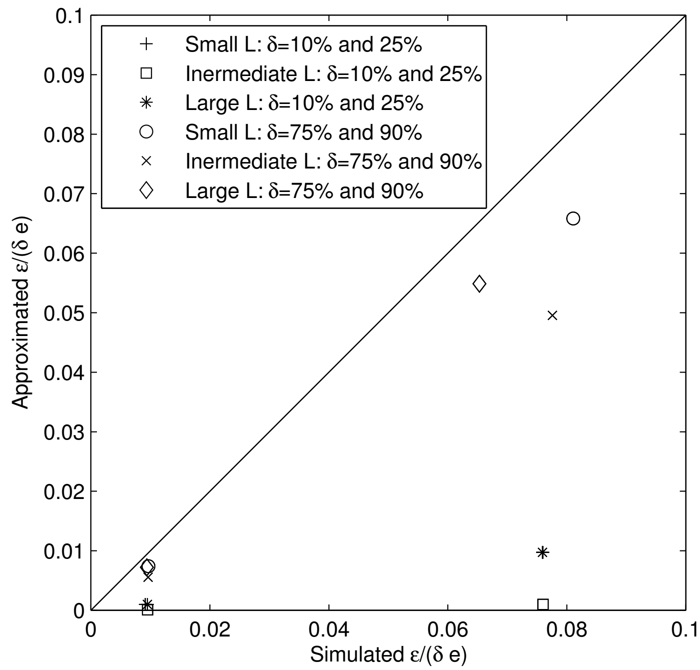

Figure 5.3: Numerically simulated $\xi/\delta e$ versus the approximated $\xi/\delta e$ by equation 5.10 at various δ and L values. A flat liquid-gas interface was assumed in the calculations.

expressed as:

$$\frac{1}{\xi/\delta e} = \frac{1}{\delta \xi_g} + \frac{1}{\xi_{ideal}} \tag{5.10}$$

The numerically calculated effective slip length at different local slip lengths (ξ_g=0.01, 0.1, 1, and 10) was compared with equation 5.10 (figure 5.3). The results showed that for longitudinal grooves, the above equation was valid only for large air fractions (75% and 90%) and the roughness period to channel height ratio L was not a critical parameter, because it had minimal effects on the effective slip length. Though this formula has not been justified physically, it provided reasonable estimation of the effective slip length involving a shear boundary condition at flat liquid-gas interfaces for pressure-driven flow. It is worth noticing that equation 5.10 was not a good predictor for rough surfaces with small air fractions (e.g., 0.1 and 0.25), which was not reported in Ybert et al. [53].

5.3.3 Influence of coupled liquid-gas interfacial shear and curvature

In this section, the coupled effect of interfacial shear and curvature of the liquid-gas interface is considered at different roughness period to channel height ratio (L=0.2, 1, and 5) and gas fractions (δ=0.1, 0.25, 0.5, 0.75 and 0.9). Teo and Khoo (2010) studied the effect of interfacial curvature on the effective slip length for different normalized channel lengths and gas fractions. I plotted similar curves of the normalized effective slip length against interface protrusion angles corresponding to various local slip lengths at liquid-gas interfaces ξ_g (figure 5.4).

The trend of the effective slip length ($\xi/\delta e$) varied as the interface protrusion angle (θ) was different for different values of L and ξ_g. For small L values, $\xi/\delta e$ increased as θ increases at the large local slip length (ξ_g=10), while opposite trend was observed at small values of ξ_g. Particularly, there was a peak in the curve $\xi/\delta e \quad \theta$ in between $\theta = -2/\pi$ and $\theta = -2/\pi$. The results agreed with the numerical calculations for superhydrophobic surfaces with a lattice of holes [64], which indicated that largest drag or friction reduction can be achieved by manipulating the contact angle of the fluid. For intermediate and large L values, increasing the protrusion angle θ lead to a decreased $\xi/\delta e$. The magnitude of the variation of the effective slip length decreased as the local slip length decreases. Different behaviors between various L values were due to the increasing confinement effect from the bottom wall when increasing the value of L [120]. It should be noted that negative effective slip length was obtained, which can explain the overestimation of the effective slip length by model predictions. The negative effective slip length was attributed to blockage effect arising from the meniscus protruding into the liquid phase, as well as the limited slip at liquid-gas interfaces.

Furthermore, I compared the numerical results with the analytical estimation by equation 5.10. A linear relationship between $\xi/\delta e$ and $1/(1/\delta\xi_g + 1/\xi_{ideal})$ was observed at large gas fractions (75% and 90%), indicating that the effective slip length increased as the gas fraction increased monotonously, and with a larger interface protrusion angle, the effective slip length increased more rapidly (figure 5.5). Similar linear relationship was shown for the curves of $1/(1/\delta\xi_g + 1/\xi_{ideal})$ for intermediate and large L (figure 5.6

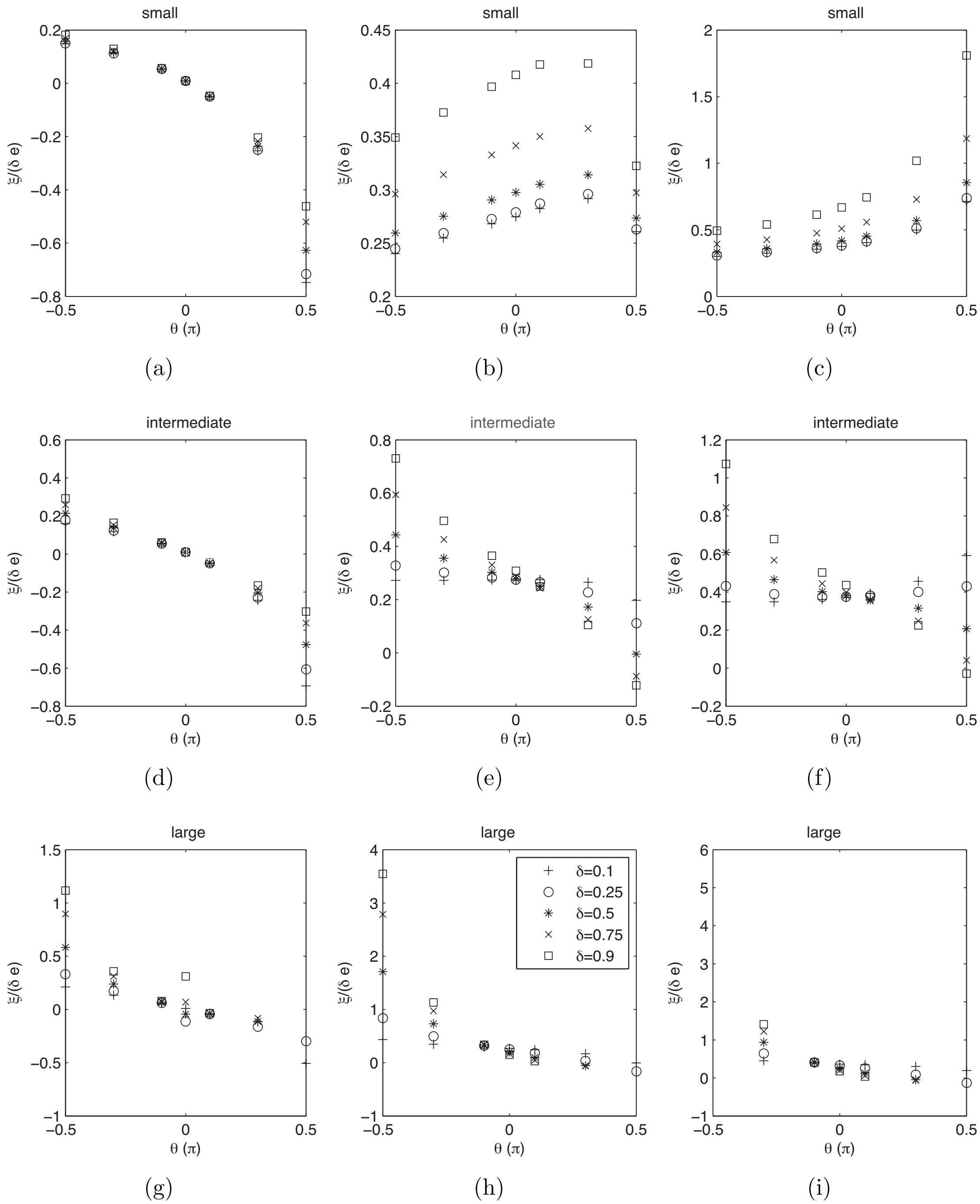

Figure 5.4: Numerically simulated $\xi/\delta e$ at different values of θ for small, intermediate, and large L at various values of δ. The calculation was conducted with $\xi = 0.01$ (a, d, g), $\xi = 1$ (b, e, h) and $\xi = 10$ (c, f, i).

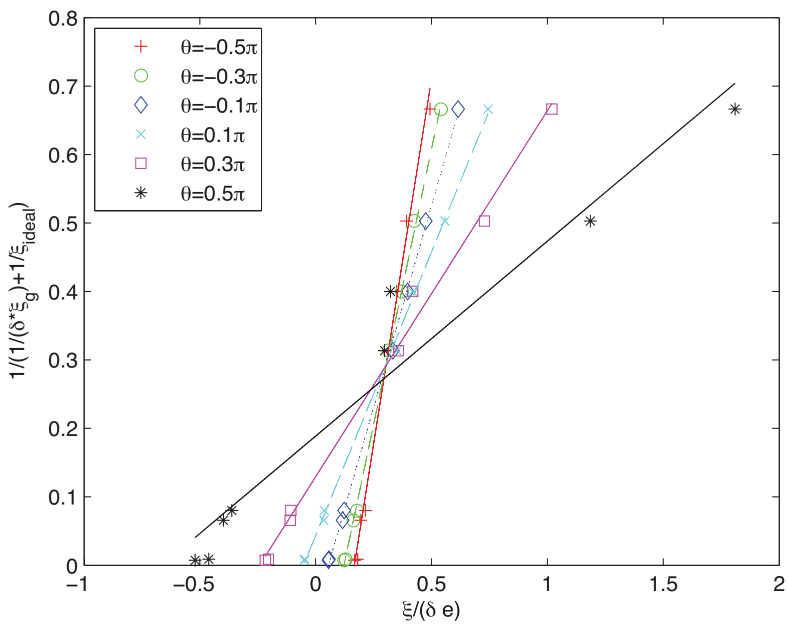

(a) small L

Figure 5.5: Numerically simulated $\xi/\delta e$ versus the approximation by equation 5.10. The calculations were conducted at small L. The figures include results at $\delta = 75\%$ and $\delta = 90\%$.

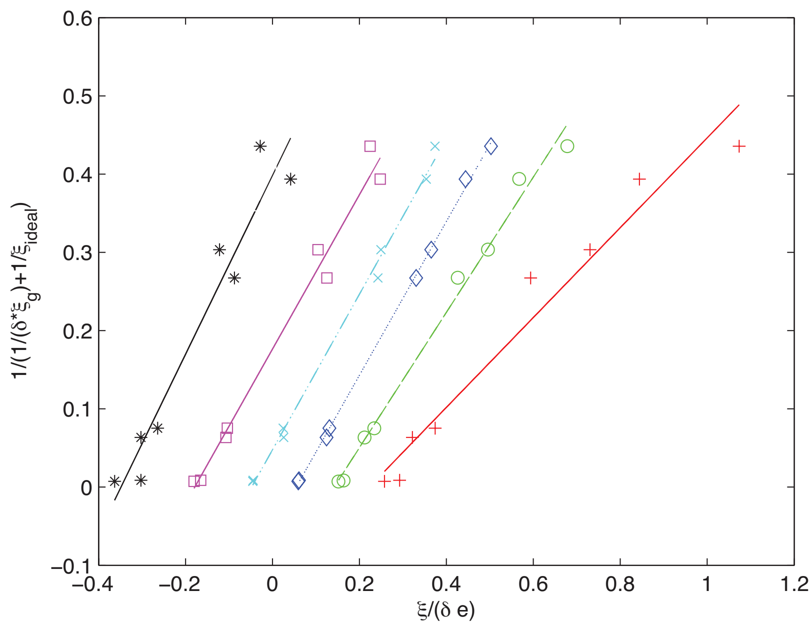

(a) intermediate L

Figure 5.6: Numerically simulated $\xi/\delta e$ versus the approximation by equation 5.10. The calculations were conducted at intermediate L. The figures include results at $\delta = 75\%$ and $\delta = 90\%$.

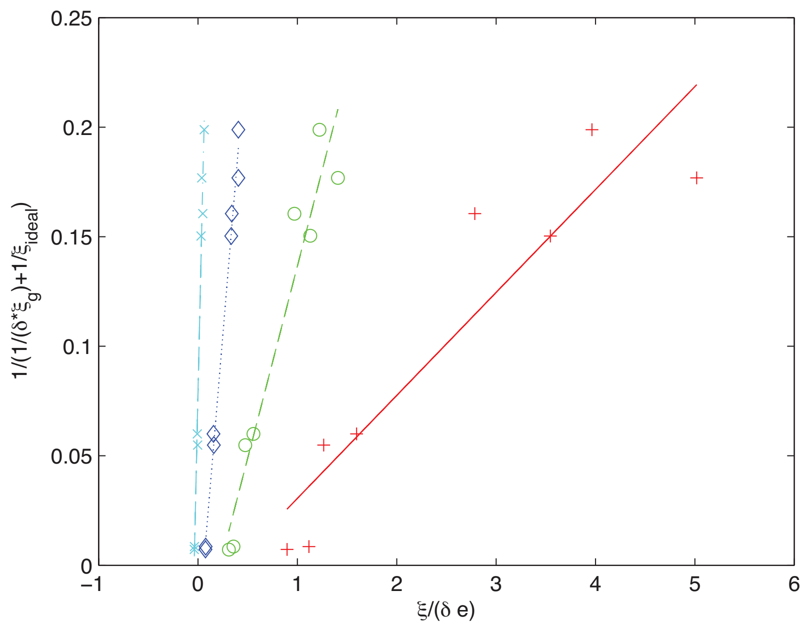

(a) large L

Figure 5.7: Numerically simulated $\xi/\delta e$ versus the approximation by equation 5.10. The calculations were conducted at large L. The figures include results at $\delta = 75\%$ and $\delta = 90\%$.

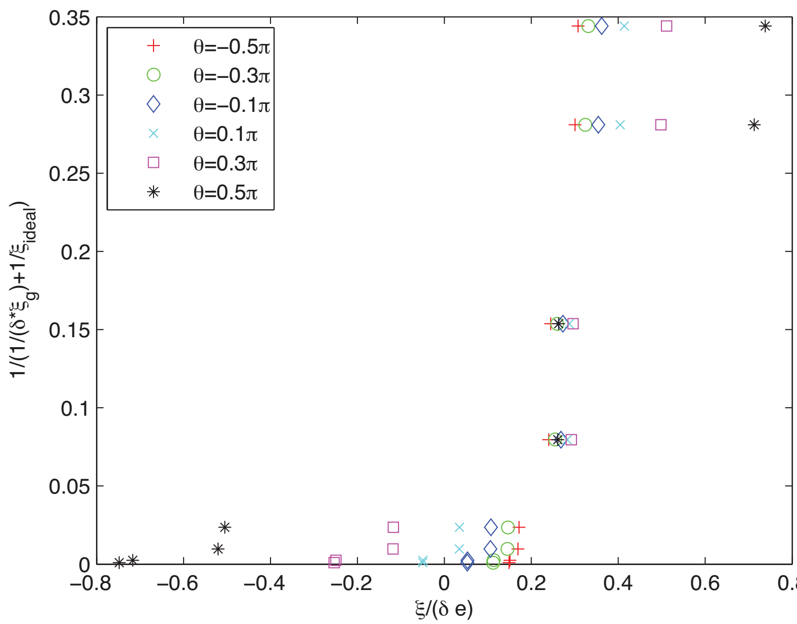

Figure 5.8: Numerically simulated $\xi/\delta e$ versus the approximation by equation 5.10. The calculations were conducted at for small L. The figure presents the result at $\delta = 10\%$.

and (figure 5.7)). At small gas fractions, the relationship between $\xi/\delta e$ and $1/(1/\delta\xi_g + 1/\xi_{ideal})$ was more complicated (figure 5.8).

5.4 Summary

In this study, pressure-driven laminar flow in microchannels patterned with ribs and grooves parallel to the flow direction was solved numerically for different roughness period to channel height ratio (L), gas fractions (δ), interface protrusion angles (θ) and normalized local slip lengths at liquid-gas interfaces (ξ_g). The dependence of the effective slip length on the channel roughness scales, interfacial curvature and local slip length at air-water interfaces was investigated, and compared with the analytical solutions. The preliminary results clearly show that the coupled interfacial effects (curved interface and local slip length) influence the effective slip length in an extremely complicated way. Additional work may include analytical consideration using the method of scaling laws analysis ([53]). Future work also includes experimental studies, such as in Tsai et al. ([63]), to explore the microflow behavior at a broader range of system variables.

Chapter 6

CONCLUSIONS

6.1 Summary

The research presented in this dissertation aimed to improve the understanding of multiphase flow in porous media, with the goal of providing pore-scale experimental observations and numerical simulations that can guide the development of macroscale multiphase flow models. In the pore-scale investigations, flow pattern in open microchannels was fully recorded using the $\mu-$PIV technique. In addition, numerical simulations of flow in microchannels revealed the key parameters of interfacial shape and shear and provide the basis for exploring the relationship between those key parameters and a broad range of system variables. Models for the macroscopic hydraulic conductivity were developed on a basis of pore-scale flows, which took into account the results from pore-scale studies. Specifically, the primary conclusions are:

1. Partial-slip, rather than the commonly used stress-free condition, provided a more accurate description of the boundary condition at confined air-water interfaces. Experimental measurements of the velocity profiles in open capillary channels showed that the maximum velocity along the profile was located between the air-water interface and the bottom of the channel, not at the air-water interface.

2. The observed interfacial shear stress at confined air-water interfaces can be attributed to the velocity gradient from adjoining no-slip walls to the channel center where flow is trapped in capillary-force-dominated region. Application of the Stokes equation with mixed boundary conditions (i.e., no-slip on the channel walls and partial-slip or shear stress at the air-water interface) clearly illustrated

the increasing importance of interfacial shear stress with decreasing channel size. The dominant effect of capillary forces in confined flow regions leads to the observed interfacial curvature and shear stress, which in turn lead to non-stress-free air-water interface.

3. Based on the knowledge gained from the pore-scale experimental study of the boundary condition at air-water interface, and combined with numerical simulations for corner flow, analytical expressions for unsaturated hydraulic conductivity were derived. Prediction of unsaturated hydraulic conductivity was improved by replacing a shear-free boundary condition with a partial-slip boundary condition at air-water interfaces for corner flow.

4. We developed a roughness-TPSM (RTPSM) for water retention and unsaturated hydraulic conductivity based on the framework of the TPSM [41]. The model explicitly considered the surface geometrical features on the solid walls that significantly increased the water film length at low water content. The developed model significantly improved the prediction of unsaturated hydraulic conductivity over the entire range from wet to dry conditions for heavier-textured soils . Additionally, effort was also made to relate the roughness factor to other soil physical properties, e.g., soil particle composition and organic matter content, which are normally available in soil database.

5. The coupled effect of interfacial shape and interfacial shear can lead to greatly negative effective slip length, which provided an explanation for the overestimated slip length at mixed liquid-gas and liquid-solid surfaces calculated assuming shear-free at the liquid-solid surfaces.

Collectively, improved physical understanding of surface/interface effects on flow behavior at the microscale was achieved. The experimental evidence of the scale-dependent slip boundary condition at air-water interface should draw attention from scientists or engineers in various research fields, including vadose zone hydrology, oil recovery, remediation of environmentally contaminated sites, design and manipulation of flow in microfluidics and so on. We have demonstrated that modeling of macroscopic hydraulic conductivity can be improved by taking into account surface/interface interactions which dominant at the pore scale. The same idea on the modeling work can be further extended to more realistic models such as the pore network model.

6.2 Future Work

Better understanding of the pore-scale flow behavior provide us with the capability of mechanistically explaining the macroscale flow phenomena. Extension of this research to further explore the insight into the physics of multiphase flow in porous media and relevant fields may include:

1. To conduct $\mu-$PIV experiments for flow over rough/patterned surfaces to validate the numerical simulations presented in Chapter 5.

2. To develop hydraulic conductivity models based on the framework of pore network models taking into account scale-dependent partial-slip air-water interface and surface roughness. The pore network models involve the interactions between pores, which are more realistic than capillary-based-models. However, the hydrodynamic consideration is still in its infancy in terms of the interfacial shear effects on hydrodynamics in a single pore unit.

3. To investigate the effect of partial-slip air-water interface on colloid transport and retention in unsaturated porous media. Favorable sites for colloid retention under unsaturated flow conditions include the air-phase-related factors, such as air-water interfaces, thin film, and contact lines. Capillary forces have been proposed as the main mechanism for colloid retention at those interfaces, but have not been well quantified. The partial-slip air-water interface, which allows largely decreased movement of water (the carrier of colloids), may provide addition insight of the problem.

4. To investigate surface roughness effect on colloid transport and retention in unsaturated porous media. Roughness is commonly regarded as one of the primary factors causing the discrepancies between predictions from the classical filtration theory (CFT) and experimental observations. While most studies aim to understand the roughness effect on chemical forces between a colloid and collectors, the complex fluid behavior near a rough surface (boundary layer) is generally ignored.

BIBLIOGRAPHY

[1] H-J Vogel and K Roth. Quantitative morphology and network representation of soil pore structure. *Advances in water resources*, 24(3):233–242, 2001.

[2] Soil Science Society of America. *Glossary of soil science terms*. Soil Science Society of America, 1970.

[3] Klaus Mosthaf, Rainer Helmig, and Dani Or. Modeling and analysis of evaporation processes from porous media on the rev scale. *Water Resources Research*, 50(2):1059–1079, 2014.

[4] E. C. Childs and N. Collisgeorge. The permeability of porous materials. *Proceedings of the Royal Society of London Series a-Mathematical and Physical Sciences*, 201(1066):392–405, 1950.

[5] E. Bresler, D. Russo, and R. D. Miller. Rapid estimate of unsaturated hydraulic conductivity function. *Soil Science Society of America Journal*, 42(1):170–172, 1978.

[6] R.H. Brooks and A.T. Corey. *Hydraulic Properties of Porous Media*. Colorado State University, 1964.

[7] S. Assouline. On the relationships between the pore size distribution index and characteristics of the soil hydraulic functions. *Water Resources Research*, 41(7), 2005.

[8] J. C. Muccino, W. G. Gray, and L. A. Ferrand. Toward an improved understanding of multiphase flow in porous media. *Reviews of Geophysics*, 36(3):401–422, 1998.

[9] Y. H. Liu, D. D. Nolte, and L. J. Pyrak-Nolte. Hysteresis and interfacial energies in smooth-walled microfluidic channels. *Water Resources Research*, 47, 2011.

[10] M. L. Porter, D. Wildenschild, G. Grant, and J. I. Gerhard. Measurement and prediction of the relationship between capillary pressure, saturation, and interfacial area in a napl-water-glass bead system. *Water Resources Research*, 46, 2010.

[11] W. G. Gray and S. M. Hassanizadeh. Paradoxes and realities in unsaturated flow theory. *Water Resources Research*, 27(8):1847–1854, 1991.

[12] S. M. Hassanizadeh and W. G. Gray. Toward an improved description of the physics of 2-phase flow. *Advances in Water Resources*, 16(1):53–67, 1993.

[13] T. C. G. Kibbey and L. Chen. Measurement of air-water interfacial area for multiple hysteretic drainage curves in an unsaturated fine sand. *Langmuir*, 22(16):6874–6880, 2006.

[14] D. Q. Chen, L. J. Pyrak-Nolte, J. Griffin, and N. J. Giordano. Measurement of interfacial area per volume for drainage and imbibition. *Water Resources Research*, 43(12), 2007.

[15] S. Whitaker. Advances in theory of fluid motion in porous media. *Industrial and Engineering Chemistry*, 61(12):14–, 1969.

[16] T. B. Anderson and R. Jackson. A fluid mechanical description of fluidized beds. *Industrial and Engineering Chemistry Fundamentals*, 6(4):527–, 1967.

[17] W. G. Gray and S. M. Hassanizadeh. Averaging theorems and averaged equations for transport of interface properties in multiphase systems. *International Journal of Multiphase Flow*, 15(1):81–95, 1989.

[18] W. G. Gray and S. M. Hassanizadeh. Macroscale continuum mechanics for multiphase porous-media flow including phases, interfaces, common lines and common points. *Advances in Water Resources*, 21(4):261–281, 1998.

[19] J. Atencia and D. J. Beebe. Controlled microfluidic interfaces. *Nature*, 437(7059):648–655, 2005.

[20] M. Gad-el Hak. The fluid mechanics of microdevices - the freeman scholar lecture. *Journal of Fluids Engineering-Transactions of the Asme*, 121(1):5–33, 1999.

[21] V. Lazouskaya, Y. Jin, and D. Or. Interfacial interactions and colloid retention under steady flows in a capillary channel. *Journal of Colloid and Interface Science*, 303(1):171–184, 2006.

[22] O. Manor, I. U. Vakarelski, G. W. Stevens, F. Grieser, R. R. Dagastine, and D. Y. C. Chan. Dynamic forces between bubbles and surfaces and hydrodynamic boundary conditions. *Langmuir*, 24(20):11533–11543, 2008.

[23] O. Manor, I. U. Vakarelski, X. S. Tang, S. J. O'Shea, G. W. Stevens, F. Grieser, R. R. Dagastine, and D. Y. C. Chan. Hydrodynamic boundary conditions and dynamic forces between bubbles and surfaces. *Physical Review Letters*, 101(2):–, 2008.

[24] D. Yang, M. Krasowska, C. Priest, M. N. Popescu, and J. Ralston. Dynamics of capillary-driven flow in open microchannels. *Journal of Physical Chemistry C*, 115(38):18761–18769, 2011.

[25] R. Byron Bird, Warren E. Stewart, and Edwin N. Lightfoot. *Transport phenomena*. J. Wiley, 2002.

[26] R. Pit, H. Hervet, and L. Leger. Direct experimental evidence of slip in hexadecane: Solid interfaces. *Physical Review Letters*, 85(5):980–983, 2000.

[27] Richards.S. No-slip boundary-condition. *Journal of Fluid Mechanics*, 59(Aug7):707–719, 1973.

[28] L. M. Hocking. Moving fluid interface on a rough surface. *Journal of Fluid Mechanics*, 76(Aug25):801–817, 1976.

[29] B. Y. Du, E. Goubaidoulline, and D. Johannsmann. Effects of laterally heterogeneous slip on the resonance properties of quartz crystals immersed in liquids. *Langmuir*, 20(24):10617–10624, 2004.

[30] N. V. Churaev, V. D. Sobolev, and A. N. Somov. Slippage of liquids over lyophobic solid-surfaces. *Journal of Colloid and Interface Science*, 97(2):574–581, 1984.

[31] O. I. Vinogradova. Slippage of water over hydrophobic surfaces. *International Journal of Mineral Processing*, 56(1-4):31–60, 1999.

[32] V. S. J. Craig and C. Neto. In situ calibration of colloid probe cantilevers in force microscopy: Hydrodynamic drag on a sphere approaching a wall. *Langmuir*, 17(19):6018–6022, 2001.

[33] E. Bonaccurso, M. Kappl, and H. J. Butt. Hydrodynamic force measurements: Boundary slip of water on hydrophilic surfaces and electrokinetic effects. *Physical Review Letters*, 88(7), 2002.

[34] Y. X. Zhu and S. Granick. Limits of the hydrodynamic no-slip boundary condition. *Physical Review Letters*, 88(10), 2002.

[35] E. Bonaccurso, H. J. Butt, and V. S. J. Craig. Surface roughness and hydrodynamic boundary slip of a newtonian fluid in a completely wetting system. *Physical Review Letters*, 90(14), 2003.

[36] E. Lauga. Apparent slip due to the motion of suspended particles in flow of electrolyte solutions. *Langmuir*, 20(20):8924–8930, 2004.

[37] L. Bocquet and J. L. Barrat. Flow boundary conditions from nano- to micro-scales. *Soft Matter*, 3(6):685–693, 2007.

[38] C. Neto, D. R. Evans, E. Bonaccurso, H. J. Butt, and V. S. J. Craig. Boundary slip in newtonian liquids: a review of experimental studies. *Reports on Progress in Physics*, 68(12):2859–2897, 2005.

[39] Thomas Lee, Eric Charrault, and Chiara Neto. Interfacial slip on rough, patterned and soft surfaces: A review of experiments and simulations. *Advances in Colloid and Interface Science*, 2014.

[40] Y. Mualem. New model for predicting hydraulic conductivity of unsaturated porous-media. *Water Resources Research*, 12(3):513–522, 1976.

[41] M. Tuller and D. Or. Hydraulic conductivity of variably saturated porous media: Film and corner flow in angular pore space. *Water Resources Research*, 37(5):1257–1276, 2001.

[42] M. T. van Genuchten. A closed-form equation for predicting the hydraulic conductivity of unsaturated soils. *Soil Science Society of America Journal*, 44(5):892–898, 1980.

[43] Shmuel Assouline and Dani Or. Conceptual and parametric representation of soil hydraulic properties: A review. *Vadose Zone Journal*, 12(4), 2013.

[44] N. T. Burdine. Relative permeability calculations from pore size distribution data. *Transactions of the American Institute of Mining and Metallurgical Engineers*, 198:71–78, 1953.

[45] J. R. Nimmo. Treatment of residual water-content in a consistent set of parametric models for the 2-phase flow of immiscible fluids in the subsurface - comment. *Water Resources Research*, 27(4):661–662, 1991.

[46] M. J. Blunt. Flow in porous media - pore-network models and multiphase flow. *Current Opinion in Colloid & Interface Science*, 6(3):197–207, 2001.

[47] V. Joekar-Niasar and S. M. Hassanizadeh. Analysis of fundamentals of two-phase flow in porous media using dynamic pore-network models: A review. *Critical Reviews in Environmental Science and Technology*, 42(18):1895–1976, 2012.

[48] M. J. Blunt, M. D. Jackson, M. Piri, and P. H. Valvatne. Detailed physics, predictive capabilities and macroscopic consequences for pore-network models of multiphase flow. *Advances in Water Resources*, 25(8-12):1069–1089, 2002.

[49] J. R. Philip. Flow in porous media. *Annual Review of Fluid Mechanics*, 2:177–204, 1970.

[50] J. R. Philip. Flows satisfying mixed no-slip and no-shear conditions. *Zeitschrift Fur Angewandte Mathematik Und Physik*, 23(3):353–372, 1972.

[51] E. Lauga and H. A. Stone. Effective slip in pressure-driven stokes flow. *Journal of Fluid Mechanics*, 489:55–77, 2003.

[52] C. Cottin-Bizonne, C. Barentin, E. Charlaix, L. Bocquet, and J. L. Barrat. Dynamics of simple liquids at heterogeneous surfaces: Molecular-dynamics simulations and hydrodynamic description. *European Physical Journal E*, 15(4):427–438, 2004.

[53] C. Ybert, C. Barentin, C. Cottin-Bizonne, P. Joseph, and L. Bocquet. Achieving large slip with superhydrophobic surfaces: Scaling laws for generic geometries. *Physics of Fluids*, 19(12), 2007.

[54] Ayyaswam.Ps, I. Catton, and D. K. Edwards. Capillary flow in triangular grooves. *Journal of Applied Mechanics-Transactions of the Asme*, 41(2):332–336, 1974.

[55] L. A. Romero and F. G. Yost. Flow in an open channel capillary. *Journal of Fluid Mechanics*, 322:109–129, 1996.

[56] L. Parkinson, R. Sedev, D. Fornasiero, and J. Ralston. The terminal rise velocity of 10-100 mu m diameter bubbles in water. *Journal of Colloid and Interface Science*, 322(1):168–172, 2008.

[57] G. M. Wang, R. Prabhakar, and E. M. Sevick. Hydrodynamic mobility of an optically trapped colloidal particle near fluid-fluid interfaces. *Physical Review Letters*, 103(24), 2009.

[58] D. Y. C. Chan, R. Manica, L. Parkinson, and J. Ralston. Interpreting the dynamic interaction between a very small rising bubble and a hydrophilic titania surface. *Journal of Physical Chemistry C*, 114(4):1942–1946, 2010.

[59] T. C. Ransohoff and C. J. Radke. Laminar-flow of a wetting liquid along the corners of a predominantly gas-occupied noncircular pore. *Journal of Colloid and Interface Science*, 121(2):392–401, 1988.

[60] S. K. Su and C. L. Lai. Interfacial shear-stress effects on transient capillary wedge flow. *Physics of Fluids*, 16(6):2033–2043, 2004.

[61] S. W. Tchikanda, R. H. Nilson, and S. K. Griffiths. Modeling of pressure and shear-driven flows in open rectangular microchannels. *International Journal of Heat and Mass Transfer*, 47(3):527–538, 2004.

[62] S. K. Thomas, R. C. Lykins, and K. L. Yerkes. Fully developed laminar flow in trapezoidal grooves with shear stress at the liquid-vapor interface. *International Journal of Heat and Mass Transfer*, 44(18):3397–3412, 2001.

[63] P. C. Tsai, A. M. Peters, C. Pirat, M. Wessling, R. G. H. Lammertink, and D. Lohse. Quantifying effective slip length over micropatterned hydrophobic surfaces. *Physics of Fluids*, 21(11):–, 2009.

[64] A. Steinberger, C. Cottin-Bizonne, P. Kleimann, and E. Charlaix. High friction on a bubble mattress. *Nature Materials*, 6(9):665–668, 2007.

[65] C. Cottin-Bizonne, B. Cross, A. Steinberger, and E. Charlaix. Boundary slip on smooth hydrophobic surfaces: Intrinsic effects and possible artifacts. *Physical Review Letters*, 94(5):–, 2005.

[66] O. I. Vinogradova, K. Koynov, A. Best, and F. Feuillebois. Direct measurements of hydrophobic slippage using double-focus fluorescence cross-correlation. *Physical Review Letters*, 102(11):–, 2009.

[67] J. G. Santiago, S. T. Wereley, C. D. Meinhart, D. J. Beebe, and R. J. Adrian. A particle image velocimetry system for microfluidics. *Experiments in Fluids*, 25(4):316–319, 1998.

[68] John Happel and Brenner Howard. *Low reynolds number hydrodynamics*. Prentice-Hall, 1965.

[69] J. S. Park, C. K. Choi, and K. D. Kihm. Optically sliced micro-piv using confocal laser scanning microscopy (clsm). *Experiments in Fluids*, 37(1):105–119, 2004.

[70] R. Lindken, M. Rossi, S. Grosse, and J. Westerweel. Micro-particle image velocimetry (mu piv): Recent developments, applications, and guidelines. *Lab on a Chip*, 9(17):2551–2567, 2009.

[71] J. M. Wan and T. K. Tokunaga. Comments on "pore-scale visualization of colloid transport and retention in partly saturated porous media". *Vadose Zone Journal*, 4(4):954–956, 2005.

[72] Vassili V. Yaminsky, Satomi Ohnishi, Erwin A. Vogler, and Roger G. Horn. Stability of aqueous films between bubbles. part 1. the effect of speed on bubble coalescence in purified water and simple electrolyte solutions. *Langmuir*, 26(11):8061–8074, 2010.

[73] L. X. Cheng, G. Ribatski, and J. R. Thome. Two-phase flow patterns and flow-pattern maps: Fundamentals and applications. *Applied Mechanics Reviews*, 61(5):–, 2008.

[74] Ven-Te Chow. *Open-Channel Hydraulics*. Mcgraw-Hill College, 1959.

[75] Joseph B. Franzini, E. John Finnemore, and Robert L. Daugherty. *Fluid mechanics with engineering applications*. McGraw-Hill, 1997.

[76] S.T. Yuster. Theoretical considerations of multiphase flow in idealized capilalry systems. *Proc. 3rd World Petroleum Congr.*, 2, 1951.

[77] E. E. Miller and R. D. Miller. Physical theory for capillary flow phenomena. *Journal of Applied Physics*, 27(4):324–332, 1956. Miller, ee miller, rd.

[78] W. R. Gardner. Some steady-state solutions of the unsaturated moisture flow equation with application to evaporation from a water table. *Soil science*, 85((4)):228–232, 1958.

[79] Wenjuan Zheng, Lian-Ping Wang, Dani Or, Volha Lazouskaya, and Yan Jin. Role of mixed boundaries on flow in open capillary channels with curved air-water interfaces. *Langmuir*, 2012. doi: 10.1021/la302833p.

[80] Feike J. Leij and Laboratory National Risk Management Research. *The UNSODA unsaturated soil hydraulic database: user's manual*. UNSODA, the UNSODA unsaturated soil hydraulic database. National Risk Management Research Laboratory, Office of Research and Development, U.S. Environmental Protection Agency, Cincinnati, Ohio, 1996.

[81] N. Hansen, S. D. Muller, and P. Koumoutsakos. Reducing the time complexity of the derandomized evolution strategy with covariance matrix adaptation (cma-es). *Evolutionary Computation*, 11(1):1–18, 2003.

[82] Franois Kalaydjian. Origin and quantification of coupling between relative permeabilities for two-phase flows in porous media. *Transport in porous media*, 5(3):215–229, 1990.

[83] S. Berg, A. W. Cense, J. P. Hofman, and R. M. M. Smits. Two-phase flow in porous media with slip boundary condition. *Transport in Porous Media*, 74(3):275–292, 2008. Berg, S. Cense, A. W. Hofman, J. P. Smits, R. M. M.

[84] Marc Lebeau and Jean-Marie Konrad. A new capillary and thin film flow model for predicting the hydraulic conductivity of unsaturated porous media. *Water Resources Research*, 46, 2010.

[85] TC Ransohoff, PA Gauglitz, and CJ Radke. Snapoff of gas bubbles in smoothly constricted noncircular capillaries. *AIChE Journal*, 33(5):753–765, 1987.

[86] S. A. Koehler, S. Hilgenfeldt, and H. A. Stone. Foam drainage on the microscale - i. modeling flow through single plateau borders. *Journal of Colloid and Interface Science*, 276(2):420–438, 2004.

[87] M. J. Fayer and C. S. Simmons. Modified soil-water retention functions for all matric suctions. *Water Resources Research*, 31(5):1233–1238, 1995.

[88] Z. Fred Zhang. Soil water retention and relative permeability for conditions from oven-dry to full saturation. *Vadose Zone Journal*, 10(4):1299–1308, 2011.

[89] A. Peters and W. Durner. A simple model for describing hydraulic conductivity in unsaturated porous media accounting for film and capillary flow. *Water Resources Research*, 44(11), 2008.

[90] A. Peters. Simple consistent models for water retention and hydraulic conductivity in the complete moisture range. *Water Resources Research*, 49(10):6765–6780, 2013.

[91] Dani Or and Markus Tuller. Flow in unsaturated fractured porous media: Hydraulic conductivity of rough surfaces. *Water Resources Research*, 36(5):1165–1177, 2000.

[92] B. Ataie-Ashtiani, S.M. Hassanizadeh, M. Oostrom, M.A. Celia, and M.D. White. Effective parameters for two-phase flow in a porous medium with periodic heterogeneities. *Journal of Contaminant Hydrology*, 49(1-2):87 – 109, 2001.

[93] M. Mirzaei and D. B. Das. Dynamic effects in capillary pressuresaturations relationships for two-phase flow in 3d porous media: Implications of micro-heterogeneities. *Chemical Engineering Science*, 62(7):1927 – 1947, 2007.

[94] C.A. Aggelopoulos and C.D. Tsakiroglou. The effect of micro-heterogeneity and capillary number on capillary pressure and relative permeability curves of soils. *Geoderma*, 148(1):25 – 34, 2008.

[95] Delwyn G Fredlund and Anqing Xing. Equations for the soil-water characteristic curve. *Canadian Geotechnical Journal*, 31(4):521–532, 1994.

[96] C. Y. Shen, B. G. Li, C. Wang, Y. F. Huang, and Y. Jin. Surface roughness effect on deposition of nano- and micro-sized colloids in saturated columns at different solution ionic strengths. *Vadose Zone Journal*, 10(3):1071–1081, 2011.

[97] P. M. Adler and H. Brenner. Multiphase flow in porous-media. *Annual Review of Fluid Mechanics*, 20:35–59, 1988.

[98] J. H. M. Wosten, Y. A. Pachepsky, and W. J. Rawls. Pedotransfer functions: bridging the gap between available basic soil data and missing soil hydraulic characteristics. *Journal of Hydrology*, 251(3-4):123–150.

[99] W. J. Rawls and D. L. Brakensiek. Estimating soil-water retention from soil properties. *Journal of the Irrigation and Drainage Division-Asce*, 108(2):166–171, 1982.

[100] H. Vereecken, M. Weynants, M. Javaux, Y. Pachepsky, M. G. Schaap, and M. Th van Genuchten. Using pedotransfer functions to estimate the van genuchten-mualem soil hydraulic properties: A review. *Vadose Zone Journal*, 9(4):795–820, 2010.

[101] S. Y. Cheng, R. Bryant, S. H. Doerr, C. J. Wright, and P. R. Williams. Investigation of surface properties of soil particles and model materials with contrasting hydrophobicity using atomic force microscopy. *Environmental Science & Technology*, 43(17):6500–6506.

[102] A. G. Hunt, B. Ghanbarian, and K. C. Saville. Unsaturated hydraulic conductivity modeling for porous media with two fractal regimes. *Geoderma*, 207:268–278, 2013.

[103] NK Nagpal, L Boersma, and LW DeBacker. Pore size distributions of soils from mercury intrusion porosimeter data. *Soil Science Society of America Journal*, 36(2):264–267, 1972.

[104] Sang Il Hwang and Sang Il Choi. Use of a lognormal distribution model for estimating soil water retention curves from particle-size distribution data. *Journal of Hydrology*, 323(1-4):325–334, 2006.

[105] Eric Lauga, Michael Brenner, and Howard Stone. Microfluidics: the no-slip boundary condition. *Springer handbook of experimental fluid mechanics*, pages 1219–1240, 2007.

[106] J. P. Rothstein. Slip on superhydrophobic surfaces. *Annual Review of Fluid Mechanics*, 42:89–109, 2010.

[107] Roman S. Voronov, Dimitrios V. Papavassiliou, and Lloyd L. Lee. Review of fluid slip over superhydrophobic surfaces and its dependence on the contact angle. *Industrial & Engineering Chemistry Research*, 47(8):2455–2477, 2008.

[108] W. Barthlott and C. Neinhuis. Purity of the sacred lotus, or escape from contamination in biological surfaces. *Planta*, 202(1):1–8, 1997.

[109] Bharat Bhushan and Yong Chae Jung. Micro-and nanoscale characterization of hydrophobic and hydrophilic leaf surfaces. *Nanotechnology*, 17(11):2758, 2006.

[110] S. Lee, J. Cho, and M. Elimelech. Influence of colloidal fouling and feed water recovery on salt rejection of ro and nf membranes. *Desalination*, 160(1):1–12, 2004.

[111] C. H. Choi, U. Ulmanella, J. Kim, C. M. Ho, and C. J. Kim. Effective slip and friction reduction in nanograted superhydrophobic microchannels. *Physics of Fluids*, 18(8), 2006. Choi, Chang-Hwan Ulmanella, Umberto Kim, Joonwon Ho, Chih-Ming Kim, Chang-Jin.

[112] J. ou, B. Perot, and J. P. Rothstein. Laminar drag reduction in microchannels using ultrahydrophobic surfaces. *Physics of Fluids*, 16(12):4635–4643, 2004.

[113] C. I. Bouzigues, L. Bocquet, E. Charlaix, C. Cottin-Bizonne, B. Cross, L. Joly, A. Steinberger, C. Ybert, and P. Tabeling. Using surface force apparatus, diffusion and velocimetry to measure slip lengths. *Philosophical Transactions of the Royal Society a-Mathematical Physical and Engineering Sciences*, 366(1869):1455–1468, 2008.

[114] J. Davies, D. Maynes, B. W. Webb, and B. Woolford. Laminar flow in a microchannel with superhydrophobic walls exhibiting transverse ribs. *Physics of Fluids*, 18(8), 2006. Davies, J. Maynes, D. Webb, B. W. Woolford, B.

[115] Jens Harting, Christian Kunert, and Jari Hyvaluoma. Lattice boltzmann simulations in microfluidics: probing the no-slip boundary condition in hydrophobic, rough, and surface nanobubble laden microchannels. *Microfluidics and Nanofluidics*, 8(1):1–10, 2010. Times Cited: 12 Harting, Jens/B-4884-2008; , /C-3671-2012 Harting, Jens/0000-0002-9200-6623; 0 12.

[116] J. Ou and J. P. Rothstein. Direct velocity measurements of the flow past drag-reducing ultrahydrophobic surfaces. *Physics of Fluids*, 17(10):–, 2005.

[117] D. Maynes, B. W. Webb, and J. Davies. Thermal transport in a microchannel exhibiting ultrahydrophobic microribs maintained at constant temperature. *Journal of Heat Transfer-Transactions of the Asme*, 130(2), 2008. Maynes, D. Webb, B. W. Davies, J.

[118] C. O. Ng and C. Y. Wang. Apparent slip arising from stokes shear flow over a bidimensional patterned surface. *Microfluidics and Nanofluidics*, 8(3):361–371, 2010. Ng, Chiu-On Wang, C. Y.

[119] M. Sbragaglia and A. Prosperetti. A note on the effective slip properties for microchannel flows with ultrahydrophobic surfaces. *Physics of Fluids*, 19(4):–, 2007.

[120] C. J. Teo and B. C. Khoo. Flow past superhydrophobic surfaces containing longitudinal grooves: effects of interface curvature. *Microfluidics and Nanofluidics*, 9(2-3):499–511, 2010. Teo, C. J. Khoo, B. C.

Appendix A

DERIVATION OF THE MENISCUS SHAPE EQUATION

A.1 Derivation of the Equation Governing the Static Meniscus Shape

We consider the static problem (no flow) shown in figure 2.1. Imagine that the surface height (measured from the channel bottom) is h_0 if there is no surface curvature (i.e., $\theta = 90°$). The pressure at the bottom of the channel is then $p_{bottom,0} = p_{atm} + \rho g h_0$. This is defined as our reference state. Now the surface is wetting and the contact angle is $\theta < 90°$. Since there is no flow, the pressure at the bottom of the channel must be the same (independent of x) as otherwise there will be local horizontal flow in the x direction near the bottom. Let us call this bottom pressure $P_{bottom,1}$. An overall force balance in the vertical direction for the whole water column would yield

$$p_{bottom,1} w + 2\sigma \cos\theta = p_{atm} w + \rho g h_0 w \tag{A.1}$$

The pressure variation inside air is neglected due to the low density relative to the water. Therefore,

$$p_{bottom,1} = p_{atm} + \rho g h_0 - \frac{2\sigma \cos\theta}{w} = p_{bottom,0} - \frac{2\sigma \cos\theta}{w} \tag{A.2}$$

Namely, the bottom water pressure is reduced by an amount that depends on the surface tension, contact angle, and channel width, if the column is bounded by wetting solid walls. Note that, for given contact angle and surface tension, the correction of bottom pressure by the capillary effect is inversely proportional to the channel size w. To determine the local meniscus shape, we can take a differential water column from x to $x + dx$ extending from the channel bottom to the air-water interface. For simplicity, we draw a control volume with top surface just inside the air-water interface, so the pressure there is

$$p_{insideAWI} = p_{atm} - \frac{\sigma}{R}, \text{ with } \frac{1}{R} = \frac{\frac{d^2h}{dx^2}}{[1+(\frac{dh}{dx})^2]^{3/2}} \tag{A.3}$$

Then the force balance in the vertical direction for the differential water column gives

$$p_{bottom,1}dx = p_{insideAWI}dx + \rho g h dx \tag{A.4}$$

The force balance in the horizontal direction can be expressed as

$$\{p_{bottom,1}h(x) - \rho g\frac{[h(x)]^2}{2}\} - \{p_{bottom,1}h(x+dx) - \rho g\frac{[h(x+dx)]^2}{2}\} + p_{insideAWI}dh = 0 \tag{A.5}$$

which yields the same equation as equation A.4. This is expected as all surface forces act in the direction normal to the local surface. Combining equations A.3 and A.4 leads to a single governing equation for $h(x)$ as:

$$\rho g(h-h_0) = \frac{\rho\frac{d^2h}{dx^2}}{[1+(\frac{dh}{dx})^2]^{3/2}} - \frac{2\rho\cos\theta}{w} \tag{A.6}$$

The left hand side of equation A.6 represents hydrostatic pressure relative to the reference flat surface. The right hand side is the difference of local capillary pressure and the reference capillary pressure based on a reference curvature radius $R_0 = \frac{w}{2\cos\theta}$. This reference radius is a radius of a circle drawn passing through the wall contact line points with the same given contact angle, with the center of the circle located at the center of the channel. We have assumed that the two bounding vertical solid walls have a same contact angle, as in our microchannels. The formulation above can be extended to walls having different wetting properties.

A.2 Derivation of the Meniscus Shape Equation in the Limit of Very Small Channel Width

We first define the Bond number (Bo) in our experimental system as the ratio of gravity effect and capillary effect as:

$$Bo = \frac{\rho g R}{\frac{2\sigma\cos\theta}{w}} \approx \frac{\rho g \frac{w}{2\cos\theta}}{\frac{2\sigma\cos\theta}{w}} = \frac{\rho g w^2}{4\sigma\cos^2\theta} \tag{A.7}$$

If the Bond number is very small, then the left hand side of equation A.6 can be neglected, and we have

$$0 \approx \frac{\sigma\frac{d^2}{dx^2}}{[1+(\frac{dh}{dx})^2]^{3/2}} - \frac{\sigma}{R_0} \tag{A.8}$$

Let $\phi \equiv \frac{dh}{dx}$, the equation can be re-written as

$$\frac{\phi\frac{d\phi}{dh}}{[1+\phi^2]^{3/2}} = \frac{1}{R_0} \tag{A.9}$$

Integrate analytically to give:

$$\frac{1}{[1+\phi^2]^{1/2}} = -\frac{[h-h(x=0.5w)]}{R_0} + 1 \tag{A.10}$$

We have applied the condition that $\varphi|_{x=0.5w} = 0$. This can be written as

$$\frac{\phi\frac{d\phi}{dx}}{\sqrt{R_0^2-\phi^2}} = 1 \text{ for } x < 0.5w; \text{ where } \phi \equiv R_0 - [h - h|_{x=0.5w}] \tag{A.11}$$

Again this can be integrated analytically, to obtain

$$h = h|_{x=0.5w} + R - \sqrt{R_0^2 - (x-0.5w)^2} \tag{A.12}$$

which is a circular arc as expected (since equation A.8 implies that the local curvature radius at any x location is equal to R_0). This limiting solution also shows that the circular arc must be exact for small w cases. Equation A.12 can also be written using h_0 as:

$$h = h_0 - \sqrt{(\frac{w}{2\cos\theta})^2 - (x - \frac{w}{2})^2} + \frac{w}{2\cos\theta}[\frac{\sin^{-1}(\cos\theta)}{2\cos\theta} + \frac{1}{2}\sin\theta] \tag{A.13}$$

Appendix B

DESCRIPTION OF TPSM BY TULLER AND OR (2001)

B.1 Unit Cell Geometry

The single pore space of a porous medium is represented by a unit cell, which is composed of a triangular central pore and slit-shaped space connecting central pores (figure 3.1). The unit cell is characterized by the central pore length L and two dimensionless parameters: slit-spacing scaling factor α and slit-length scaling factor β. The applied single pore space allows for dual occupancy of wetting and non-wetting phase.

B.2 Wetting Phase Saturation Curve of a Single Cell

Over a wide range of matric potential, the drainage process of the unit cell includes different stages. At relatively low matric potentials, the pore remains fully saturated with the wetting phase. The non-wetting phase begins to enter the central pore but leaving the slits-shaped space filled at a matric potential of μ_1. When decreasing the matric potential gradually to a certain value of μ_2, the wetting phase retains in corners and in form of adsorbed film on all the exposed solid surfaces. Tuller et al. (2000) applied a shifted augmented Young-Laplace equation to combine adsorptive and capillary components under a certain matric potential. The adsorbed film thickness (h) is estimated as a function of matric potential (μ) assuming that the film is exclusively controlled by van der Waals forces

$$h(\mu) = \sqrt[3]{\frac{A_{svl}}{6\pi\rho\mu}} \tag{B.1}$$

The radius of the interfacial curvature (r) is shifted from the film thickness h, and is obtained from the classic Young-Laplace equation:

$$r(\mu) = \frac{\sigma}{\rho\mu} \tag{B.2}$$

where A_{svl} is the Hamaker constant for solid-vapor interactions through the intervening liquid (i.e., water), A_{svl} = -6.010^{-20} J (Russel et al., 2006); ρ is the density of water; σ is the surface tension of water; $\sigma = 0.0728$ N m^{-1}. The configuration of the interface between wetting and no-wetting phases is thus determined with the adsorbed film thickness h and radius of interfacial curvature r (Fig. 1). The degree of saturation is defined as the area of occupied by the wetting phase divided by the total area of the unit cell. With a known configuration of the wetting phase, the saturation ratio is readily expressed as:

$$s_w = \begin{array}{cc} 1 & (\mu > \mu_2) \\ \frac{2\alpha\beta+3h(\mu)[L-h(\mu)]+r(\mu)^2(3\sqrt{3}-\pi)}{(2\alpha\beta+\sqrt{3}/4)L^2} & (\mu_1 < \mu < \mu_2) \\ \frac{Lh(\mu)(3+4\beta-2\alpha)-3h(\mu)^2+r(\mu)^2(3\sqrt{3}-\pi)}{(2\alpha\beta+\sqrt{3}/4)L^2} & (\mu < \mu_1) \end{array} \tag{B.3}$$

B.3 Conductance of Wetting Phase in a Single Cell

We first consider the hydrodynamics of flow within a single cell. For pores with complete saturation of wetting phase, flows occur in ducts (central pore) and between parallel plates (slits); for partial saturation, flows occurs in form of adsorbed films on all the exposed solid surfaces, and in corners of the central pore. As the flow in the cell is assumed to be at slow laminar condition and the interface between wetting and non-wetting phase remains stable, the Navier-Stokes equation was applied to solve the average flow rate for each flow regime (Tuller et. al., 2000). The average flow rate (v) was converted to hydraulic conductance (K) using $v = \frac{Q}{A} = \frac{K}{\rho g}(-\frac{dp}{dz})$, where $-\frac{dp}{dz}$ is the pressure head gradient, which is cancelled out in the expressions for hydraulic conductance for each element:

$$\text{Slits: } K_s = \frac{\rho g}{\eta}\frac{\alpha^2 L^2}{12} \tag{B.4}$$

$$\text{Triangular duct: } K_d = \frac{\rho g}{\eta}\frac{\alpha^2 L^2}{80} \tag{B.5}$$

$$\text{Film: } K_f = \begin{cases} \frac{\rho g}{\eta}\frac{h(\mu)^2}{3} & h \geq 10nm \\ \frac{\rho g}{\eta}\frac{B(\mu)}{12h(\mu)} & h \leq 10nm \end{cases} \tag{B.6}$$

$$\text{Corner: } K_c = \frac{\rho g}{\eta}\frac{r(\mu)^2}{\varepsilon} \tag{B.7}$$

where η_0 is the viscosity of water, $\eta_0 = 1.00210^{-3}$ kg m^{-1} s^{-1}; ε is a dimensionless flow resistance parameter. When the hydrodynamic boundary condition of the interface is treated as shear-free (perfect slip), the value of ε is set as 31.07 for corners with a corner angle of 60° and contact angle of 0° between the wetting phase and solid surface. As the interface may not always follow the shear-free boundary condition due to the confined pore space, we proposed that the flow resistance parameter can be expressed a function of saturation degree as $\varepsilon = 31.07 f(S)$.

Hydraulic conductance of the unit cell for the wetting phase is calculated by adding up the weighted conductance of each element over its occupied cross-sectional area and divided by the total cross-sectional area of the single cell:

$$K_w(\mu) = \begin{cases} \frac{2\alpha\beta L^2 K_s + \sqrt{3}/4L^2 K_d}{2\alpha\beta + \sqrt{3}/4L^2} & (\mu > \mu_2) \\ \frac{2\alpha\beta L^2 K_s + 3h(\mu)[L - 2\sqrt{3}r(\mu)]K_f + r(\mu)^2(3\sqrt{3}-\pi)K_c}{(2\alpha\beta+\sqrt{3}/4)L^2} & (\mu_1 < \mu < \mu_2) \\ \frac{h(\mu)(3L + 4\beta L - 6\sqrt{3}r(\mu) - 3h(\mu))K_f + r(\mu)^2(3\sqrt{3}-\pi)K_c}{(2\alpha\beta+\sqrt{3}/4)L^2} & (\mu < \mu_1) \end{cases} \tag{B.8}$$

The relative hydraulic conductivity $K_{wr}(\mu)$ is thus obtained by dividing $K_w(\mu)$ by K_{sat}.

$$K_{wr}(\mu) = K_w(\mu)/K_{wsat} \tag{B.9}$$

B.4 Upscaling from Pore Scale to Sample Scale

Upscaling from a single unit cell to a population of pores is usually achieved by assigning a statistical probability distribution of pore sizes to produce the saturation or hydraulic conductivity at the sample scale. Porous media with narrow pore size distributions (e.g., sandy soils) can be represented by a uniform pore size distribution. Therefore, using the TPSM with a uniform pore size, the sample scale saturation curve and hydraulic conductivity are the same with those at the pore scale.

Appendix C

REVERSE FLOW

C.1 Movie.avi

This movie shows colloid tracers in the contact line region moving in the direction opposite to bulk ow. This video recorded the ow in a 0.6 mm channel with a mean velocity of 0.514 mm s^{-1}.